
1

2 μ/π separation using

3 Convolutional Neural Networks

4 for the MicroBooNE

5 Charged Current Inclusive Cross Section

6 Measurement

7

8 Jessica Nicole Esquivel

9 Bachelor of Science in Electrical Engineering and Applied Physics

10 St. Mary's University

11 San Antonio, TX, USA 2011

12 DISSERTATION

13 Submitted in partial fulfillment

14 of the requirements for the degree

15 *Doctor of Philosophy in Physics*

16 - * - DRAFT December 30, 2017 - * -

17 December, 2017

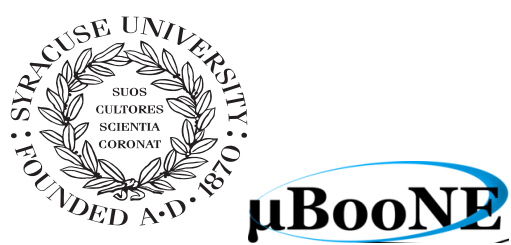
18 Syracuse University

19 Syracuse, New York

20
21
22
23

Copyright 2017
Jessica Nicole Esquivel
All Rights Reserved
Syracuse University

24



μ BooNE



26

Abstract

27

The purpose of this thesis was to use Convolutional Neural Networks
28 (CNN) to separate μ' s and π' s for use in increasing the acceptance rate
29 of μ' 's below the implemented 75cm track length cut in the Charged
30 Current Inclusive (CC-Inclusive) event selection for the CC-Inclusive
31 Cross-Section Measurement. In doing this, we increase acceptance
32 rate for CC-Inclusive events below a specific momentum range.

33

Dedication

34

I dedicate this dissertation to the two important women in my life; My
35 wife and my mom. Both have been there cheering me on giving me strength
36 and love as I worked towards the hardest accomplishment I've ever done.

37

Jessica Nicole Esquivel

38

Acknowledgements

39 Of the many people who deserve thanks, some are particularly prominent, such as
40 my supervisor...

Contents

41	List of figures	xv
43	List of tables	xxiii
44	1 Introduction	1
45	2 Neutrinos	3
46	2.1 What are Neutrinos	3
47	2.2 History of Neutrinos	4
48	2.3 Neutrino Oscillations	4
49	2.3.1 Solar Oscillations and the Solar Neutrino Problem	5
50	2.3.2 Atmospheric Oscillations and the Atmospheric Neutrino Anomaly	7
51	2.3.3 Two Flavor Neutrino Oscillation Formulation	9
52	2.3.4 Three Flavor Neutrino Oscillation Formulation	12
53	2.3.5 Reactor Oscillation	13
54	3 The MicroBooNE Experiment	15
55	3.1 Liquid argon time projection chambers	15
56	3.2 The MicroBooNE Time Projection Chamber	16
57	3.3 MicroBooNE’s Physics Goals	18
58	3.3.1 The low-energy excess	18
59	3.3.2 Cross sections	19
60	3.3.3 Liquid argon detector development	20
61	3.4 The Booster Neutrino Beam	20
62	3.4.1 Creating the Booster Neutrino Beam	21
63	3.5 Event Reconstruction	22

64	4 Neutrino Identification: Finding MicroBooNE's first Neutrinos	25
65	4.1 Flash Finding	25
66	4.1.1 Flash Reconstruction	26
67	4.1.2 Beam Timing	27
68	4.1.3 Event Rates	28
69	4.2 TPC Topology Selection	28
70	4.2.1 Cosmic Tagging	29
71	4.2.2 2D Cluster Selection	29
72	4.2.3 3D Tracks and vertices Selection	31
73	4.2.4 TPC Updates	33
74	4.3 Conclusion	34
75	5 CC-Inclusive Cross Section Selection Filter	35
76	5.1 Data and MC Processing Chain	36
77	5.2 Normalization of data and MC	37
78	5.3 Optical Software Trigger and Reconstruction	39
79	5.3.1 Software Trigger	39
80	5.3.2 Flash Reconstruction	40
81	5.3.3 Beam Window	40
82	5.4 TPC Reconstruction	42
83	5.4.1 Hit Reconstruction	43
84	5.4.2 Clustering	43
85	5.4.3 Pandora	43
86	5.4.4 Trackkalmanhit	43
87	5.4.5 Cosmic Hit Removal	43
88	5.4.6 Projection Matching Algorithm	43
89	5.4.7 Calorimetry	43
90	5.5 Event Selection	43
91	6 Background on Convolutional Neural Networks	45
92	6.1 Image Classification	45
93	6.2 CNN Structure	46
94	6.2.1 Backpropagation	49
95	6.3 Choosing Hyperparameters	50

96	7 Training Convolutional Neural Networks on particles WORKING TITLE	53
97	7.1 Hardware Frameworks used for Training	54
98	7.1.1 Syracuse CPU Machine setup	54
99	7.1.2 Syracuse University GPU Cluster Setup	54
100	7.2 Convolutional Neural Network Training	54
101	7.2.1 Image Making Scheme	54
102	7.2.2 Training CNN1075	55
103	7.2.3 Training CNN10000	55
104	7.2.4 Training CNN100000	57
105	8 Results of Convolutional Neural Networks on particles WORKING TITLE	71
106	8.1 Classification using CNN10000	71
107	8.1.1 Classification of MC data using Selection I Original CC-Inclusive Filter	71
108	8.1.2 Classification of MC data using Selection I Modified CC-Inclusive Filter	75
109	8.1.3 Conclusions and Future Work	83
110	8.2 Classification using CNN100000	85
111	8.2.1 Classification of MC data using Selection I Modified CC-Inclusive Filter	85
112	8.2.2 Classification of MicroBooNE data using Selection I Modified CC-Inclusive Filter	85
113	8.2.3 Comparing two CC-Inclusive Cross Section Selection Filters	85
114	9 Conclusion	87
115	Bibliography	89

¹²⁰ List of figures

¹²¹	2.1	The Standard Solar Model	5
¹²²	2.2	Solar Neutrino Experiments	7
¹²³	2.2a	Ray Davis's Homestake Experiment	7
¹²⁴	2.2b	Kamiokande Experiment	7
¹²⁵	2.2c	SNO Experiment	7
¹²⁶	2.3	Cosmic Ray Shower	8
¹²⁷	2.4	Measurements of the double ratio for various atmospheric neutrino experiments	9
¹²⁹	2.5	The flavor eigenstates are rotated by an angle θ with respect to the mass eigenstates	10
¹³¹	3.1	Low Energy excess seen in MiniBooNE	19
¹³²	3.2	Arial view of the Main Injector and the Booster Neutrino Beam at Fermilab	21
¹³³	3.3	Arial view of the Main Injector and the Booster Neutrino Beam at Fermilab	23
¹³⁴	3.4	Energy spectrum of the Booster Neutrino Beam at Fermi National Laboratories	24
¹³⁶	4.1	Efficiency for selecting beam events as a function of minimum total PE cut for all PE cuts as well as zoomed into interesting region.	26
¹³⁸	4.2a	Predicted distribution of flash times with respect to trigger time for 1 day of data taking at nominal rate and intensity	31

140	4.2b	Measured distribution of flash times with a 50 PE threshold cut, with respect to trigger time. Shown as a ratio to the expected cosmic rate from off-beam data. A clear excess from neutrinos is visible between 3- 5 μ s after the trigger time.	31
144	4.3	Percent of good clusters remaining for neutrinos and cosmics after the primary cuts were applied. This is relative to total number of initial clusters.	32
147	4.4	Percent matched cluster pairs remaining for neutrinos and cosmics after secondary cuts applied. This is relative to the number of events that contain clusters which pass the primary cuts.	32
150	5.1	5.1a Track range distribution for selection I. The track range is defined as the 3D distance between the start and end of the muon candidate track. No data is shown below 75 cm due to the track length cut described previously. 5.1b Efficiency of the selected events by process quasi-elastic (QE), resonant (RES), and deep-inelastic (DIS). Statistical uncertainty is shown in the bands and the distributions are a function of true muon momentum. The rise of the efficiency between 0 GeV and 0.5 GeV is due to the minimum track length cut and the decreasing efficiency for higher momentum tracks is caused by the containment requirement. .	38
159	5.1a	Track range distribution of selection I	38
160	5.1b	Selection efficiency as a function of the true muon momentum .	38
161	5.2	Time distribution of reconstructed optical flashes with a PE value of 50 or more for a sample of BNB unbiased triggered events.	41
163	5.3	Flash time distribution for all flashes (left plot) and flashes > 20PE (right plot). The different curves are as follows: on-beam data (black), off-beam data (red), CORSIKA inTime MC (light blue), BNB only MC (green), and BNB+Cosmic MC (purple). The dashed vertical lines mark the time window that was chosen for each sample	41
168	5.4	Reconstruction chain run on both data and MC. The red stars mean that the algorithm returns reconstructed 3D vertices.	42

170	6.1 Pixel representation and visualization of a curve detector filter. As you 171 can see, in the pixel representation, the weights of this filter are greater 172 along a curve we are trying to find in the input image	47
173	6.2 Visualization of filters found in first layer of a CNN.	47
174	6.3 Applying a feature mask over a set of fashion items to extract necessary 175 information for auto-encoding. Unnecessary information for example 176 color or brand emblems are not saved. This feature map is an edge detec- 177 tion mask that leaves only shape information which helps to distinguish 178 between different types of clothes.	48
179	6.4 Pictorial Representation of Convolutional Neural Networks as well as a 180 visual representation on CNN's complexity of layer feature extraction	48
181	6.5 Pictoral representation of the AlexNet model. The AlexNet model 182 consists of 5 convolution layers and 3 fully connected layers.	51
183	6.6 Pictoral representation of the GoogleNet model. The GoogleNet model 184 consists of 22 layers. The model implements 9 Inception modules which 185 performs covolution and pooling in parallel and strays away from 186 the basis that CNN layers need to be stacked up sequentially. The 187 GoogleNet model also doesn't use fully connected layers, instead it 188 uses average pooling which greatly reduces the amount of parameters. 189 GoogleNet has 12x fewer parameters than AlexNet.	51
190	7.1 Accuracy vs. Loss of ImageNet 2-output μ/π sample consisting of 191 10000 images each.	57
192	7.2 Description of confusion matrix variables: False pion rate = $false\pi/total\pi$ 193 True pion rate = $true\pi/total\pi$ Accuracy = $(true\pi rate + true\mu rate)/2$ 194 Pion prediction value = $true\pi/(true\pi + false\pi)$ Muon prediction value 195 = $true\mu/(true\mu + false\mu)$ 7.2c The probability plot includes muons and 196 pions that are classified as primary particles.	58
197	7.2a Confusion Matrix showing Accuracy of CNN using training data	58
198	7.2b Confusion Matrix showing Accuracy of CNN using testing data	58

199	7.2c	Probability plot of muons and pions from testing set. Images surrounding histogram are a random event from lowest bin and highest bin for each particle.	58
200			
201			
202	7.3	Confusion Matrix of all five particles	59
203	7.4	Training and testing accuracy of CNN trained on 100,000 images of $\mu/\pi/p/\gamma/e$ with 20,000 images of each particle. Each image was a size of 576x576 and the images per particle were split 90% use for training and 10% used for testing the network	60
204			
205			
206			
207	7.5	Training and testing loss of CNN trained on 100,000 images of $\mu/\pi/p/\gamma/e$	60
208	7.6	t-SNE of CNN	61
209	7.7	Muon Prob	62
210	7.8	Pion Prob	62
211	7.9	Proton Prob	63
212	7.10	Electron Prob	63
213	7.11	Gamma Prob	64
214	7.12	Prob	64
215	7.13	mupi	65
216	7.14	mupi	65
217	7.15	mupi	66
218	7.16	mup	66
219	7.17	mup	67
220	7.18	mup	67
221	7.19	mue	68
222	7.20	mue	68
223	7.21	mue	69
224	7.22	mug	69

225	7.23 mug	70
226	7.24 mug	70
227	8.1 Snapshot of passing rates of Selection I from CC-Inclusive Filter	72
228	8.2 Results of CNN10000 classification of track candidate images output from cc-inclusive filter.	73
230	8.2a Confusion Matrix showing Accuracy of CNN using data with wrong normilazion	73
232	8.2b Probability plot showing μ/π separation of CNN using wrong normalization	73
234	8.2c Confusion Matrix showing Accuracy of CNN using data with correct normilazion	73
236	8.2d Probability plot showing μ/π separation of CNN using correct normalization	73
238	8.3 CNN10000 distributions of track candidate images output from Selec- tion I Original cc-inclusive filter with different image data normalizations	74
240	8.3a Track range distribution of events from Selection I Original passing CNN with 70% accuracy using image data with wrong normilazion	74
243	8.3b Track range distribution of events from Selection I Original pass- ing CNN with 70% accuracy using image data with correct normilazion	74
246	8.3c Momentum distribution of events from Selection I Original pass- ing CNN with 70% accuracy using image data with wrong normilazion	74
249	8.3d Momentum distribution of events from Selection I Original pass- ing CNN with 70% accuracy using image data with correct normilazion	74
252	8.4 Snapshot of passing rates of all cuts from Selection I Modified cc- inclusive filter	75

254	8.5 Confusion matrix and probability plot of events passing selection I modified cc-inclusive cuts right before 75cm track length cut	76
255		
256	8.5a Confusion Matrix for CNN10000 classified events from selection I modified	76
257		
258	8.5b Probability plot for CNN10000 classified events from selection I modified	76
259		
260	8.6 CNN10000 distributions of track candidate images output from Selection I Modified cc-inclusive filter	77
261		
262	8.6a Track range distribution of events from Selection I Modified passing CNN with 70% accuracy	77
263		
264	8.6b Stacked signal and background track range distributions from Selection I Modified passing CNN with 70% accuracy	77
265		
266	8.6c Stacked signal and background track range distributions from Selection I Modified passing 75 cm track length cut	77
267		
268	8.6d Stacked signal muons and background muons/pions of track range distributions from Selection I Modified passing CNN with 70% accuracy	77
269		
270	8.6e Stacked signal muons and background muons/pions of track range distributions from Selection I Modified passing 75 cm track length cut	77
271		
272		
273		
274	8.7 CNN10000 stacked signal/background track range distributions of track candidate images output from Selection I Modified cc-inclusive filter	78
275		
276	8.7a Stacked signal muons and background muons/pions of track range distributions from Selection I Modified passing CNN with 75% accuracy	78
277		
278	8.7b Stacked signal muons and background muons/pions of track range distributions from Selection I Modified passing CNN with 80% accuracy	78
279		
280		
281		

282	8.7c	Stacked signal muons and background muons/pions of track range distributions from Selection I Modified passing CNN with 85% accuracy	78
285	8.7d	Stacked signal muons and background muons/pions of track range distributions from Selection I Modified passing CNN with 90% accuracy	78
288	8.8	CNN10000 momentum distributions of track candidate images output from Selection I Modified cc-inclusive filter	79
290	8.8a	Momentum distribution of events from Selection I Modified passing CNN with 70% accuracy	79
292	8.8b	Stacked signal and background momentum distributions from Selection I Modified passing CNN with 70% accuracy	79
294	8.8c	Stacked signal and background momentum distributions from Selection I Modified passing 75 cm track length cut	79
296	8.9	Track distribution comparisons of true CC muons plotted vs true CC muons and pions plotted	81
298	8.9a	Stacked signal μ /background μ and π track range distribution of CNN @ 70%	81
300	8.9b	Stacked signal $\mu\&\pi$ /background $\mu\&\pi$ track range distribution of CNN @ 70%	81
302	8.10	Images of true CC events where the pion was the tagged track candidate	81
303	8.10a	Pion reconstructed track range is less than 75 cm and longer than muon track due to dead wires	81
305	8.10b	Pion reconstructed track range is less than 75 cm and larger than muon reconstructed track	81
307	8.10c	Pion reconstructed track range is greater than 75 cm and larger than muon reconstructed track	81
309	8.11	Snapshot of signal and background event numbers of Selection I modified from cc-inclusive note [?]	84

311	8.12 CNN performance of classified muons and pions compared to the al-	
312	ready implemented 75 cm track length cut	84

³¹³ List of tables

³¹⁴ 4.1	Passing rates for 2D cluster cuts for neutrino on MC set and a cosmic only MC set. First column shows event rates with no cuts applied to both sets. Columns two and three show event rates after primary and secondary cuts are applied. Line three shows the second line scaled with the flash finding factor of 0.008. All events are normalized to per day assuming we are running at 5 Hz.	31
³²⁰ 8.1	Comparing passing rates of CNN at different probabilities versus 75 cm track length cut: Numbers are absolute event counts and Cosmic background is not scaled appropriately. The BNB+Cosmic sample contains all events. The numbers in brackets give the passing rate wrt the step before (first percentage) and wrt the generated events (second percentage). In the BNB+Cosmic MC Truth column shows how many true ν_μ CC-inclusive events (in FV) are left in the sample. This number includes possible mis-identifications where a cosmic track is picked by the selection instead of the neutrino interaction in the same event. The CNN MC True generated events were scaled wrt the MC True generated events for the 75 cm cut passing rates due to only running over 188,880 generated events versus the 191362 generated events. The last column Signal:Cosmic only gives an estimate of the ν_μ CC events wrt the cosmic only background at each step. For this number, the cosmic background has been scaled as described in [?]. Note that these numbers are not a purity, since other backgrounds can't be determined at this step. . .	82

336	8.2 Signal and background event numbers at modified selection level with	
337	CNN cut estimated from a BNB+Cosmic sample and Cosmic only sam-	
338	ple normalized to $5 * 10^{19}$ PoT. The last column gives the fraction of	
339	this signal or background type to the total selected events per CNN	
340	probability.	82

*"If they don't give you a seat at the table,
bring a folding chair."*

— Shirley Chisholm

³⁴³ **Chapter 1**

³⁴⁴ **Introduction**

³⁴⁵ This thesis will be a description of work done to further increase efficiency and purity
³⁴⁶ of the charged current inclusive cross section measurement using the MicroBooNE
³⁴⁷ detector. It will also describe the MicroBooNE detector, what neutrinos are, the
³⁴⁸ charged current inclusive cross section measurement and its importance as well as
³⁴⁹ convolutional neural networks and how they can be used in μ/π separation. Chapter
³⁵⁰ **2** will talk about the background of neutrinos and the people and detectors that
³⁵¹ discovered neutrinos as well as an in depth history of neutrino oscillation and the
³⁵² discovery that neutrinos have mass.

³⁵³ Chapter **3** will discuss the MicroBooNE experiment, specifically, how Liquid
³⁵⁴ Argon Time Projection Chambers work, the Light Collection System and the Electronic
³⁵⁵ and Readout Trigger systems. This chapter will also describe the Booster Neutrino
³⁵⁶ Beam sationed at Fermilab.

³⁵⁷ Chapter **4** will discuss the work that was done to detect the first neutrinos seen in
³⁵⁸ the MicroBooNE detector and the software reconstruction efforts required to create an
³⁵⁹ automated neutrino ID filter that was used to find the first neutrinos and then was
³⁶⁰ later expanded on to create the charged current inclusive filter that will be discussed
³⁶¹ in chapter **5**

³⁶² Chapter **6** will give a brief description of what Convolutional Neural Networks are
³⁶³ and how it will be used for μ/π separation in this selection. Chapter **7** will discuss
³⁶⁴ the hardware frameworks and training methods used to train multiple Convolutional
³⁶⁵ Neural Networks for use in the charged current inclusive cross section measurement.
³⁶⁶ Chapters **8** and **??** will discuss the results of using Convolutional Neural Networks on
³⁶⁷ monte-carlo and data to sift out charged current inclusive neutrino events.

³⁶⁸ **Chapter 2**

³⁶⁹ **Neutrinos**

³⁷⁰ **2.1 What are Neutrinos**

³⁷¹ Neutrinos are one of the fundamental particles which make up the universe. They are
³⁷² also one of the least understood. Neutrinos are not affected by the electromagnetic
³⁷³ forces because they do not have electric charge. Neutrinos are affected by a "weak"
³⁷⁴ sub-atomic force of much shorter range than electromagnetism, and are therefore able
³⁷⁵ to pass through great distances in matter without being affected by it. Until the late
³⁷⁶ 90's, neutrinos were thought to have no mass. Due to their mass, neutrinos are also
³⁷⁷ affected by gravity. Neutrinos are created by radioactive decay or nuclear reactions
³⁷⁸ such as the ones that happen in the sun, in nuclear reactors or when cosmic rays hit
³⁷⁹ atoms. There are three types of neutrinos, ν_e , ν_μ and ν_τ which correspond to their
³⁸⁰ charged lepton pairs.

³⁸¹ As previously stated, neutrinos are very weakly interacting; in fact, neutrinos can
³⁸² pass unscathed through a wall of lead several hundred light-years thick. Because
³⁸³ neutrinos interact so rarely, studying neutrinos requires a massive detector and a
³⁸⁴ powerful neutrino source. With that being said, we can only infer their existence when
³⁸⁵ they interact in a detector. In a collision, distinct charged particles are produced with
³⁸⁶ each type of neutrino. An electron neutrino will create an electron, a muon neutrino
³⁸⁷ will create a muon, and a tau neutrino will create a tau. The track the particle leaves
³⁸⁸ in the detector is how one figures out what type of neutrino interaction was "seen".
³⁸⁹ Liquid Argon Time Projection Chambers are the newest type of detectors being used to
³⁹⁰ study neutrinos due to their excellent imaging and particle identification capabilities.

³⁹¹ 2.2 History of Neutrinos

³⁹² The neutrino was first postulated by Wolfgang Pauli in 1931 to explain how beta
³⁹³ decay could resolve the conservation of energy, momentum and angular momentum
³⁹⁴ problem. Pauli suggested that this missing energy might be carried off, unseen, by a
³⁹⁵ neutral particle (he called neutron) which was escaping detection. James Chadwick
³⁹⁶ discovered a much heavier nuclear particle in 1932 that he also named neutron, leaving
³⁹⁷ two particles with the same name. Enrico Fermi was the first person to coin the
³⁹⁸ term neutrino (which means little neutral one in latin) in 1933 to fix this confusion.
³⁹⁹ Fermi's paper, which was published in 1934, unified Pauli's neutrino with Paul Dirac's
⁴⁰⁰ positron and Werner Heisenberg's neutron-proton model and his theory accurately
⁴⁰¹ explained many experimentally observed results. Wang Ganchang first proposed the
⁴⁰² use of beta capture to experimentally detect neutrinos and in 1959 Clyde Cowan and
⁴⁰³ Frederick Reines published their work stating that they had detected the neutrino.
⁴⁰⁴ The experiment called for antineutrinos created in a nuclear reactor by beta decay that
⁴⁰⁵ reacted with protons producing neutrons and positrons: $\nu_e + p^+ \rightarrow n^0 + e^+$. Once
⁴⁰⁶ this happens, the positron finds an electron and they annihilate each other and the
⁴⁰⁷ resulting gamma rays are detectable. The neutron is detected by neutron capture and
⁴⁰⁸ the releasing of another gamma ray. In 1962 Leon M. Lenderman, Melvin Schwartz
⁴⁰⁹ and Jack Steinberger were the first to detect interactions of the muon neutrino. The
⁴¹⁰ first detection of the tau neutrino was announced in the summer of 2000 by the
⁴¹¹ DONUT collaboration at Fermilab. In the late 1960s, many experiments found that the
⁴¹² number of electron neutrinos arriving from the sun was around 1/3 to 1/2 the number
⁴¹³ predicted by the Standard Solar Model. This became known as the solar neutrino
⁴¹⁴ problem and remained unresolved for around thirty years. This problem was resolved
⁴¹⁵ by the discovery of neutrino oscillation and mass. [1]

⁴¹⁶ 2.3 Neutrino Oscillations

⁴¹⁷ Neutrino oscillation was first predicted by Bruno Pontecorvo. It describes the phe-
⁴¹⁸ nomenon of a neutrino created with a specific lepton flavor (electron, muon or tau)
⁴¹⁹ that is later measured to have a different flavor. Neutrino oscillation is important
⁴²⁰ theoretically and experimentally due to the fact that this observation implies that the
⁴²¹ neutrino has a non-zero mass, which is not part of the original Standard Model of
⁴²² particle physics. [2]

423 2.3.1 Solar Oscillations and the Solar Neutrino Problem

424 The solar neutrino flux derived from Bahcall's Standard Solar Model is shown in figure
 425 2.1. Nuclear fusion and decay processes produce an abundant amount of neutrinos.
 426 The standard solar model predicts that these reactions produce several groups of
 427 neutrinos, each with differing fluxes and energy spectra. The figure also shows the
 428 ranges of detection of existing solar neutrino experiments in different shades of blue
 429 to illustrate that they sample different portions of the solar neutrino energy spectrum.
 430 Three of these experiments, plus a new one, are discussed below.

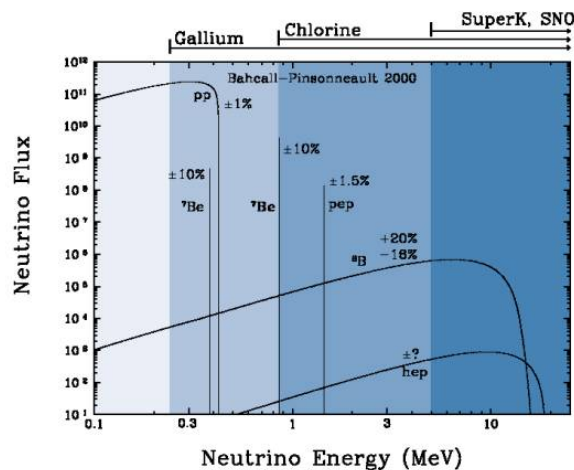


Figure 2.1: The Standard Solar Model

431 Since neutrinos rarely interact with matter, they pass through the sun and the earth
 432 undetected. About 65-billion neutrinos from the sun stream through every square
 433 centimeter on the Earth every second, yet we are oblivious to their passage in our
 434 every-day lives. [3]

435 The first experiment to detect the effects of neutrino oscillation was the Ray Davis's
 436 Homestake Experiment. The detector was stationed in the Homestake Gold Mine in
 437 Lead, South Dakota. It was 1,478 meters underground and was $380\ m^3$. The detector
 438 was filled with perchloroethylene. Perchloroethylene was chosen because of its high
 439 concentrations of chlorine. When an ν_e interacted with chlorine-37 atom, the atom
 440 would transform to argon-37 which was then extracted and counted. The neutrino
 441 capture reaction is shown in equation 2.1. Davis observed a deficit of about 1/3
 442 the flux of solar neutrinos that was predicted by Bahcall's Standard Solar Model.

- ⁴⁴³ The unexplained difference between the measured solar neutrino flux and model
⁴⁴⁴ predictions lead to the Solar Neutrino Problem. [4]



⁴⁴⁵ While it is now known that the Homestake Experiment detected neutrinos, some
⁴⁴⁶ physicist were weary of the results. Conclusive evidence of the Solar Neutrino Problem
⁴⁴⁷ was provided by the Kamiokande-II experiment, a water Cherenkov detector with
⁴⁴⁸ a low enough energy threshold to detect neutrinos through neutrino-electron elastic
⁴⁴⁹ scattering. In the elastic scattering interaction the electrons coming out of the point of
⁴⁵⁰ reaction strongly point in the direction that the neutrino was traveling, away from the
⁴⁵¹ sun. While the neutrinos observed in Kamiokande-II were clearly from the sun, there
⁴⁵² was still a discrepancy between Kamiokande-II and Homestake; The Kamiokande-
⁴⁵³ II experiment measured about 1/2 the predicted flux, rather than the 1/3 that the
⁴⁵⁴ Homestake Experiment saw.

⁴⁵⁵ The solution to the solar neutrino problem was finally experimentally determined
⁴⁵⁶ by the Sudbury Neutrino Observatory(SNO). The Ray Davis's Homestake Experiment
⁴⁵⁷ was only sensitive to electron neutrinos, and the Kamiokande-II Experiment was
⁴⁵⁸ dominated by the electron neutrino signal. The SNO experiment had the capability to
⁴⁵⁹ see all three neutrino flavors. Because of this, it was possible to measure the electron
⁴⁶⁰ neutrinos and total neutrino flux. The experiment demonstrated that the deficit was
⁴⁶¹ due to the MSW effect, the conversion of electron neutrinos from their pure flavor
⁴⁶² state into the second neutrino mass eigenstate as they passed through a resonance
⁴⁶³ due to the changing density of the sun. The resonance is energy dependent, and is
⁴⁶⁴ visible near 2MeV. The water cherenkov detectors only detect neutrinos above about
⁴⁶⁵ 5MeV, while the radiochemical experiments were sensitive to lower energy (0.8MeV
⁴⁶⁶ for chlorine, 0.2MeV for gallium), and this turned out to be the source of the difference
⁴⁶⁷ in the observed neutrino rates at the two types of experiments. Figure 2.2 shows
⁴⁶⁸ Homestake, Kamiokande-II and SNO experiments.

⁴⁶⁹ MSW Effect

⁴⁷⁰ The Mikheyev-Smirnov-Wolfenstein effect is a process which acts to modify neu-
⁴⁷¹ trino oscillations in matter. The presence of electrons in matter changes the energy

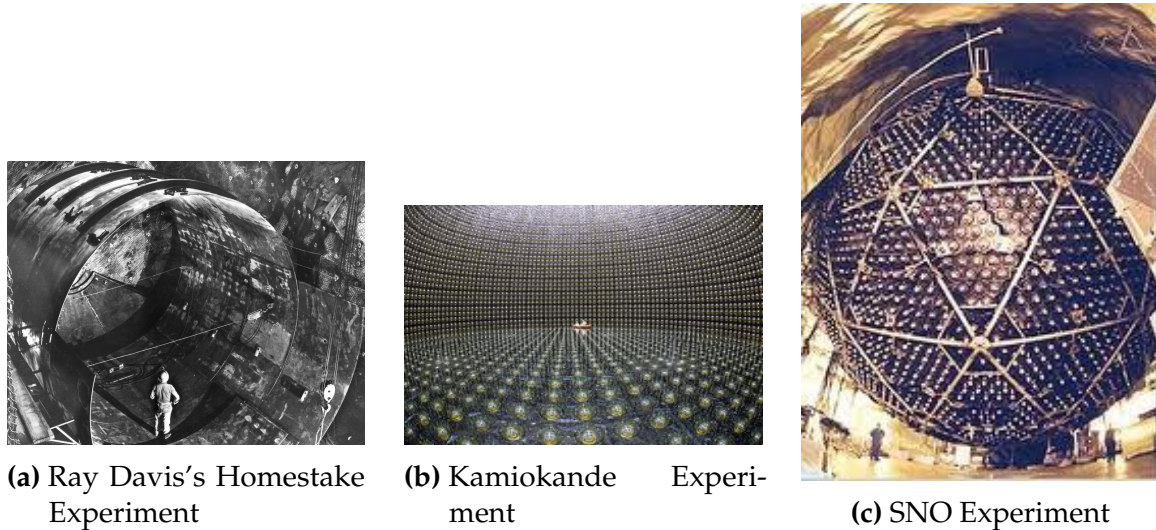


Figure 2.2: Solar Neutrino Experiments

472 levels of the mass eigenstates of neutrinos due to charged current coherent forward
 473 scattering of the electron neutrinos. This coherent forward scattering is similar to
 474 the electromagnetic process with respect to the refractive index of light in a medium.
 475 Because of this MSW Effect, neutrinos in vacuum have a different effective mass than
 476 neutrinos in matter and because neutrino oscillations depend on the squared mass
 477 difference of the neutrinos, the neutrino oscillations are different in matter than in
 478 vacuum. This effect is important at the sun where electron neutrinos are produced.
 479 The neutrinos of high energy leaving the sun are in a vacuum propagation eigenstate
 480 ν_2 that has a very small overlap with the electron neutrino $\nu_e = \nu_1\cos(\theta) + \nu_2\sin(\theta)$
 481 seen by the charged current reactions in Kamiokande-II and SNO. The discrepancy of
 482 the deficit between SNO, Kamiokande-II and Homestake is due to the energy of the
 483 solar neutrinos. The MSW effect "turns on" at about 2MeV and at lower energies, this
 484 MSW effect is negligible. [5]

485 **2.3.2 Atmospheric Oscillations and the Atmospheric Neutrino
 486 Anomaly**

487 Atmospheric neutrinos are neutrinos that stem from the decay hadrons coming from
 488 primary cosmic rays. The dominant part of the decay chain is shown in equations 2.2
 489 and 2.3

$$\pi^+ \rightarrow \mu^+ \nu_\mu \mu^+ \rightarrow e^+ \nu_e \bar{\nu}_\mu \quad (2.2)$$

490

$$\pi^- \rightarrow \mu^- \bar{\nu}_\mu \mu^- \rightarrow e^- \bar{\nu}_e \nu_\mu \quad (2.3)$$



Figure 2.3: Cosmic Ray Shower

491 Figure 2.3 shows the cosmic ray shower. In general, these neutrinos have energies
 492 from 1GeV to 100s of GeV and the ratio of ν_μ s to ν_e s equals to 2 (see equation 2.4)

$$R = \frac{(\nu_\mu + \bar{\nu}_\mu)}{(\nu_e + \bar{\nu}_e)} \quad (2.4)$$

493 There have been two types of detectors used to study atmospheric neutrinos: Water
 494 Cherenkov detectors and tracking calorimeters. Super-Kamiokande is the detector we
 495 will focus on. These atmospheric detector experiments measure the ratio of ν_μ to ν_e .
 496 They also measure the zenith angle distribution of the neutrinos. These experiments
 497 report a double ratio (shown in equation 2.5). This double ratio is the ratio measured
 498 in the detector to the ratio that's expected which is 2. If the double ratio equals to 1, the
 499 data agrees with the prediction. Various measurements from multiple experiments
 500 are shown in figure 2.4. Except for Frejus, all R measurements are less than 1. This
 501 discrepancy between the predicted R and the measured R became known as the
 502 Atmospheric Neutrino Anomaly.

$$R = \frac{(N_\mu / N_e)_{DATA}}{(N_\mu / N_e)_{SIM}} \quad (2.5)$$

503 Kamiokande-II has the the capability of measuring the direction of the incoming
 504 neutrinos. The expectation of atmospheric neutrino detection is that the flux be

Experiment	Type of experiment	R
Super-Kamiokande	Water Cerenkov	0.675 ± 0.085
Soudan2	Iron Tracking Calorimeter	0.69 ± 0.13
IMB	Water Cerenkov	0.54 ± 0.12
Kamiokande	Water Cerenkov	0.60 ± 0.07
Frejus	Iron Tracking Calorimeter	1.0 ± 0.15

Figure 2.4: Measurements of the double ratio for various atmospheric neutrino experiments

isotropic due to the fact that atmospheric neutrinos can reach the detector from all directions. Kamiokande-II noticed that muon-like data did not agree well with this expectation. At low energies approximately half of the ν_μ are missing over the full range of zenith angles. At high energies the number of ν_μ coming down from above the detector seems to agree with expectation, but half of the same ν_μ coming up from below the detector are missing. This anomaly can be easily explained by neutrino flavor oscillations. Due to the fact that the neutrino travels less distance coming straight down into the detector (about 15km) than coming up from the bottom of the detector(13000km) changes the probability of oscillation. The probability of oscillation for the muon neutrinos coming down into the detector is roughly zero, whereas for neutrinos coming up, the oscillation probability is $\sin^2(2\theta)$. Both the solar and atmospheric neutrino problems can be explained by neutrino oscillation so its fitting to derive this phenomenon mathematically. In the next two sections, two flavor and three flavor neutrino oscillation derivations will be explained.

2.3.3 Two Flavor Neutrino Oscillation Formulation

The flavor eigenstates can oscillate between each other because they are composed of an add-mixture of mass eigenstates(ν_1, ν_2). Figure 2.5 shows the mass and flavor eigenstates rotated by an angle θ which is the mixing angle.

In matrix form the wavefunctions are:

$$\begin{pmatrix} \nu_\mu \\ \nu_e \end{pmatrix} = \begin{pmatrix} \cos\theta & \sin\theta \\ -\sin\theta & \cos\theta \end{pmatrix} * \begin{pmatrix} \nu_1 \\ \nu_2 \end{pmatrix} \quad (2.6)$$

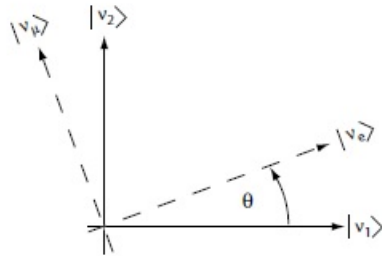


Figure 2.5: The flavor eigenstates are rotated by an angle θ with respect to the mass eigenstates

524 Applying the time evolution operator to ν_μ :

$$|\nu_\mu(t)\rangle = -\sin\theta|\nu_1\rangle e^{-i\frac{E_1 t}{\hbar}} + \cos\theta|\nu_2\rangle e^{-i\frac{E_2 t}{\hbar}} \quad (2.7)$$

525 where $E_1 = \sqrt{p^2 c^2 + m_1^2 c^4}$ and $E_2 = \sqrt{p^2 c^2 + m_2^2 c^4}$ and $p_1 = p_2$. For the time
526 being, let us assume $\hbar = c = 1$. With this assumption: $E_1 = \sqrt{p^2 + m_1^2}$ and $E_2 =$
527 $\sqrt{p^2 + m_2^2}$. The next modifications is to assume neutrinos are relativistic:

$$\gamma = \frac{E}{m_o c^2} = \frac{\sqrt{p^2 c^2 + m_o^2 c^4}}{m_o c^2} \gg 1 \quad (2.8)$$

528 because of this,

$$p \gg m_o \quad (2.9)$$

529

$$E = \sqrt{p^2 + m_o^2} = p\sqrt{1 + m_o^2/p^2} \simeq p + \frac{1}{2}\frac{m_o^2}{p} \quad (2.10)$$

530 where the binomial expansion is used. Now E_1 and E_2 can be written as:

$$E_1 \simeq p + \frac{1}{2}\frac{m_1^2}{p} \text{ and } E_2 \simeq p + \frac{1}{2}\frac{m_2^2}{p} \quad (2.11)$$

531 Now applying all these assumptions back into equation 2.7 gives us:

$$|\nu_\mu(t)\rangle = -\sin\theta|\nu_1\rangle e^{-i\left(p + \frac{1}{2}\frac{m_1^2}{p}\right)t} + \cos\theta|\nu_2\rangle e^{-i\left(p + \frac{1}{2}\frac{m_2^2}{p}\right)t} \quad (2.12)$$

$$|\nu_\mu(t)\rangle = e^{-i\left(p+\frac{1}{2}\frac{m_1^2-m_2^2}{p}\right)t} (-\sin\theta|\nu_1\rangle + \cos\theta|\nu_2\rangle) \quad (2.13)$$

⁵³² Substituting $\Delta m^2 = m_1^2 - m_2^2$ and $t = \frac{x}{c} = x$ and $e^{-iz} = e^{-i\left(p+\frac{1}{2}\frac{m_1^2}{p}\right)t}$ gives us:

$$|\nu_\mu(t)\rangle = e^{-iz} \left(-\sin\theta|\nu_1\rangle + \cos\theta|\nu_2\rangle e^{+ix\left(\frac{1}{2}\frac{\Delta m^2}{p}\right)} \right) \quad (2.14)$$

⁵³³ Finding the Probability for a $\nu_\mu \rightarrow \nu_e$:

$$P(\nu_\mu \rightarrow \nu_e) = |\langle \nu_e | \nu_\mu(t) \rangle|^2 \quad (2.15)$$

⁵³⁴ Remembering that $\langle \nu_i | \nu_j \rangle = \delta_{ij}$

$$\langle \nu_e | \nu_\mu(t) \rangle = e^{-iz} \left(-\sin\theta\cos\theta + \sin\theta\cos\theta e^{\frac{i\Delta m^2 x}{p}} \right) \quad (2.16)$$

⁵³⁵ Taking the absolute value squared gives us:

$$P(\nu_\mu \rightarrow \nu_e) = |\langle \nu_e | \nu_\mu(t) \rangle|^2 = e^{+iz} e^{-iz} \sin^2\theta \cos^2\theta \left(-1 + e^{\frac{i\Delta m^2 x}{p}} \right) \left(-1 + e^{\frac{-i\Delta m^2 x}{p}} \right) \quad (2.17)$$

⁵³⁶ Since the neutrino is relativistic we can set $p = E_\nu$ and change $x = L$. Also
⁵³⁷ recognizing the trigonometric relation $(1 - \cos 2\theta)/2 = \sin^2\theta$ the above equation
⁵³⁸ becomes:

$$P(\nu_\mu \rightarrow \nu_e) = \sin^2 2\theta \sin^2 \left(\frac{\Delta m^2 L}{4E_\nu} \right) \quad (2.18)$$

⁵³⁹ All that's left to do now is re-introduce \hbar and c doing this we get:

$$P_{\nu_\mu \rightarrow \nu_e}(L, E) = \sin^2 2\theta \sin^2 \left(1.27 \Delta m^2 \frac{L}{E_\nu} \right) \quad (2.19)$$

⁵⁴⁰ This equations has three important variables.

- The angle θ : This angle, as mentioned before, is called the mixing angle. It defines the difference between the flavor and the mass eigenstates. When $\theta = 0$ the mass and flavor eigenstates are identical and now oscillations occur.
- The mass squared difference, Δm^2 : Again $\Delta m^2 = m_1^2 - m_2^2$. The reason this is an important variable is because it implies that for neutrinos to oscillate, neutrinos must have mass. Furthermore, the mass squared difference also tells us that the neutrino mass eigenstates must be different.
- L/E: This is the variable that is of most interest to experimental physicists due to the fact that it is the variable that we set. L is the distance between the source and detector and E is the energy of the neutrino. For a given Δm^2 , the probability of oscillation changes with respect to L/E.

2.3.4 Three Flavor Neutrino Oscillation Formulation

Seeing the quantum mechanics involved in deriving the probability of a two flavor neutrino oscillation, it is now possible to formulate the three flavor neutrino oscillation. The three flavor neutrino oscillation formulation begins similarly to the two flavor, but there is the Pontecorvo-Maki-Nakagawa-Sakata matrix (PMNS) instead of the 2X2 matrix in the previous section. The PMNS matrix is show below:

$$\begin{pmatrix} c_{12}c_{13} & s_{12}c_{13} & s_{13}e^{-i\delta} \\ -s_{12}c_{23} - c_{12}s_{23}s_{13}e^{i\delta} & c_{12}c_{23} - s_{12}s_{23}s_{13}e^{i\delta} & s_{23}c_{13} \\ s_{12}s_{23} - c_{12}c_{23}s_{13}e^{i\delta} & -c_{12}s_{23} - s_{12}c_{23}s_{13}e^{i\delta} & c_{23}c_{13} \end{pmatrix} * \begin{pmatrix} e^{i\alpha_1/2} & 0 & 0 \\ 0 & e^{i\alpha_2/2} & 0 \\ 0 & 0 & 1 \end{pmatrix} \quad (2.20)$$

where $c_{ij} = \cos\theta_{ij}$ and $s_{ij} = \sin\theta_{ij}$

Following the same steps as before we get:

$$P_{\alpha \rightarrow \beta} = \delta_{\alpha\beta} - 4\sum Re(U_{\alpha i}^* U_{\beta i} U_{\alpha j} U_{\beta j}^*) \sin^2\left(\frac{\Delta m_{ij}^2 L}{4E}\right) 2\sum Im(U_{\alpha i}^* U_{\beta i} U_{\alpha j} U_{\beta j}^*) \sin\left(\frac{\Delta m_{ij}^2 L}{2E}\right) \quad (2.21)$$

The main things to notice here are δ_{ij} which is the CP violating term and has not been measured yet, and θ_{13} which has just been measured. CP violation is a violation

562 of the postulated CP-symmetry. CP-symmetry states that the laws of physics should
563 be the same if a particle were to be exchanged with its antiparticle and then if the left
564 hand side of a decay were switched with the right hand side.

565 **2.3.5 Reactor Oscillation**

566 Many experiments have searched for oscillation of electron anti-neutrinos produced at
567 nuclear reactors. Such oscillations give the value of the parameter θ_{13} . The KamLAND
568 experiment, started in 2002, has made a high precision observation of reactor neutrino
569 oscillation. Neutrinos produced in nuclear reactors have energies similar to solar
570 neutrinos, a few MeV. The baselines of these experiments have ranged from tens
571 of meters to over 100 km. On 8 March 2012, the Daya Bay team announced a 5.2σ
572 discovery that $\theta_{13} \neq 0$.

⁵⁷³ **Chapter 3**

⁵⁷⁴ **The MicroBooNE Experiment**

⁵⁷⁵ The purpose of this chapter is to discuss and understand the details of the MicroBooNE
⁵⁷⁶ detector. A thorough understanding of MicroBooNE and the technology behind liquid
⁵⁷⁷ argon time projection chambers is important for understanding results as well as
⁵⁷⁸ understanding how images were made for use in deep learning efforts that will be
⁵⁷⁹ outlined in later chapters.

⁵⁸⁰ **3.1 Liquid argon time projection chambers**

⁵⁸¹ Liquid Argon Time Projection Chambers (LArTPCs) are an exciting detector technol-
⁵⁸² ogy that provide excellent imaging and particle identification, and are now being
⁵⁸³ used to study neutrinos. The Time Projection Chamber (TPC) was first invented by
⁵⁸⁴ Nygren in 1974 [?] and the proposal for a LArTPC for neutrino physics was made
⁵⁸⁵ by Rubbia [?] in 1977 with the ICARUS collaboration implementing this concept [?].
⁵⁸⁶ A LArTPC is a three-dimensional imaging detector that uses planes of wires at the
⁵⁸⁷ edge of an active volume to read out an interaction. When a neutrino interacts with an
⁵⁸⁸ argon atom, the charged particles that are produced ionize the LAr as they travel away
⁵⁸⁹ from the interaction. By placing a uniform electric field throughout the LAr volume,
⁵⁹⁰ the ionization is made to drift towards a set of anode planes, which consist of wires
⁵⁹¹ spaced very closely together collecting the ionized charge, which is subsequently read
⁵⁹² out by electronics connected to the anode wires. The collected ionization creates a
⁵⁹³ spatial image of what happened in the detector on each anode plane. The position
⁵⁹⁴ resolution of the interaction along the beam direction (perpendicular to drift direction)
⁵⁹⁵ relies on the wire pitch, while the resolution in drift direction is dependent on the

596 timing resolution of the electronics used and the longitudinal diffusion in the volume.
 597 The drift time of the ionization relative to the time of the original signal allows the
 598 signal to be projected back along the drift coordinate, hence the name LArTPC. Having
 599 very small distances between each wire within an anode plane allows for very fine
 600 granularity and detail to be captured, and having multiple wire planes at different
 601 angles provides independent two-dimensional views that can be combined into a
 602 three dimensional picture of the interaction. Once the charge signal is created on the
 603 anode planes, software analysis packages identify particles in the detector by using
 604 deposited energy on the wires along their track length. The 30 year development of the
 605 ICARUS detector has led to LArTPCs being used as cosmic ray [?], solar neutrino [?]
 606 and accelerator neutrino [?] detectors. The ArgoNeuT experiment at Fermilab was
 607 the first United States based liquid argon neutrino program that has since produced
 608 short-baseline $\nu - Ar$ cross-section measurements in the NUMI beamline [?]. The
 609 MicroBooNE experiment is the second experiment in the US based LArTPC neutrino
 610 program and will be discussed thoroughly in the next sections. The next phases of
 611 the liquid argon neutrino program are under way and are the Fermilab Short Base-
 612 line Neutrino (SBN) program [?] and the Deep Underground Neutrino Experiment
 613 (DUNE) [6]. The SBN program will include three LArTPC detectors, including the
 614 MicroBooNE detector, on the Booster Neutrino Beam (BNB) to do multiple-baseline
 615 oscillation measurements. The detector closest to the beam will be the 40 ton Short
 616 Baseline Neutrino Detector (SBND) [?] at 150 m and the detector furthest is the 600 ton
 617 ICARUS T600 [?] detector positioned at 600 m. The DUNE collaboration will deliver
 618 a 30 GeV neutrino beam 1300 km from Fermilab to a 34 kiloton LArTPC detector
 619 at Homestake, SD. DUNE will study the leptonic CP phase, δ_{cp} , as well as measure
 620 neutrino and antineutrino oscillations.

621 3.2 The MicroBooNE Time Projection Chamber

622 MicroBooNE (Micro Booster Neutrino Experiment) is a 89 ton active volume (180 ton
 623 total mass) LArTPC which is then inserted into a cylindrical cryostat on axis of the
 624 Booster Neutrino Beam (BNB) stationed at Fermilab in Batavia, Illinois. Understanding
 625 LArTPC technology and detector physics is necessary to build a LArTPC the size of
 626 DUNE, and MicroBooNE has made many advances in developing this technology [7]
 627 [8].

MicroBooNE's Time Projection Chamber (TPC) is 10.3 m long (beamline direction), 2.3 m high and 2.5 m wide (which corresponds to the drift distance). The TPC is shown in figure ?? . MicroBooNE is the largest LArTPC currently running in the world [9]. This LArTPC has 3 wire planes: 1 plane that collects the ionization in the wires and is 0° to the vertical with 3456 wires spaced 3 mm apart, and 2 planes where the ionization drifts passed and induces a signal at $\pm 60^\circ$ to the vertical each with 2400 wires also spaced 3 mm apart. Each plane has a spacing also of 3 mm from eachother. The first two planes are the induction planes and the last is the collection. The 270 V/cm electric field of the TPC is created using 64 stainless steel tubes shaped into rectangles around the TPC and held in place by G10 to form a field cage. The cathode is charged at a high voltage of -70 kV and this voltage is stepped down across the field cage tubes using a voltage divider chain with an equivalent resistance of $240\text{ M}\Omega$ between the tubes. The field cage tubes are separated by 4 cm from center to center. The electron drift distance is 2.5 m in the x direction with a drift time of 2.3 ms. Maintaining high charge yield is done by continuously recirculating and purifying the argon. The purity is monitored using MicroBooNE's light collection system. Another use of the light collection system is initial timing and drift coordinate of the interaction.

MicroBooNE's light collection system is a crucial part for 3D reconstruction of all particle interactions in the LArTPC. The initial interaction time, t_0 , and initial drift coordinate, x_0 , are not known from the TPC alone. For beam events, the accelerator clock is used to determine t_0 of the interaction and the x_0 can be inferred using drift time. Non-beam events, however, do not have this capability, which is why scintillation light from an interaction is used. The $\nu - Ar$ interaction produces scintillation light which is collected by photomultiplier tubes (PMTs) which allows the exact time, t_0 of the neutrino interaction to be determined. The scintillation light created propagates within nanoseconds to the light collection system compared to the milliseconds it takes the ionized electrons from the interaction to reach the anode wire planes. Therefore we can precisely know where along the drift direction the particle interaction first took place. The scintillation light is also localized, so combining the PMT information with the wire plane information allows for cosmic background rejection happening outside the beam timing window.

The light collection system is made up of 32 Hamamatsu R5912-02mod cryogenic PMTs with a diameter of 8-inches. The PMTs are located behind the 3 wire anode planes and provides 0.85% photocathode coverage. Each PMT has an acrylic plate mounted in front of it that is coated with a wave-length shifting material called TPB.

663 The acrylic plates take in the scintillation light, at 128 nm, and re-emits it visible
664 wavelengths visible to the PMTs, with a peak at 425 nm.

665 Both the light collection system and the TPC create analog signal that is read out and
666 digitized by the electronics system. The process requires amplification and shaping of
667 the signal which then goes to the data acquisition (DAQ) software for writing of the
668 digitized data to disk. The anode plane wires are connected to detector specific circuit
669 boards (ASICS) that are submerged and operate inside the liquid argon volume. These
670 ASICS send amplified signal to 11 feed-throughs where further amplification of the
671 signal happens outside the cryostat. The signal is received by custom LArTPC readout
672 modules distributed over nine readout crates which do the digitization. The TPC wires
673 are digitized at 16 MHz then downsampled to 2 MHz. The TPC system reads out 4
674 frames of wire signal data per event, 1 frame before a trigger and 2 frames after the
675 triggered frame. The four frames allows for identification of a neutrino interaction as
676 well as cosmic background rejection. The process of digitization is similar for the light
677 collection system. Each PMT signal undergoes a shaping with a 60 ns peaking time
678 for digitization of multiple samples. The digitization occurs at 64 MHz but are not
679 read out continuously during the TPC readout time. Only shaped PMT signal samples
680 above a small threshold are read out and saved. Both the TPC and PMT readouts are
681 initiated via triggers on a separate trigger board located in a warm electronics crate.
682 The timing trigger is created by a timing signal from the BNB accelerator which is
683 shaped and sent to the trigger board. The PMT trigger is generated when the PMT
684 signal multiplicity is greater than 1 and the summed PMT pulse-height is more than 2
685 photo-electrons summed up over all PMT channels. When the trigger board gets both
686 a timing trigger and a PMT trigger in coincidence, at BNB trigger is then generated by
687 the board. This signal is then passed to all readout crates initiating the readout of data.
688 The data is then sent to the DAQ software which then saves the data to disk into one
689 event memory.

690 **3.3 MicroBooNE's Physics Goals**

691 **3.3.1 The low-energy excess**

692 The primary goal of the MicroBooNE experiment is to study and investigate the low-
693 energy excess seen in MiniBooNE 3.1. MicroBooNE has the capability of confirming or

denying this excess as electrons or photons due to the detector being in the same beam, having a similar baseline, and lastly the detector being able to clearly distinguish between electrons and photons. LArTPCs use the topology of events as well as energy loss near the vertex to differentiate between single e^- tracks and photon-induced induced pair production $\gamma \rightarrow e^+ e^-$, which wasn't possible in MiniBooNE, a Cherenkov detector. This technique has been shown in the ArogoNeuT detector [?] and a side by side comparison of both event types in a LArTPC can be seen in figure ?? . An excess in electrons would point towards new oscillation physics beyond the standard model, while photons would be within the standard model. MicroBooNE will observe a $4-5\sigma$ signal.

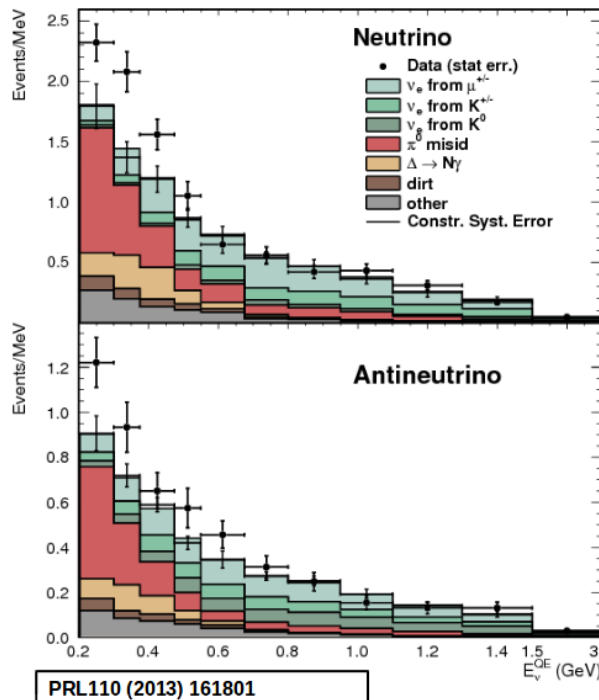


Figure 3.1: Low Energy excess seen in MiniBooNE

3.3.2 Cross sections

MicroBooNE's neutrino cross-section program will be the first $\nu - Ar$ cross-section in the 1 GeV energy range and one of only a few cross-section measurements of $\nu - Ar$ in the world. MicroBooNE is also the first liquid argon detector to collect the highest statistics sample of neutrino interactions. Investigating final-state-interactions in the 1GeV energy range provides information about short range nuclear correlations that affect the interpretations of neutrino oscillation experiment data.

711 One of the cross-section measurements MicroBooNE can make is an inclusive
 712 charged-current cross-section measurement (referred to as CC-inclusive). CC-inclusive
 713 events consist of a neutrino exchanging a W^\pm boson with an argon atom, producing a
 714 charged lepton and any number of other final state particles. In MicroBooNE's case, a
 715 CC-inclusive event will mostly have a defining muon track coming out of the vertex
 716 due to our neutrinos being predominately ν_μ s. A cross-section measurement is the
 717 energy dependent probability of $\nu - Ar$ interaction in the detector. Cross-sections
 718 however are independent of the intensity or focus of the particle beam so they can
 719 be compared among different experiments. A background for a CC-inclusive cross-
 720 section measurement are the neutral-current events that contain a pion. It is possible
 721 to have a neutral current interaction with a $\pi + p$ event signature that looks like a
 722 charged current $\mu + p$ event. Reconstruction tools implemented to date don't efficiently
 723 separate muons from pions. A common way to separate these two particles species is
 724 to implement a track length cut. On average, muons tend to have longer track lengths
 725 in LArTPCs so by requiring that the hypothesized lepton be above a threshold track
 726 length, it is possible to increase signal to background.

727 3.3.3 Liquid argon detector development

728 The last physics goal for the MicroBooNE collaboration is to provide important infor-
 729 mation regarding LArTPC technology. Being the first in large scare LArTPCs in the US,
 730 MicroBooNE will be albe to provide improvements to High Voltage (HV) distribution,
 731 Noise Characterization [?], and Michel Electron Reconstruction [8].

732 3.4 The Booster Neutrino Beam

733 The MicroBooNE detector is stationed at Fermi National Accelerator Laboratory
 734 (FNAL) where it receives neutrinos from both the Booster Neutrino Beam (BNB)
 735 and Neutrinos from the Main Injector (NuMI) beams. MicroBooNE is on-axis for the
 736 BNB and off-axis by 135 mrad for NuMI. For the purpose of this analysis, only data
 737 from the BNB was used. This section will discuss how neutrinos are created using the
 738 BNB. How these neutrinos are produced as well as their flux through the MicroBooNE
 739 detector is necessary for any analysis because of the systematic uncertainties the beam

⁷⁴⁰ introduces to a measurement. An aerial view of fermilab as well as the BNB is shown
⁷⁴¹ in figure 3.2

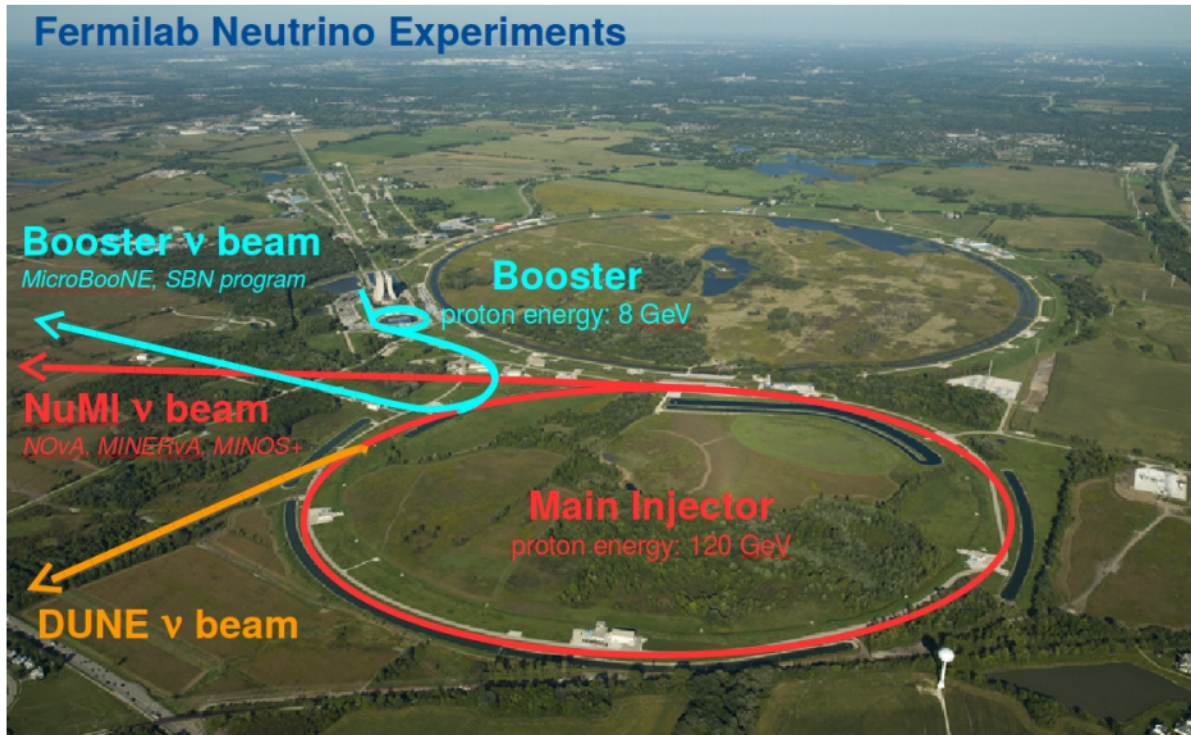


Figure 3.2: Arial view of the Main Injector and the Booster Neutrino Beam at Fermilab

⁷⁴² 3.4.1 Creating the Booster Neutrino Beam

⁷⁴³ The BNB is a very pure ν_μ beam, with only 0.6% contamination from ν_e s. The energy
⁷⁴⁴ also peaks around 700 MeV which is desired based on the probability of oscillation
⁷⁴⁵ equation which depends on the the value of L/E , where L is the distance of the
⁷⁴⁶ detector from the neutrino beam and E is the energy of the neutrino beam. L/E was
⁷⁴⁷ chosen to increase the probability of seeing neutrino oscillations in the MiniBooNE
⁷⁴⁸ Low Energy Excess (LEE) range based on the probability of oscillation equation, which
⁷⁴⁹ is $P_{\nu_\mu \rightarrow \nu_e}(L, E) = \sin^2 2\theta \sin^2 \left(1.27 \Delta m^2 \frac{L}{E} \right)$. The BNB collides 8.9 GeV/c momentum
⁷⁵⁰ protons from the FNAL booster synchrotron into a beryllium target which produces a
⁷⁵¹ high flux of neutrinos. The protons originate from H^2 gas molecules that are turned
⁷⁵² into H^- ions by a Cockcroft-Walton generator shown in figure ???. The H^- initially are
⁷⁵³ accelerated to 1MeV kinetic energy and are then passed to a linear accelerator using
⁷⁵⁴ alternating electromagnetic fields to increase their energy to 400MeV. The ions are
⁷⁵⁵ stripped of electrons by passing them through a carbon foil. The protons are bunched

756 into beam spills which contain $4 * 10^{12}$ protons in a $1.6 \mu\text{s}$ time window per spill. It's
757 at this point that the protons are directed towards the beryllium target. The amount
758 of protons directed towards the target (POT) is measured by two toroids upstream of
759 the target with an error of 2%. Beam intensity, timing, width, position, and direction
760 are monitored by beam position monitors, multi-wire chamber and resistive monitors.
761 The beryllium target is 71.1 cm long, 1.7 proton interaction lengths, and is 0.51 cm in
762 radius. The target is located inside a larger focusing electromagnet called the horn.
763 The horn is an aluminum alloy pulsed toroidal electromagnet. The pulsed current
764 peaks at 170 kA with a time-width of $143 \mu\text{s}$ which coincides with the protons arriving
765 on the target. The current flows from the inner conductor to the outer conductor
766 with a maximum magnetic field of 1.5 Tesla. The magnetic field focuses the charged
767 secondary particles produced by the p-Be interactions. The direction of current can be
768 switched to change the polarity of the secondary particles being focused creating a
769 beam of either primarily neutrinos, with positively charged secondary particles, or
770 antineutrinos.

771 Further down the beamline is a concrete collimator which absorbs particles not
772 necessary to the neutrino flux. The collimator is 214 cm long and 30 cm in radius.
773 After the collimator comes a 45 meter long, 1 meter radius, air-filled cylindrical decay
774 region which then ends in a beam-stop made of steel and concrete. The beam-stop
775 contains an array of gas proportional counters to detect muons. The BNB is shown in
776 figure 3.3.

777 **3.5 Event Reconstruction**

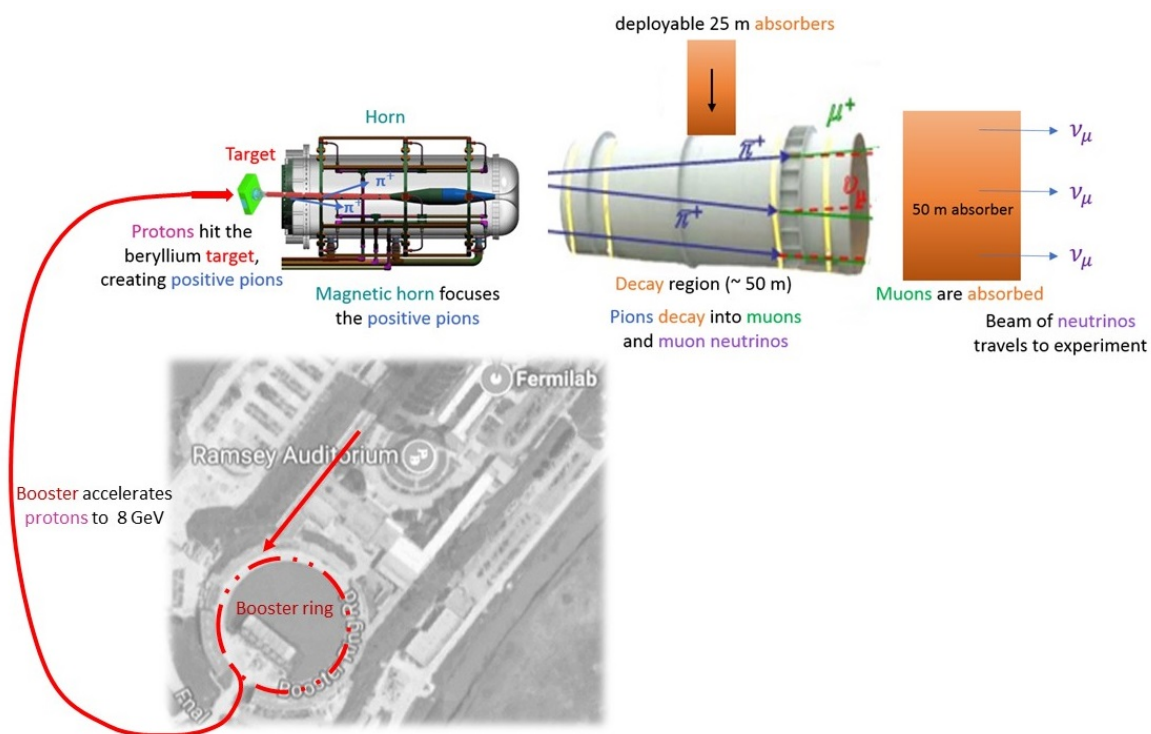


Figure 3.3: Aerial view of the Main Injector and the Booster Neutrino Beam at Fermilab

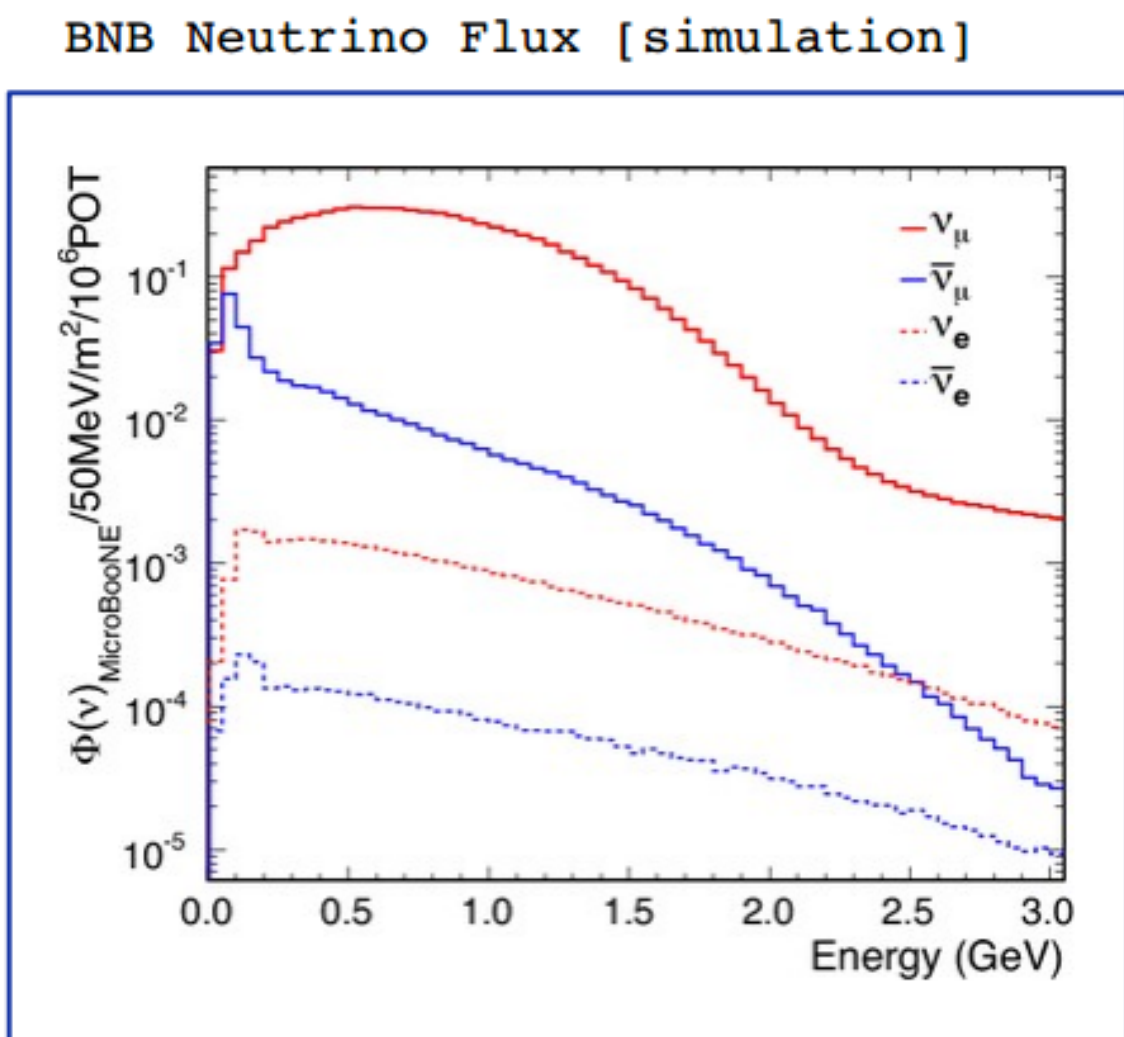


Figure 3.4: Energy spectrum of the Booster Neutrino Beam at Fermi National Laboratories

⁷⁷⁸ Chapter 4

⁷⁷⁹ Neutrino Identification: Finding ⁷⁸⁰ MicroBooNE's first Neutrinos

⁷⁸¹ The goal of the Neutrino Identification analysis was to positively identify BNB neutrino
⁷⁸² interactions in the MicroBooNE detector collected during the first days of running.
⁷⁸³ Neutrino event candidates were identified in part by using a cut on detected flash of
⁷⁸⁴ scintillation light during the $1.6 \mu\text{s}$ beam-spill length of the BNB as well as identifying
⁷⁸⁵ reconstructed object from the TPC that are neutrino like. After this selection, 2D
⁷⁸⁶ and 3D event displays were used for verification of the selection performance. This
⁷⁸⁷ selection was targeted to reduce the ratio of neutrino events to cosmic-only events from
⁷⁸⁸ the initial 1 neutrino to 675 cosmics to a ratio of 1 to 0.5 or better which is equivalent to
⁷⁸⁹ a background reduction by a factor of 1000 or more. These selected events were used
⁷⁹⁰ for MicroBooNE's public displays of neutrino interactions. A clearly visible neutrino
⁷⁹¹ interaction with an identifiable vertex and at least 2 tracks originating from the vertex
⁷⁹² was what the analysis focused on. This analysis wasn't optimized for high purity
⁷⁹³ or efficiency, but rather for very distinguishable neutrino interactions that could be
⁷⁹⁴ identified by the public.

⁷⁹⁵ 4.1 Flash Finding

⁷⁹⁶ Flash finding is the first step used in finding neutrino interactions. This section will
⁷⁹⁷ detail how optical information is reconstructed as well as analysis scripts and event
⁷⁹⁸ filters were used.

799 **4.1.1 Flash Reconstruction**

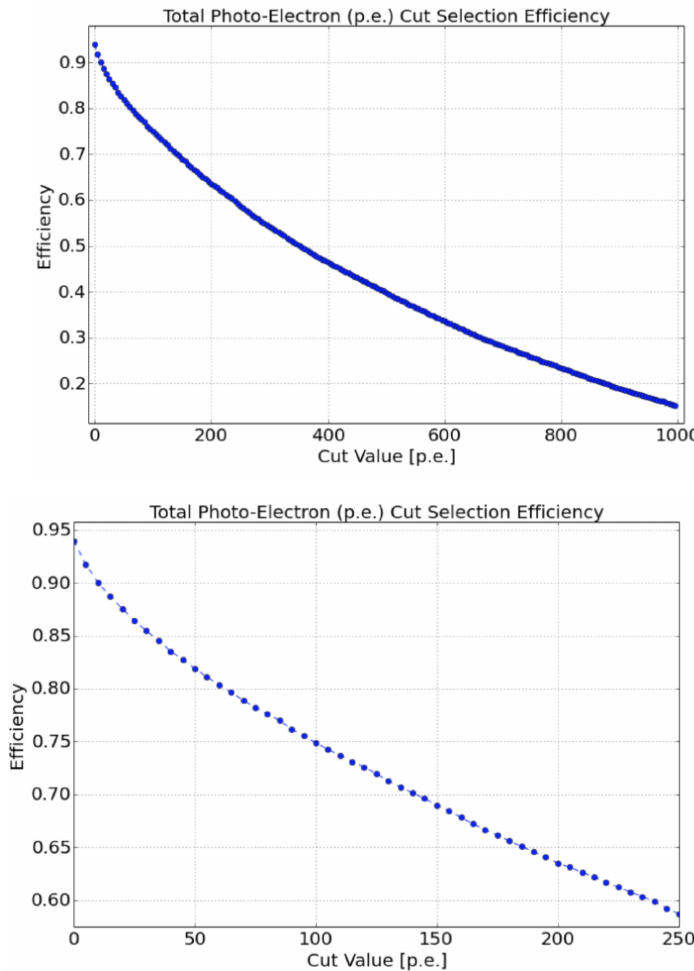
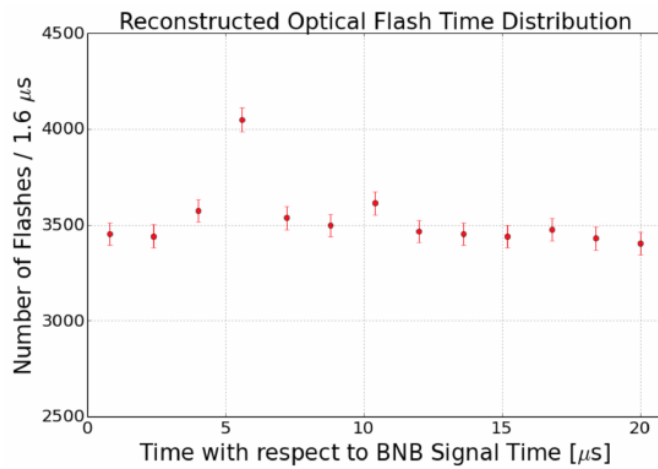


Figure 4.1: Efficiency for selecting beam events as a function of minimum total PE cut for all PE cuts as well as zoomed into interesting region.

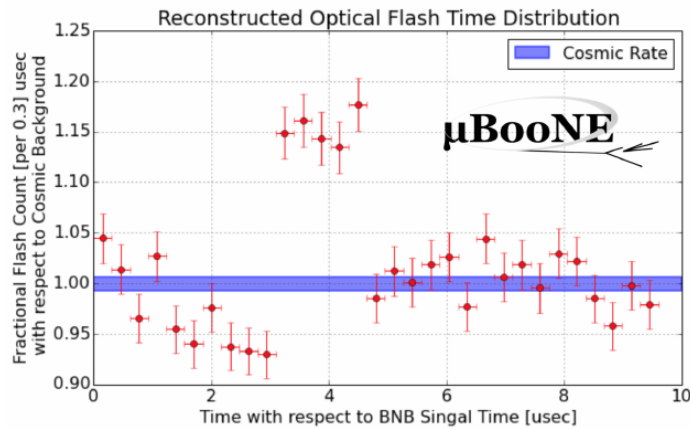
800 A flash is described as a collection of light seen at the same time within the detector.
801 They are then reconstructed by identifying signal from the PMTs above a specific
802 photoelectron (PE) threshold. These signals are called optical hits. Optical hits from
803 all the PMTs are then accumulated into $1\text{ }\mu\text{s}$ bins of time. If a specific bin is above a
804 set PE threshold, then the optical hits that overlap in time are the labeled as the hits
805 from the flash. All flash reconstructed properties like average time and x/y positions
806 are then found via the flash labeled optical hits. The total size of the flash is found by
807 summing up the total number of photoelectrons from all PMTs. Neutrino interactions
808 and cosmic muons will have a larger flash size compared to noise and other low-energy
809 backgrounds, therefore a total PE cut is used to reject these backgrounds. A total PE

⁸¹⁰ cut of 50 PE was deemed sufficient for this analysis. Figure 4.1 show the total PE
⁸¹¹ versus the selection efficency of selecting neutrino beam events.

⁸¹² 4.1.2 Beam Timing



(a) Predicted distribution of flash times with respect to trigger time for 1 day of data taking at nominal rate and intensity



(b) Measured distribution of flash times with a 50 PE threshold cut, with respect to trigger time. Shown as a ratio to the expected cosmic rate from off-beam data. A clear excess from neutrinos is visible between 3- 5 μ s after the trigger time.

⁸¹³ It is necessary to get the specific time from flashes if one uses flashes to filter out
⁸¹⁴ neutrino interactions coincident with the neutrino beam spill period and background.
⁸¹⁵ Before a filter can be applied, an understanding of the timing of the trigger and PMT

816 readout with respect to the arrival of neutrinos from the BNB. To do this, a $1.6 \mu\text{s}$
 817 window near the expected beamtime was created and verified by finding that the
 818 number of flashes was significantly above the cosmic-ray background flashes. Beam
 819 data during the first week of running, October 16th 2016 through October 22nd 2016
 820 and were used for a timing measurement. The total POT uses corresponds to roughly
 821 24 hours of data taking at nominal intensity ($4 \times 10^{12} \text{ ppp}$) and a 5 Hz repetition rate.
 822 Figure 4.2a shows size of the expected neutrino signal in time using Monte Carlo
 823 predictions and figure 4.2b shows the neutrino signal in data. The intensity in data is
 824 lower, however there can still be seen a significant excess above data.

825 **4.1.3 Event Rates**

826 Applying a 50 PE threshold cut inside a $1.6 \mu\text{s}$ window reduces the cosmic-ray passing
 827 rate to 0.8%. With a 5 Hz beam rate, this corresponds to 135 cosmics passing per
 828 hour. The neutrino passing rate for this filter is about 22 events per hour. To further
 829 increase the neutrino to cosmic ratio, TPC topology cuts were implemented and will
 830 be discussed in the following section.

831 **4.2 TPC Topology Selection**

832 In order to further reduce the background of cosmic events, two independent selection
 833 streams using TPC wire data reconstruction was implemented. The first using 2D
 834 reconstructed clusters, and the second using 3D reconstructed tracks. Both streams
 835 look for neutrino interactions in the active TPC volume which are identifiable by two
 836 or more tracks originating from the same vertex.

837 Both 2D and 3D channels were optimized using monte carlo simulation which
 838 used a 128 kV cathode voltage. Passing rates were calculated using a 0.008 efficiency
 839 factor for cosmic events passing to simulate the flash finding described in section 4.1.
 840 This efficiency factor was an overestimation and was just used to get a general feel of
 841 what signal and background rates we would actually see in data.

842 **4.2.1 Cosmic Tagging**

843 The first step in TPC selection was based on the geometry of cosmic tracks in an event.
844 The cosmic ray muon geometry tagger runs on 3D tracks and assigns a score to each
845 reconstructed track on the likeliness of the track originating from a cosmic. The cosmic
846 scores are detailed below:

- 847 • 1: The track is tagged as entering or exiting the TPC
- 848 • 0.95: The track is a delta ray associated with a tagged track
- 849 • 0.5: The track is either entering or exiting, but not both
- 850 • 0.4: The track is entering or exiting through the Z boundary
- 851 • 0: The track isn't tagged

852 Clusters are assigned either a 0 or 1, 1 being a cosmic. In simulation, 90% of cosmics
853 are tagged as cosmics. These tracks are no longer considered when looking for a
854 neutrino topology. Requiring that the tracks be contained in turn affects the neutrino
855 efficiency by 20%. The algorithm checks that each track is contained within a boundary
856 region of 10 cm from all sides of the TPC. This boundary region was optimized via
857 handscanning of experimental data.

858 As can be expected, cosmic tagging is more efficient in the 3D channel (tracks) than
859 the 2D channel (clusters) because the reconstructed tracks can use the full 3D position
860 information of the entering and exiting points while the 2D channel mainly use the
861 reconstructed x position of the cluster which is associated to timing.

862 Cosmic tagging uses timing information to reject tracks and clusters that are outside
863 of drift window. The drift window for 128 kV is $1.6 \mu\text{s}$ while for 70 kV, the actual
864 voltage MicroBooNE is running at, is $2.3 \mu\text{s}$. Due to this variation between simulation
865 and data, we expect to see $2.3/1.6 = 1.44$ times more cosmic induced tracks or clusters
866 in the drift window.

867 **4.2.2 2D Cluster Selection**

868 This selection was spearheaded by myself and Katherine Woodruff. After looking at
869 experimental cosmics data, 2D clustering performs well, while 3D track reconstruction
870 is affected by more variations in simulation, for example noise filters. This was the

871 motivation for having a selection only on 2D clusters in the collection (Y) plane. As
872 stated previously, the goal of this analysis was to find identifiable neutrino interactions
873 for use in public event displays, in future analyses, the 3D track reconstruction has
874 been modified to further increase the tracking efficiency and has more information
875 that just the clusters. For this analysis, however, 2D cluster information was sufficient
876 enough for neutrino selection.

877 **Primary Cuts**

878 The first cuts were used to select which clusters to consider. First the clusters must
879 have at least ten hits on the collection plane and have a cosmic tagging score < 0.4.
880 Only events that have at least two clusters that satisfy these primary cuts continue on.

881 After the initial cosmic tagging is applied, the following cuts are used to further
882 separate identifiable neutrinos from background cosmics.

883 The next cut was to remove long, vertical clusters. This was applied after seeing
884 that most cosmic induced clusters passing were long with high angles, while neutrino
885 induced clusters were mainly forward going. We required a good cluster to either
886 have a projected start angle less than 30 degrees from the z axis or be less than 200
887 wires long. The length cut was added to make sure we don't cut any short high angle
888 clusters that can correspond with a proton, or other highly ionizing particle associated
889 with a long muon cluster. The 200 wire cut roughly equates to 0.6 m in the z direction,
890 with a 3 mm wire pitch. Also, the projected angle is defined by $\tan \alpha = \Delta T / \Delta W$ where
891 T is the time ticks and W is the wires.

892 The last cut requires the clusters to be either 30 time ticks or 30 wires. This cut was
893 applied to reduce small delta rays associated with a cosmic without removing proton
894 clusters associated with a long muon cluster, which saves ideal neutrino events that
895 have both a long minimum ionizing muon like cluster and a short highly ionizing
896 proton like cluster.

897 **Secondary Cuts**

898 The secondary cuts look to match long, low-angle clusters with short, high-charge
899 clusters. Only clusters that have passed previous cuts are used. First clusters with
900 length greater than 100 wires are chosen, which is approximately 0.3 m in the z

Cluster set	No Cuts	Primary Cuts	Secondary Cuts
Neutrinos only	570	303	32
Cosmics only (no flash)	308,016	291,879	602
Cosmics only (w/ flash)	2464	2335	5
Neutrinos/Cosmics	0.23	0.13	6.4

Table 4.1: Passing rates for 2D cluster cuts for neutrino on MC set and a cosmic only MC set. First column shows event rates with no cuts applied to both sets. Columns two and three show event rates after primary and secondary cuts are applied. Line three shows the second line scaled with the flash finding factor of 0.008. All events are normalized to per day assuming we are running at 5 Hz.

901 direction. Then we search for any cluster that is within approximately 3 cm (10 wires
 902 and 30 time ticks) away from the low-z end of the long cluster. This cluster must also
 903 be shorter than the first. In our reconstruction, the start and end point of a cluster can
 904 be swapped so both ends of the short cluster are compared to the long cluster.

905 Now that there is a vertex match, cuts based on charge and projected opening angle
 906 are implemented. We require the short cluster to have a higher start charge than the
 907 long cluster or the long cluster be longer than 500 wires. Start charge is defined as
 908 the charge on the first wire in ADC counts. The projected opening angle must also
 909 be between 11 and 90 degrees. This last cut is intended to remove clusters that are
 910 entirely overlapping or are part of the same long track. The resulting neutrino/cosmic
 911 event rate per day is shown in table 4.1. Figures 4.3 and 4.4 shows the percentages of
 912 clusters that pass each primary and secondary cuts.

913 4.2.3 3D Tracks and vertices Selection

914 The neutrino selection for the 3D channel was based on a reconstructed vertex and
 915 two tracks. All vertices and tracks were looped over that had a cosmic tag score < 0.4
 916 and the distances below were calculated:

- 917 • d : distance between the start points of the two tracks.
- 918 • d_1 : distance between vertex and start of track 1.
- 919 • d_2 : distance between vertex and start of track 2.

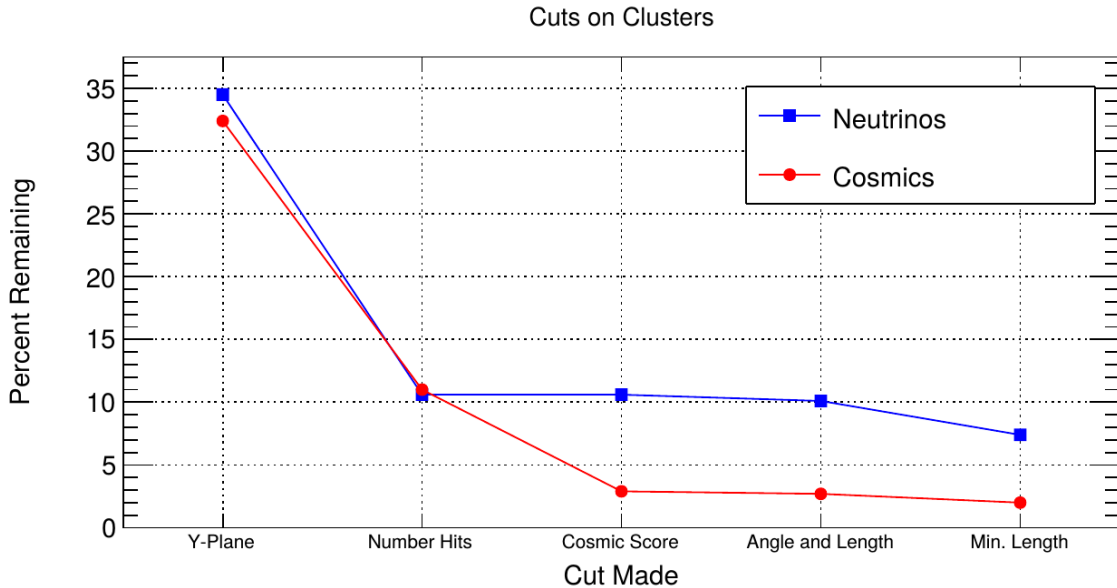


Figure 4.3: Percent of good clusters remaining for neutrinos and cosmics after the primary cuts were applied. This is relative to total number of initial clusters.

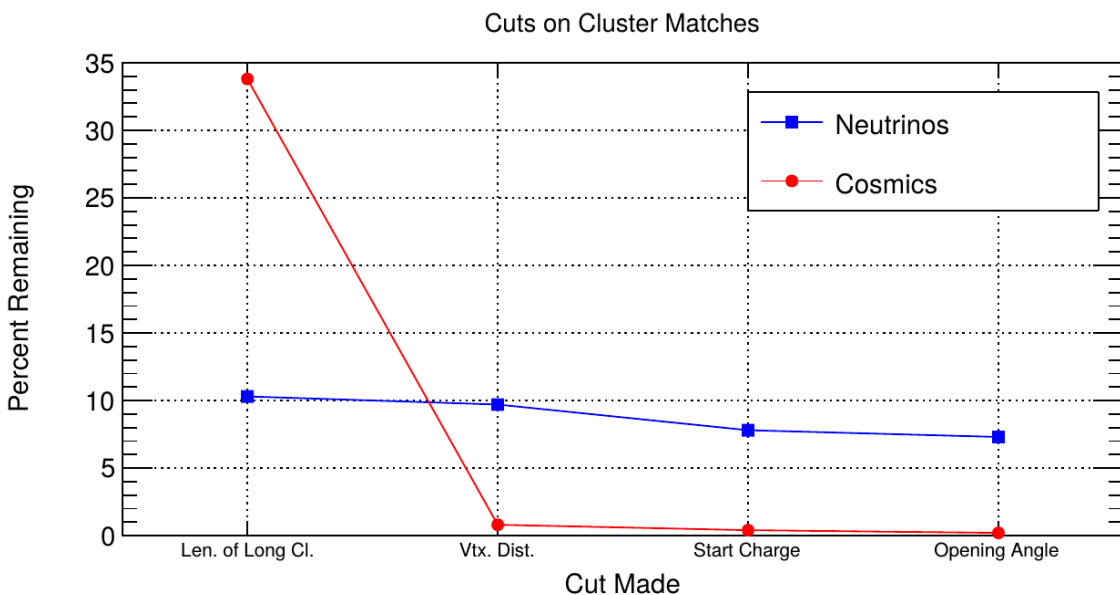


Figure 4.4: Percent matched cluster pairs remaining for neutrinos and cosmics after secondary cuts applied. This is relative to the number of events that contain clusters which pass the primary cuts.

920 The maximum distance of all three is then selected as the important characteristic per
921 trio. The best trio is the one that has the smallest maximum distance. The $\min(\max_d)$
922 for all trios in an event were plotted for BNB neutrino events and for cosmics to
923 find the best cut value for each tracking algorithm. The distribution of $\min(\max_{d,i})$
924 is smaller for neutrinos than for cosmics. The cut values for different tracking and
925 clustering algorithms are shown below. These cut values were chosen to minimize the
926 cosmic background to 20%.

- 927 • trackkalmanhit with cccluster $\min(\max_{d,i}) < 3$ cm.
928 • trackkalmanhit with pandoraNu $\min(\max_{d,i}) < 4.5$ cm.
929 • pandoraNu with cccluster $\min(\max_{d,i}) < 5$ cm.

930 4.2.4 TPC Updates

931 After doing a visual hand-scanning of the first beam data processed with the filters
932 detailed above, the events passing had a larger contamination of background than
933 expected. This was mainly in part due to the reconstruction performing better on
934 simulation than on data. Due to this, additional cuts on both streams needed to be
935 implemented in order to increase signal/background ratio. These cuts were added on
936 top of the filters described above and further reduce the event count.

937 2D Filter Updates

938 The main background observed in the 2D filter were Michel events, where the muon
939 and electron formed two connected clusters. These events were rejected by comparing
940 the start and end charge deposition of the long cluster (i.e muon particle). The start
941 charge deposition must be less than the end charge deposition. This cut is implemented
942 because muons have a higher ionizaiton loss at the end.

943 3D Filter Updates

944 It was seen that cosmic tracks can often originate or end at the same point, therefore
945 faking a signal. Cosmic tracks, however, are mostly vertical. By requiring the angle
946 of the longer track have a cosine greater than 0.85 with respect to the z-axis as well

947 as requiring the longer track to have a length greater than 10 cm, we can reduce this
948 background.

949 **4.3 Conclusion**

950 After proccesing these filters in parallel, it was shown that the 3D filter had a higher
951 purity than the 2D filter because of the higher cosmic rejection being used due to 3D
952 reconstruction. The 2D filter is blind to track entering/exiting from the top or bottom
953 of the TPC. Although the 3D filter had a higher purity, the 2D filter was still able to
954 find identifiable events in data that were used as public event displays. A sample of
955 event displays are shown in figures ?? and ??.

956 **Chapter 5**

957 **CC-Inclusive Cross Section Selection**
958 **Filter**

959 The CC-Inclusive cross-section selection I and selection I modified filters used in this
960 analysis will be described in the following sections below. These filters are an expansion
961 of the Neutrino ID filter. The work done in this thesis was to further improve these
962 selections by increasing both efficiency and purity as well as increasing acceptance
963 without further affecting the kinematic distributions of the selected neutrino events.

964 MicroBooNE requires fully automated event reconstruction and selection algorithms for use in the many physics measurements being worked on to date due to
965 the large data rate MicroBooNE receives. Being able to automatically pluck out the
966 neutrino interaction among a sea of cosmics proved to be challenging but was accomplished.
967 MicroBooNE has developed two complementary and preliminary selection
968 algorithms to select charged-current $\nu_\mu - Ar$ interactions. Both are fully automated
969 and cut based. The results of this thesis will focus on selection I and selection I modified
970 and will focus on further improving these algorithms using Convolutional Neural
971 Network (CNN) implementations. These selections identify the muon from a neutrino
972 interaction without biasing towards track multiplicity. To combat cosmic and neutral
973 current background, the analysis is strongly biased towards forward-going long tracks
974 which are contained. This limits phase space and reduces acceptance.
975

976 5.1 Data and MC Processing Chain

977 The data used for this analysis were based on hardware and software triggers. Events
978 used came from the *BNB_INCLUSIVE* and *EXT_BNB_INCLUSIVE* streams and were
979 used for signal and background. The *BNB_INCLUSIVE* stream is chosen by requiring
980 that the hardware trigger bit is fired and that the event passed an optical software
981 trigger within a BNB spill timing window. The *EXT_BNB_INCLUSIVE* stream requires
982 the EXT hardware trigger to fire as well as pass the same optical software trigger
983 within a BNB spill size timing window similar to the *BNB_INCLUSIVE*.

984 The two MC samples used in this analysis and for determining selection efficiencies
985 and purities were GENIE BNB neutrino interactions with CORSIKA cosmic ray overlay
986 within the readout window and inTime CORSIKA cosmic rays. The MC samples
987 generated used *uboonecode v04_36_00* and are based on the following packages:

- 988 • larsoft v04_36_00
- 989 • GEANT v04_09_06_p04d
- 990 • GENIE v02_08_06d
- 991 • GENIE xsec v02_08_06a
- 992 • pandora v02_03_0a
- 993 • CORSIKA v07_4003

994 Both data and MC samples were processed using the same reconstruction release,
995 *uboonecode v05_08_00* and the fcl files used for reconstruction are listed below:

- 996 • MC fcl files
 - 997 – reco_uboone_mcc7_driver_stage1.fcl
 - 998 – reco_uboone_mcc7_driver_stage2.fcl
- 999 • Data fcl files
 - 1000 • reco_uboone_data_Feb2016_driver_stage1.fcl
 - 1001 • reco_uboone_data_Feb2016_driver_stage2.fcl

1002 On top of the hardware and software triggers, the data also had to pass more
1003 criteria to be identified as part of the good run list. The criteria is detailed below.

- 1004 • **Detector conditions:** the detector has to be in a good operating condition. The
1005 detector conditions are read from the slow monitoring database and are required
1006 to be within the alarm thresholds. The variables of interest for events passing
1007 the good run list criteria include DAQ, PMT, HV, Drift HV, wire bias, electron
1008 lifetime and detector power. These conditions need to be met on a run-by-run
1009 basis in order to pass the selection.
- 1010 • **Data quality:** normal and stable behavior for basic reconstruction quantities.
1011 These reconstruction variables include average number of tracks, hits, and flashes
1012 in each event, the average length of tracks, the average amplitude and area of
1013 hits, the average PE and the average spread of each one of these quantities.
- 1014 • **Beam Conditions:** the BNB must be on and stable and the POT per spill needs
1015 to above the intensity threshold. Beam quality conditions include checking the
1016 fraction of proton beam interacting within the target, the horn current, and the
1017 intensity of protons per spill. The final sample is $5 * 10^{19}$ and a per-spill intensity
1018 of $4 * 10^{12}$
- 1019 • **Run processed:** the full run must be processed completely without missing
1020 subruns or crashes in the data processing.

1021 The selection begins with a cut that requires an optical flash greater than 50 photo
1022 electrons (PE) in the $1.6 \mu\text{s}$ beam window. Next, two or more 3D reconstructed tracks
1023 must be within 5 cm from a 3D reconstructed vertex. The most forward going track
1024 vertex-track association is then selected for further cuts. The vertex from the chosen
1025 association must be in the fiducial volume, and the longest track from this association
1026 must be matched to a flash 80 cm in z. Lastly the longest track must be contained and
1027 longer than 75 cm.

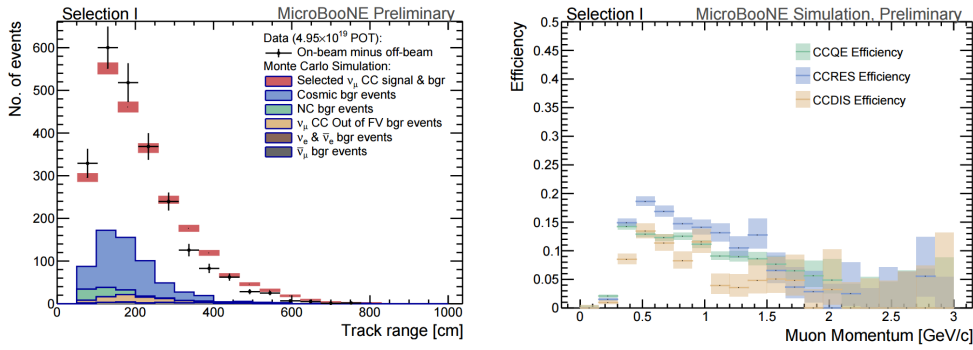
1028 5.2 Normalization of data and MC

1029 The off-beam sample is used to measure beam unrelated backgrounds. For normaliza-
1030 tion, one needs the total number of BNB spills (N_{BNB}) and the total number of external
1031 triggers. The BNB spills used need to pass the beam quality cuts. The normalization
1032 factor is then N_{BNB} / N_{EXT} which is 1.23.

1033 To normalize generated BNB MC events to POT, we used the following:

- 1034 • $5 * 10^{19} POT = 41524.3$ generated events

1035 where this scaling factor only applies to mcc7 generated events. The inTime cosmic
 1036 sample is normalized with respect to the open cosmic sample so an understanding
 1037 of both is necessary. The POT per beam spill for mcc7 BNB samples is $5 * 10^{12}$. To
 1038 calculate how many spills are necessary to produce a specific POT one would multiply
 1039 the total POT by the average 1/POT per spill. For a total POT of $5 * 10^{19}$ the amount
 1040 of spills necessary is $\frac{5*10^{19}}{5*10^{12}} = 1 * 10^7$. This is only one in ~ 241 events therefore each
 1041 cosmic event needs to be scaled up by a factor of 240.8 when comparing to BNB
 1042 MC. For inTime cosmics however, two filters are applied to reduce computing and
 1043 processing time and only leave cosmics that will interact within the detector. The
 1044 passing rate after these two filters is 0.02125, therefore the total inTime cosmic scaling
 1045 factor to compare inTime cosmics to BNB is $0.02125 * 240.8 = 5.12$.



(a) Track range distribution of selection I

(b) Selection efficiency as a function of the true muon momentum

Figure 5.1: 5.1a Track range distribution for selection I. The track range is defined as the 3D distance between the start and end of the muon candidate track. No data is shown below 75 cm due to the track length cut described previously. 5.1b Efficiency of the selected events by process quasi-elastic (QE), resonant (RES), and deep-inelastic (DIS). Statistical uncertainty is shown in the bands and the distributions are a function of true muon momentum. The rise of the efficiency between 0 GeV and 0.5 GeV is due to the minimum track length cut and the decreasing efficiency for higher momentum tracks is caused by the containment requirement.

1046 5.3 Optical Software Trigger and Reconstruction

1047 5.3.1 Software Trigger

1048 Most of the BNB spills from the accelerator do not have a neutrino interaction in
1049 MicroBooNE. To save computation resources and reduce data-rates, we require a
1050 burst of light in the light collection system in coincidence with the 1.6 μ s beam spill.
1051 Requiring light activity in coincidence with the beam spill eliminates the vast majority
1052 of triggers with no neutrino interaction in the detector, however, it doesn't guarantee
1053 the activity in the detector is a neutrino interaction since a cosmic ray can interact in
1054 coincidence with the beam spill as well.

1055 To implement this, a software trigger was used on the PMT waveforms to decide
1056 whether or not to keep that event. The software trigger is implemented after the event
1057 builder combines data from the PMTs and triggers into a single event. The software
1058 trigger uses the digitized output of the 32 PMT channels in the light collection system.
1059 Only the waveform region in coincidence with the beam spill is used to search for
1060 possible triggers. For each PMT, a waveform is found by taking the difference of ADC
1061 values is calculated between t and $t + s$. This waveform is then scanned for ADC
1062 values above a threshold X_0 . Once an ADC is above this threshold, a discriminator
1063 window is opened for a fixed number of time ticks (W_0). If the ADC count within this
1064 window W_0 is greater than a second larger threshold X_3 , a final window of width W_3
1065 is opened. The max ADC value within this final window is set as the peak amplitude
1066 for the PMT and then summed across all 32 PMTs and set to the variable PHMAX. The
1067 software trigger places a final cut on the PHMAX variable to decide whether or not
1068 to keep the event. The thresholds were found by the Trigger task force using Monte
1069 Carlo Studies and are as follows:

- 1070 • $X_0 = 5$ ADC
- 1071 • $X_3 = 10$ ADC
- 1072 • $W_0 = 6$ Ticks
- 1073 • $W_3 = 6$ Ticks
- 1074 • PHMAX cut = 130 ADC

1075 5.3.2 Flash Reconstruction

1076 MicroBooNE collects light from each of the 32 PMTs either in a continuous readout
 1077 window of $23.4 \mu\text{s}$ activated by a beam gate signal on the trigger board, or in discrimi-
 1078 nated pulses of $\sim 1 \mu\text{s}$ duration activated if the ADC count for any PMT goes above 80
 1079 ADC count. These two formats are saved as output waveforms and put onto an event.
 1080 Additionally, each PMT can provide two output streams, high-gain ($\sim 20 \text{ ADC/PE}$)
 1081 and low-gain ($\sim 2 \text{ ADC/PE}$) channels. The first step in the reconstruction is to merge
 1082 both these channels into a “saturation corrected waveform” which uses information
 1083 from the low-gain waveform to correct for saturating high-gain pulses.

1084 The saturation corrected waveform in the continuous readout window is used to
 1085 reconstruct optical hits. Each PMT’s waveform is scanned for hits then a threshold
 1086 based hit reconstruction algorithm is applied which requires pulses of a minimum
 1087 area in order to be reconstructed. Each reconstructed hit is associated to a PMT, a time
 1088 in μs , and a PE count.

1089 Once hits are reconstructed for all 32 PMTs, all PMT information is then combined
 1090 into optical flashes which represent optical information seen by the PMTs from interac-
 1091 tions in the detector. Each flash has information on total light seen per interaction, the
 1092 distribution of the light across all 32 PMTs, the flash time with respect to the trigger
 1093 time of the flash, and lastly, the spacial information of the flash in Y-Z plane of the
 1094 detector. These flashes are reconstructed by requiring that there is a $\sim 1 \mu\text{s}$ coincidence
 1095 between the reconstructed hits in all 32 PMTs. The total PE is summed up among
 1096 all coincident hits across the PMTs and if the total PE is greater than 2 PE, a flash is
 1097 reconstructed. There are also safe guards in place to take care of late scintillation light.

1098 Figure 5.2 shows the time distribution of reconstructed optical flashes using the
 1099 BNB continuous stream. You can see a clear excess in coincidence with the expected
 1100 arrival time of neutrinos. The same flash reconstruction that was used in the cc-
 1101 inclusive filter detailed here was used to create this plot in data.

1102 5.3.3 Beam Window

1103 Figure 5.3 shows the distribution of flashes for on-beam, off-beam and various MC
 1104 samples. The software trigger has been applied to these samples. The pile-up seen just
 1105 after $0 \mu\text{s}$ is a feature of the flash finding algorithm and consists of low PE flashes and

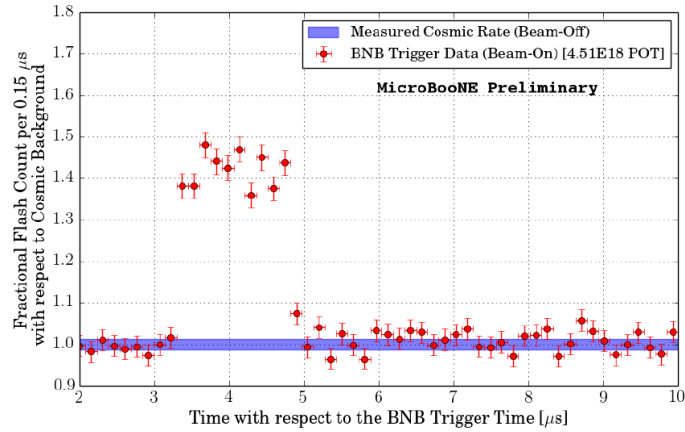


Figure 5.2: Time distribution of reconstructed optical flashes with a PE value of 50 or more for a sample of BNB unbiased triggered events.

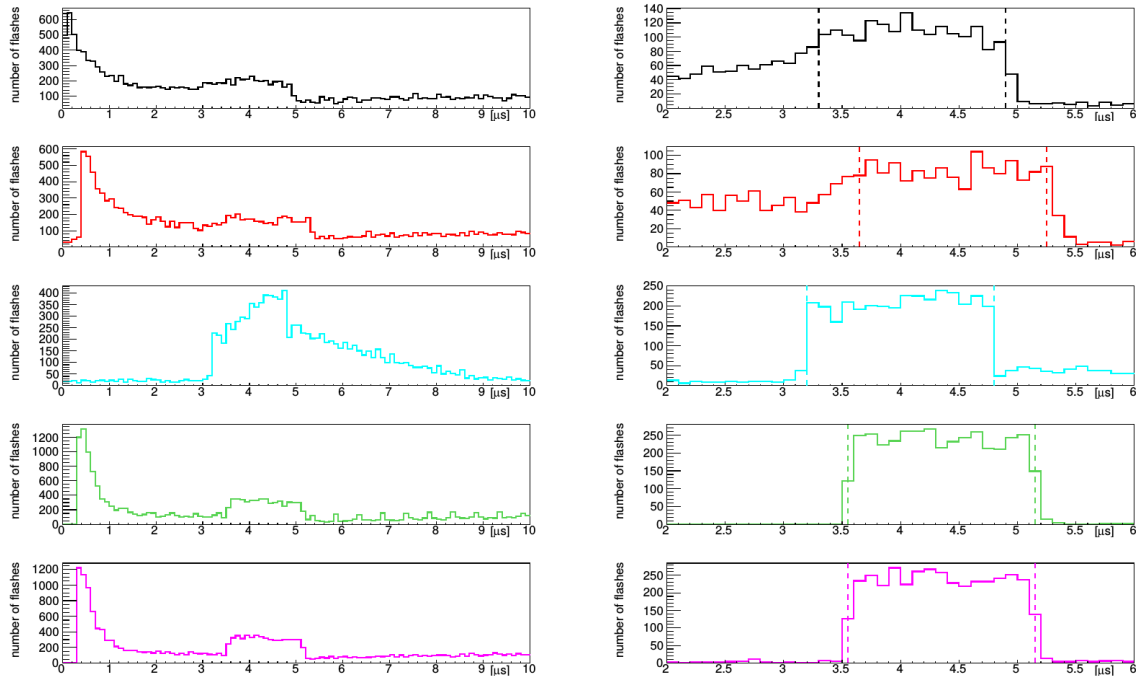


Figure 5.3: Flash time distribution for all flashes (left plot) and flashes $> 20\text{PE}$ (right plot). The different curves are as follows: on-beam data (black), off-beam data (red), CORSIKA inTime MC (light blue), BNB only MC (green), and BNB+Cosmic MC (purple). The dashed vertical lines mark the time window that was chosen for each sample

1106 is removed in the second column of distributions with a low 20 PE threshold cut. The
1107 plots show that the time window for the distributions are shifted a small amount from
1108 each-other. This is caused by different hardware configurations per sample. Using
1109 these distributions, the windows chosen per sample are as follows:

- 1110 • On-Beam: 3.3 to 4.9 μ s
 - 1111 • Off-Beam: 3.65 to 5.25 μ s
 - 1112 • CORSIKA inTime: 3.2 to 4.8 μ s
 - 1113 • BNB only: 3.55 to 5.15 μ s
 - 1114 • BNB+Cosmic: 3.55 to 5.15 μ s
- 1115 Each window has a width of 1.6 μ s.

1116 5.4 TPC Reconstruction

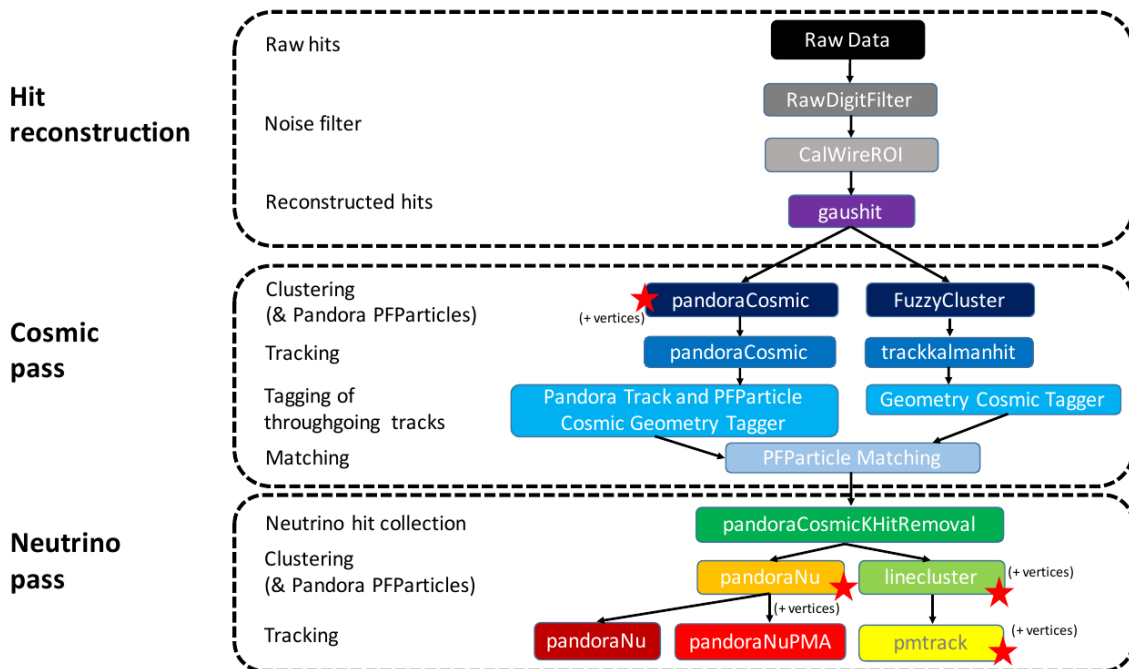


Figure 5.4: Reconstruction chain run on both data and MC. The red stars mean that the algorithm returns reconstructed 3D vertices.

₁₁₁₇ Figure 5.4 summarizes the reconstruction chain applied to both MC and data for
₁₁₁₈ this analysis. After the hit reconstruction, a cosmic pass is applied which removes all
₁₁₁₉ hits associated to through-going tracks. A description of these TPC reconstruction
₁₁₂₀ algorithms will be detailed below.

₁₁₂₁ **5.4.1 Hit Reconstruction**

₁₁₂₂ **5.4.2 Clustering**

₁₁₂₃ **5.4.3 Pandora**

₁₁₂₄ **5.4.4 Trackkalmanhit**

₁₁₂₅ **5.4.5 Cosmic Hit Removal**

₁₁₂₆ **5.4.6 Projection Matching Algorithm**

₁₁₂₇ **5.4.7 Calorimetry**

₁₁₂₈ **5.5 Event Selection**

₁₁₂₉ **Chapter 6**

₁₁₃₀ **Background on Convolutional Neural
1131 Networks**

₁₁₃₂ Convolutional neural networks (CNNs) have been one of the most influential inno-
₁₁₃₃ vations in the field of computer vision. Neural networks became popular in 2012
₁₁₃₄ when Alex Krizhevsky used them to win that year's ImageNet competition [?] by
₁₁₃₅ dropping the error from 26% to 15%. Since then, many companies are using deep
₁₁₃₆ learning including Facebook's tagging algorithms, Google for their photo search and
₁₁₃₇ Amazon for product recommendations. For the purpose of this thesis CNNs were
₁₁₃₈ used for image classification, specifically, images of varying particles created using
₁₁₃₉ LArTPC data.

₁₁₄₀ **6.1 Image Classification**

₁₁₄₁ Image classification is the process of inputting an image into the CNN and receiving a
₁₁₄₂ probability of classes that best describes what is happening in the image. As humans,
₁₁₄₃ image classification is something that is learned at a very young age and is easy to
₁₁₄₄ do without much effort. This is also apparent when hand-scanning LArTPC images.
₁₁₄₅ After learning what a neutrino event looks like in MicroBooNE, it is relatively easy
₁₁₄₆ to recognize simple neutrino events from cosmic ray background as well as highly
₁₁₄₇ ionizing particles like protons from minimum ionizing particles like muons. The very
₁₁₄₈ detailed images LArTPC detectors output are prime candidates for input images into
₁₁₄₉ a CNN. CNNs mimic a human's ability to classify objects by creating an architecture
₁₁₅₀ that can learn differences between all the images it's given as well as figure out the

unique features that make up each object. CNNs are modeled after the visual cortex. Hubel and Wiesel [?] found that there are small regions of neuronal cells in the brain that respond to specific regions of the visual field. They saw that some neurons fired when exposed to vertical edges while others fired when shown horizontal or diagonal edges. They also saw that these neurons were organized in columns. The idea of specific neurons inside of the brain firing to specific characteristics is the basis behind CNNs.

6.2 CNN Structure

When used for image recognition, convolutional neural networks consist of multiple layers that extract different information on small portions of the input image. How many layers is tunable to increase the accuracy. The output of these collections are then tiled so that they overlap to gain a better representation of the original image and allow for translation. The first of these layers is always a convolution layer. To the CNN, an image is an array of pixel values. For a RGB color image with width and height equal to 32x32 the corresponding array is 32x32x3. Filters, also known as neurons, of any size set by the user is then convolved with the receptive field of the image. If the filter is 5x5, the receptive field will be a patch of 5x5 on the input image. The filter is also an array of numbers called weights. The convolution of the filter and image are matrix multiplications of the weights and the pixel values. By stepping the receptive field by 1 unit, for an input image of 32x32x3 and a filter of 5x5x3 you'd get an output array of 28x28x1. This output array is called an activation map or feature map. The use of more filters preserves the spatial dimensions better. The filters can be described as feature identifiers. Examples of features in an image consist of edges, curves, and changes in colors. The first filters in a CNN will primarily be straight line and curve feature identifiers. An example of a curve filter is shown in figure 6.2. When a curve in the same concavity is found in the input image, the corresponding pixel in the output feature map will be activated. Going back to our example of a 32x32 input image and a 5x5 filter, if there were to be a curve in the top left corner of the input image, our output feature map would have a high pixel value in the top left. Therefore, feature maps tell us where a specific feature is located in the original image. Figure ?? shows a visualization of filters found in the first layers of many CNN architectures. These filters in the first layer convolve around the image and activate when the specific feature it is looking for is in the receptive field.

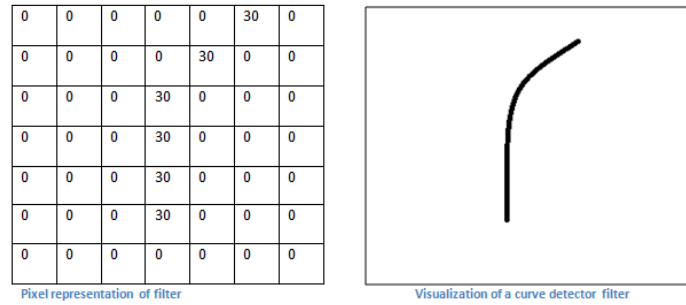


Figure 6.1: Pixel representation and visualization of a curve detector filter. As you can see, in the pixel representation, the weights of this filter are greater along a curve we are trying to find in the input image

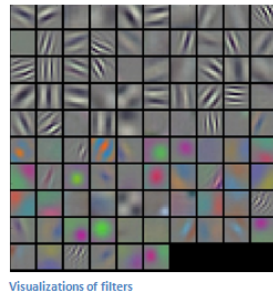


Figure 6.2: Visualization of filters found in first layer of a CNN.

In figure 6.3 you can see how an edge detection filter is used to save only necessary information for recognizing different types of clothes. You can also see by having multiple filters you can get more detail or less detail from an image which can then simplify or complicate the object recognition task. Being able to distinguish between a shirt or a leg garment is as much information you want, having a filter that extracts outline edge or shape information would be all that you need. But if instead you wanted to distinguish between a formal cocktail dress or a summer dress, more information would need to be saved equating to many more filters for one image. Rather than trying to come up with how many filters and what features are important for detection, CNNs do this automatically. CNNs take input parameters, called hyperparameters, for example number of layers, number of filters per layers, number of weights per filter, and uses these to create the output feature maps. The layers build upon each-other, for example if we were creating a CNN for facial recognition the convolutional layers will start learning feature combinations off of the previous layers. The low level features like edges, gradients, and corners of the first layers become high level features like eyes, noses, and hairs. This process is visualized in figure 6.4



Figure 6.3: Applying a feature mask over a set of fashion items to extract necessary information for auto-encoding. Unnecessary information for example color or brand emblems are not saved. This feature map is an edge detection mask that leaves only shape information which helps to distinguish between different types of clothes.

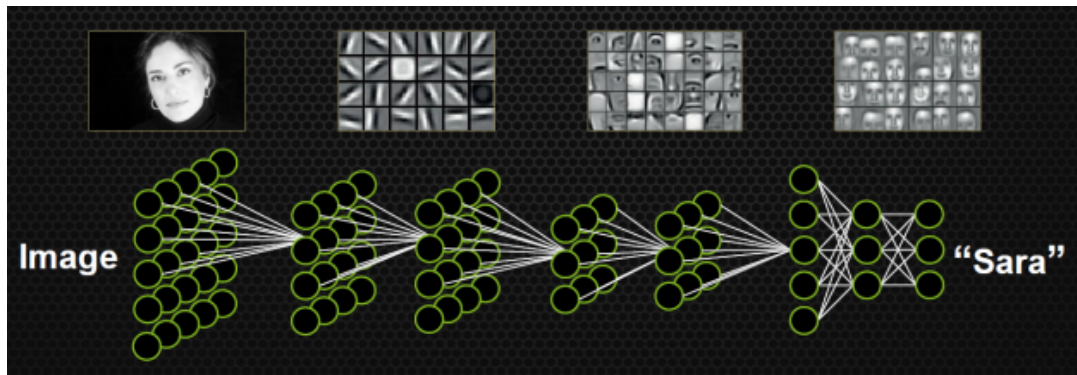


Figure 6.4: Pictorial Representation of Convolutional Neural Networks as well as a visual representation on CNN's complexity of layer feature extraction

1200 There are other layers in a CNN architecture that will not be covered in the scope
 1201 of this thesis but in a general sense, these layers are interspersed between convolution
 1202 layers to preserve dimensionality and control overfitting of the network. The last layer
 1203 is called a fully connected layer and it's job is to output an N dimensional vector where
 1204 N is the number of classes the network has been trained on. Each number in this vector
 1205 represents the probability that the input image is a certain class. Fully connected layers
 1206 use the feature maps of the high level features to compute the products between the
 1207 weights of the previous layer to get the probabilities of each class. These weights are
 1208 then adjusted through the training process using backpropagation.

1209 6.2.1 Backpropagation

1210 A CNN at it's onset has weights that are randomized. The filters themselves don't
 1211 know how to pull out identifying information per class. For a neural network to learn,
 1212 it must be trained on a training set that is labeled. Backpropagation has four seperate
 1213 steps: foward pass, loss function, backward pass and updating weights. In the forward
 1214 pass, a training image is passed through the whole network. All of our weights at this
 1215 time are randomly initialized so the output for the first image will have no preference
 1216 to a specific class. A common loss function is mean squared error (MSE):

$$E_{total} = \sum \frac{1}{2} (actualclass - predictedclass)^2 \quad (6.1)$$

1217 If we assume that the MSE is the loss of our CNN, the goal would be that our
 1218 predicted label (output of CNN) is the same as our training label. To do this, we need
 1219 to minimize the loss function. To do this, it is necessary to find out which weights most
 1220 directly affect the loss of the network i.e $\frac{dL}{dW}$ where L is our loss function and W are
 1221 the weights of a specific layer. The next step is the backward pass which determines
 1222 which weights contribute the most to the loss and finds ways to adjust these weights
 1223 so that the loss decreases. After the derivative is computed, the last step updates the
 1224 weights in the opposite direction of the gradient.

$$w = w_i - \eta \frac{dL}{dW} \quad (6.2)$$

$$w = \text{Weight} \quad (6.3)$$

$$w_i = \text{Initial Weight} \quad (6.4)$$

$$\eta = \text{Learning Rate} \quad (6.5)$$

1225 The learning rate is a parameter given to the CNN and it describes the steps the
 1226 network takes to update the weights. Higher learning rate equals large steps and a
 1227 lower training time, but a learning rate that is too large can mean the CNN never
 1228 converges.

1229 Going through backpropagation consists of one training iteration. Once the net-
 1230 work completes a specific number of iterations, another parameter given, and runs
 1231 over all training images that are split up into batches, the process is considered com-
 1232 plete. User input parameters, called hyperparameters, help the network converge to

optimal weights for each layer. Batch size, learning rate, and training iteration are just some of the user input hyperparameters that help. Lastly, to check if the network has learned, a different set of labeled images are fed to the CNN iteratively through the training process to see how well it's learning. This process is especially important to make sure the network architecture isn't being affected by overfitting (memorizing training input rather than learning).

6.3 Choosing Hyperparameters

Convolutional neural networks are a relatively new tool in computer vision. Choosing hyperparameters for your specific dataset is a non-trivial task. Hyperparameters can range from the amount of layers and filters per layer in an CNN architecture to the stride the receptive field of a filter takes, not to mention training hyperparameters such as learning rate and batch size described above. They're ways to optimize these hyperparameters via hyperparameter optimization using Bayesian Optimization [?] but as you can imagine, optimizing an CNN architecture from scratch can be very computationally intensive. For the purpose of this thesis, two well known CNN architectures were used, AlexNet [?], which won the ImageNet Large-Scale Visual Recognition Challenge (ILSVRC) in 2012 and therefore bringing awareness of CNNs, and GoogleNet [?], which won the ILSVRC in 2014, giving rise to deep networks. Both AlexNet and GoogleNet architectures were used to train on LArTPC images and their low level filter weights. Higher level filter weights were randomly initialized before training so the network can learn high level features of LArTPC image classes. The AlexNet architecture is shown in figure 6.5 and the GoogleNet architecture is shown in figure 6.6

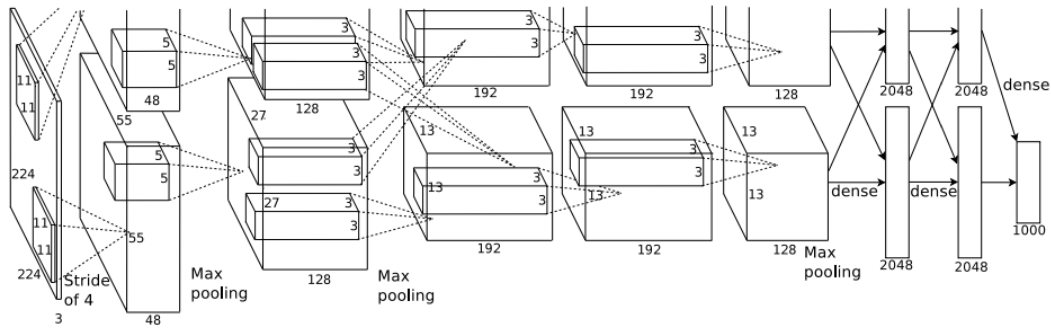


Figure 6.5: Pictoral representation of the AlexNet model. The AlexNet model consists of 5 convolution layers and 3 fully connected layers.

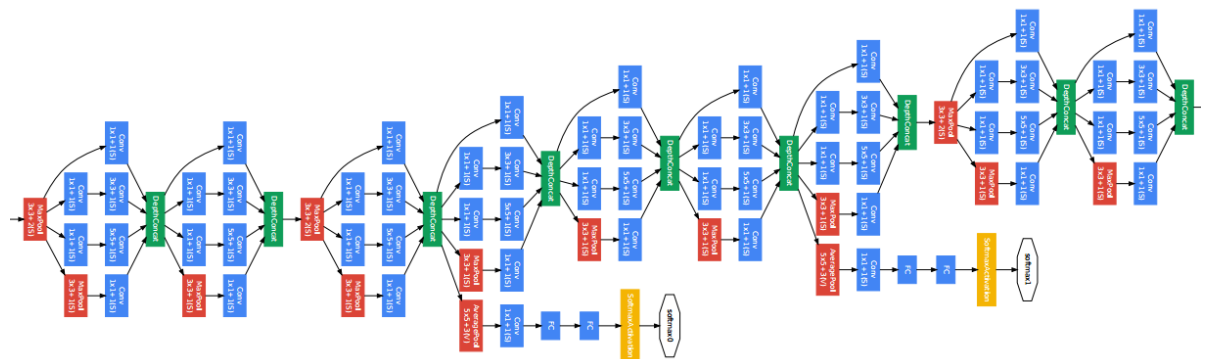


Figure 6.6: Pictoral representation of the GoogleNet model. The GoogleNet model consists of 22 layers. The model implements 9 Inception modules which performs covolution and pooling in parallel and strays away from the basis that CNN layers need to be stacked up sequentially. The GoogleNet model also doesn't use fully connected layers, instead it uses average pooling which greatly reduces the amount of parameters. GoogleNet has 12x fewer parameters than AlexNet.

1256 Chapter 7

1257 Training Convolutional Neural 1258 Networks on particles **WORKING** 1259 **TITLE**

1260 Three Convolutional Neural Networks CNNs were trained throughout this analysis.
1261 There are differences to each CNN and will be described fully in the next sections but
1262 the main difference are the amount of particle images used for training and validation.
1263 CNN1075 used 1,075 muons and 10,75 pions for training and the same amount of each
1264 particle for validation. CNN10000 used 10,000 muons and 10,000 pions split in half
1265 for testing and training. Lastly CNN100000 had muons, pions, protons, electrons,
1266 and gammas in its training and validation set. Each particle had 20,000 images and
1267 training and validation was split 90% training, 10% validation. This chapter will also
1268 describe the different hardware frameworks used for training beginning on a CPU
1269 and ending on a GPU cluster.

₁₂₇₀ **7.1 Hardware Frameworks used for Training**

₁₂₇₁ **7.1.1 Syracuse CPU Machine setup**

₁₂₇₂ **7.1.2 Syracuse University GPU Cluster Setup**

₁₂₇₃ **7.2 Convolutional Neural Network Training**

₁₂₇₄ **7.2.1 Image Making Scheme**

₁₂₇₅ **Images used for Traing/Validation of Convolutional Neural Networks**

₁₂₇₆ **add image making for CNN1075** The μ/π image dataset used to train and validate
₁₂₇₇ the CNN10000 was created using single generated isotropic muons and pions from
₁₂₇₈ 0-2 GeV energ range. 10,000 muons and 10,000 pions were used for training and
₁₂₇₉ testing split 50%. The images were created based on wire number and time tick in the
₁₂₈₀ collection plane. Uboonecode v06_23_00 was used instead of v05_08_00 which was
₁₂₈₁ used previously. The wire signal was the raw ADC value after noise filtering. Each
₁₂₈₂ collection plane grayscale image was 3456x1280x1 where 5 time ticks were pooled into
₁₂₈₃ 1 bin which is different than the previous dataset and was implemented due to the fact
₁₂₈₄ that the time ticks of an event went from 9400 to 6400 with the change of uboonecode
₁₂₈₅ version. The grayscale color standard is 8bit therefore the ADC value of wire and time
₁₂₈₆ tick was also downsampled due to the 12bit ADC value MicroBooNE has. To do this,
₁₂₈₇ the highest ADC pixel in the image was found and then this was divided by the rest
₁₂₈₈ placing all pixel values between 0-1. From there, all pixel values are then multiplied
₁₂₈₉ by 255. All images were made using a LArSoft module. Once the images were created,
₁₂₉₀ using and image manipulation framework called OpenCV images were read into a
₁₂₉₁ numpy array and cropped to the region of interest by only keeping rows and columns
₁₂₉₂ where all ADC values are higher than 0 and then resized it to 224x224 using OpenCV's
₁₂₉₃ resize function. This downsampling of ADC values creates a problem of information
₁₂₉₄ loss for example, a proton which is highly ionizing will have the same brightness as a
₁₂₉₅ minimum ionizing muon by virtue of how the images are created. Issues that arose
₁₂₉₆ in CNN1075 that were fixed in CNN10000 include zero-padding images in X and Y
₁₂₉₇ that are smaller than 224X224 to eliminate over-zooming effect and fixing a bug that
₁₂₉₈ shifted pixels separated by a dead-wire region.

1299 Images were also made from events that passed the cc-inclusive selection 1 filter
1300 right before the 75 cm track length cut and were classified using the CNN10000. The
1301 dataset used to create these images is the same one used in [?], prodgenie_bnb_nu_cosmic_uboone_mc
1302 These images were created using information from the track candidate that passed
1303 the filter. Only wire number and time ticks associated to the track candidate were
1304 drawn on the image to mimic a single particle generated image. These images were
1305 then classified using CNN10000. Two approaches were taken in making these images.
1306 The first was using the image normalization above where the maximum pixel in each
1307 image is used as a normalization constant to get all pixels between 0-1 then multiply
1308 all pixels by 255. As described above, this is the incorrect way to normalize; it should
1309 be normalized by dataset not by event, which is the second way the images were
1310 created. The results of CNN10000 performance are shown in section 7.2.

1311 7.2.2 Training CNN1075

1312 The work shown in these next sections are based on the previous work done described
1313 in [?]. That CNN (now referred to as CNN1075) was trained using single generated
1314 isotropic muons and pions from 0-2 GeV energy range. 1,075 muons and pions were
1315 used to train the network and 1,075 μ/π were used as a validation set. The accuracy is
1316 how well CNN1075 is doing by epoch and was 74.5%. The loss is gradient descent
1317 or minimization of the error of the weights and biases used in each neuron of each
1318 layer of CNN1075 and was 58% with a trend sloping downwards on the loss curve
1319 as well as a trend sloping upward in the accuracy curve. Due to the depth of the
1320 neural network framework, it was necessary to train with a larger dataset and for
1321 more epochs, however, the downward slope of the loss curve is an indication that once
1322 trained for longer with a higher training sample, neural networks can be used for μ/π
1323 separation. Updates in the image making and downsampling algorithm were made to
1324 fix issues that arose in CNN1075.

1325 7.2.3 Training CNN10000

1326 The hyperparameters used for CNN10000 are shown. The batch size for the training
1327 and testing as well as the test iter were chosen to encompass the whole training/testing
1328 image set when doing accuracy/loss calculations. To do this, multiplying the test

1329 iter by the test batch size give you the amount of images used when calculating
1330 accuracy/loss curves. For reference, the accuracy and loss are defined as well.

```
1331     • train_batch_size: 100
1332     • test_batch_size: 100
1333     • test_iter: 100
1334     • test_interval: 100
1335     • base_lr: 0.001
1336     • lr_policy: "step"
1337     • gamma: 0.1
1338     • stepsize: 1000
1339     • display: 100
1340     • max_iter: 10000
1341     • momentum: 0.99
1342     • weight_decay: 0.0005
1343     • snapshot: 100
1344     • Accuracy: How often the CNN predicts the truth over total number of images
1345     • Loss: Error between truth and prediction. Minimize loss by gradient descent to
1346       update weights and biases of CNN
```

1347 The same architecure that was used to train CNN1075 was employed on CNN10000,
1348 Imagenet. Caffe [?] was the software package used for both CNNs. The differences
1349 include batch size and test_iter and momentum to account for the larger dataset. Both
1350 CNNs were trained on a CPU machine, Syracuse01. Further training will be done
1351 on a GPU cluster stationed at Syracuse University. Figure 7.1 shows the loss and
1352 accuracy of CNN10000. There is around a 10% increase in accuracy from CNN1075 to
1353 CNN10000, 85%, and around a 20% decrease in loss, 36%.

1354 Figure 7.2 show a breakdown of μ/π separation for CNN10000. It also shows
1355 the network is not being overtrained due to the Accuracy of both the training and
1356 testing datasets being within .01% of eachother. The CNN is doing a very good job of

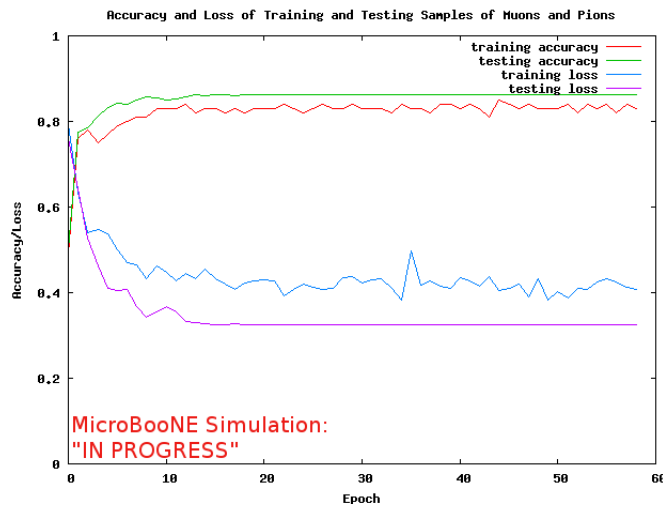
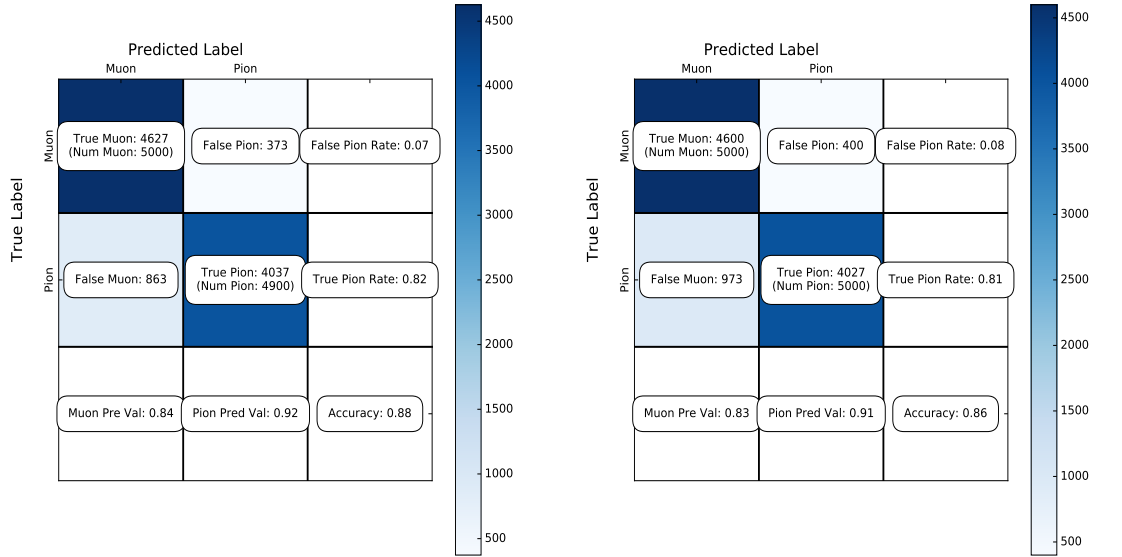


Figure 7.1: Accuracy vs. Loss of ImageNet 2-output μ/π sample consisting of 10000 images each.

1357 classifying true muons as muons, and our loss increase from CNN1075 is due to the
1358 increase in accurately classifying pions as pions.

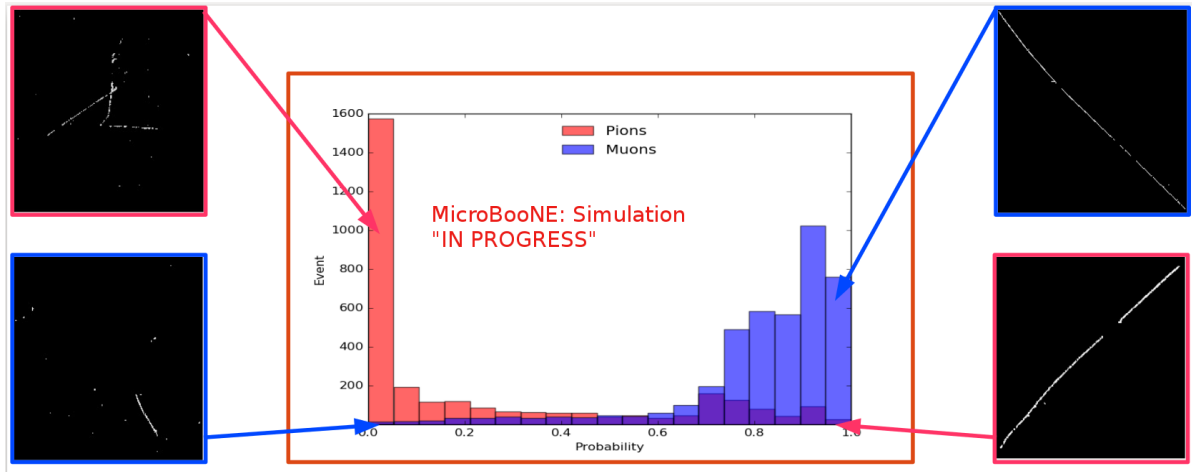
1359 7.2.4 Training CNN100000

1360 Results of training using 100,000 images, 20,000 images per $\mu/\pi/p/\gamma/e$.



(a) Confusion Matrix showing Accuracy of CNN using training data

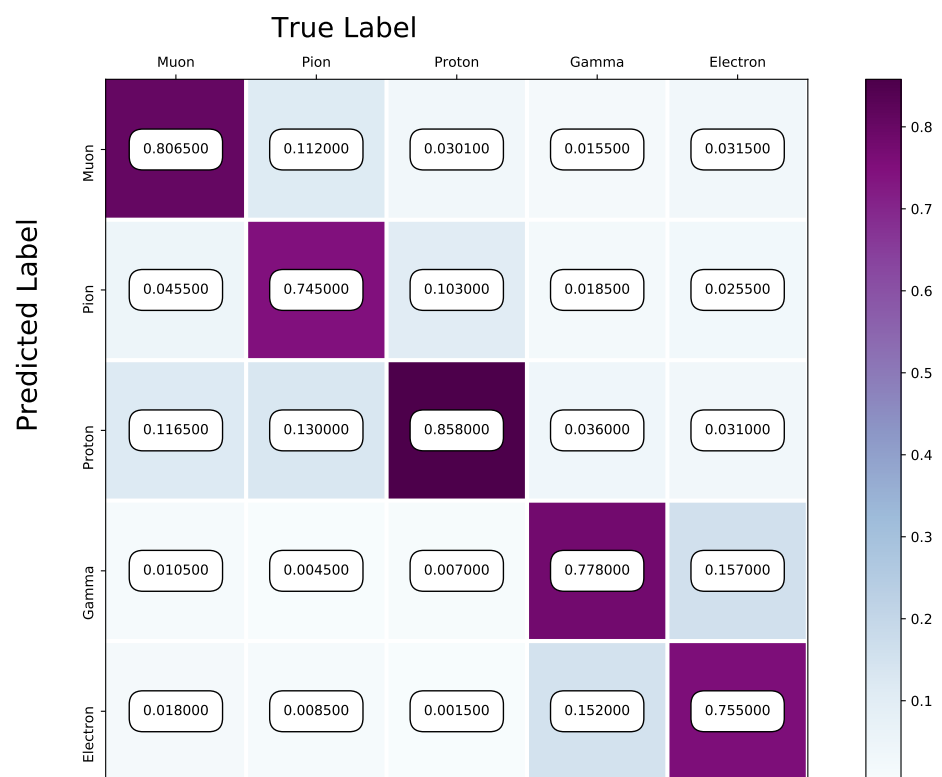
(b) Confusion Matrix showing Accuracy of CNN using testing data



(c) Probability plot of muons and pions from testing set. Images surrounding histogram are a random event from lowest bin and highest bin for each particle.

Figure 7.2: Description of confusion matrix variables: False pion rate = $false\pi / total\pi$ True pion rate = $true\pi / total\pi$ Accuracy = $(true\pi rate + true\mu rate) / 2$ Pion prediction value = $true\pi / (true\pi + false\pi)$ Muon prediction value = $true\mu / (true\mu + false\mu)$

7.2c The probability plot includes muons and pions that are classified as primary particles.

**Figure 7.3:** Confusion Matrix of all five particles

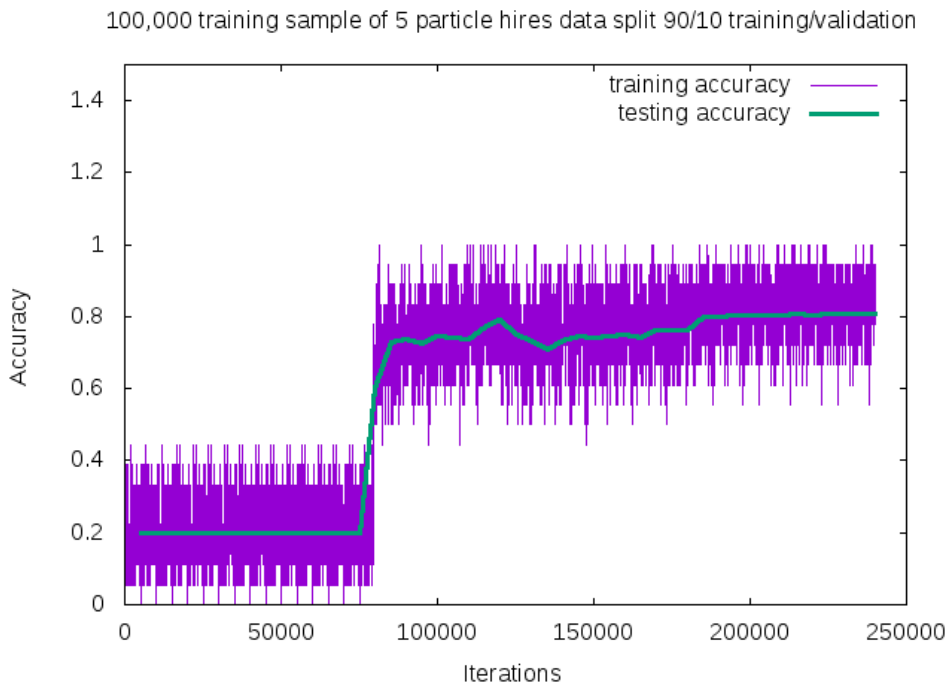


Figure 7.4: Training and testing accuracy of CNN trained on 100,000 images of $\mu/\pi/p/\gamma/e$ with 20,000 images of each particle. Each image was a size of 576x576 and the images per particle were split 90% use for training and 10% used for testing the network

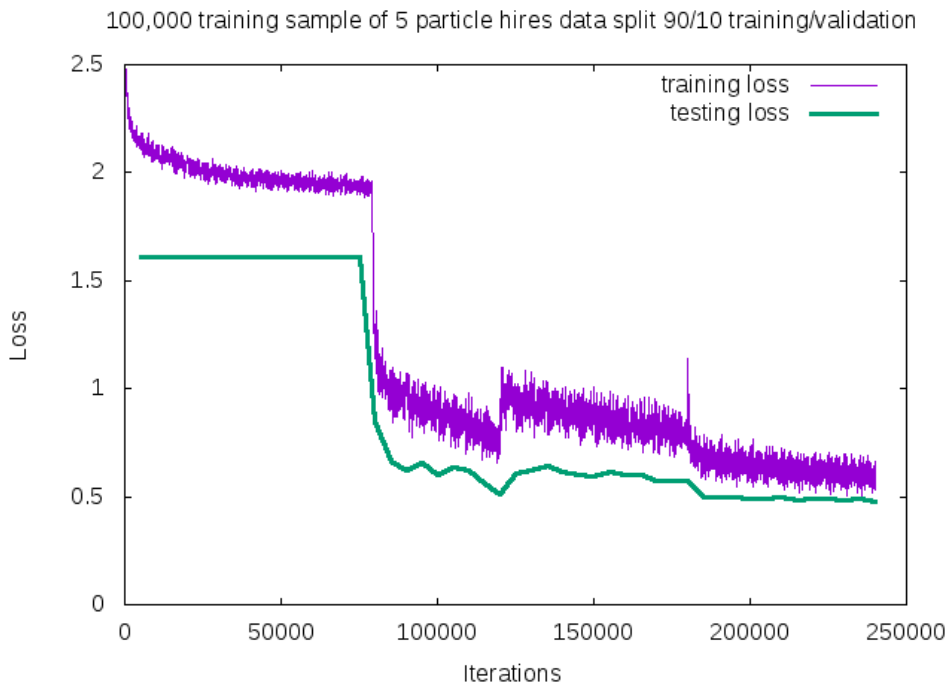


Figure 7.5: Training and testing loss of CNN trained on 100,000 images of $\mu/\pi/p/\gamma/e$

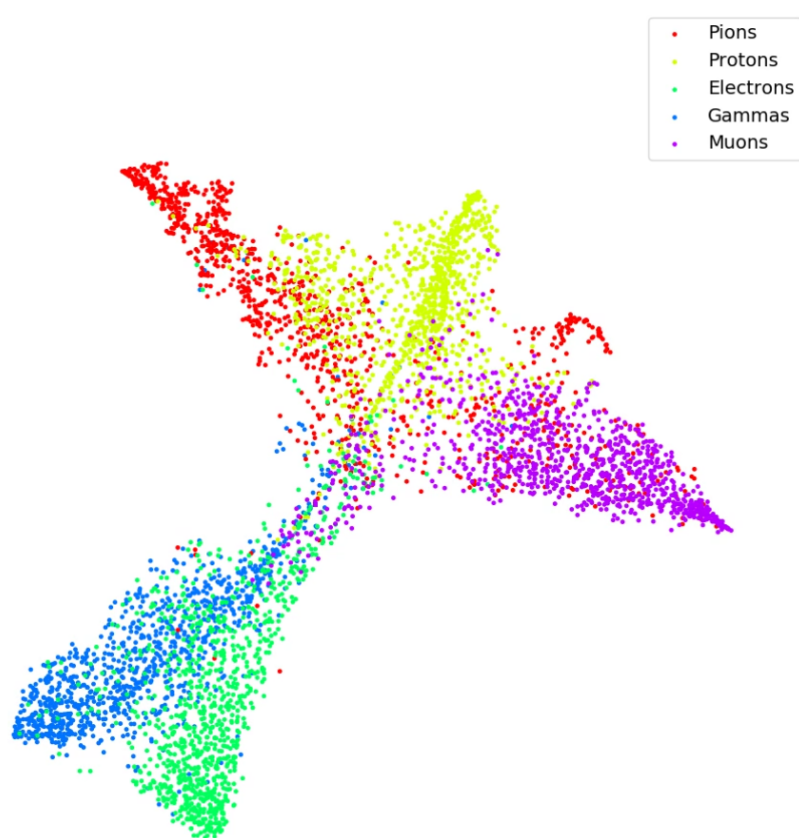


Figure 7.6: t-SNE of CNN

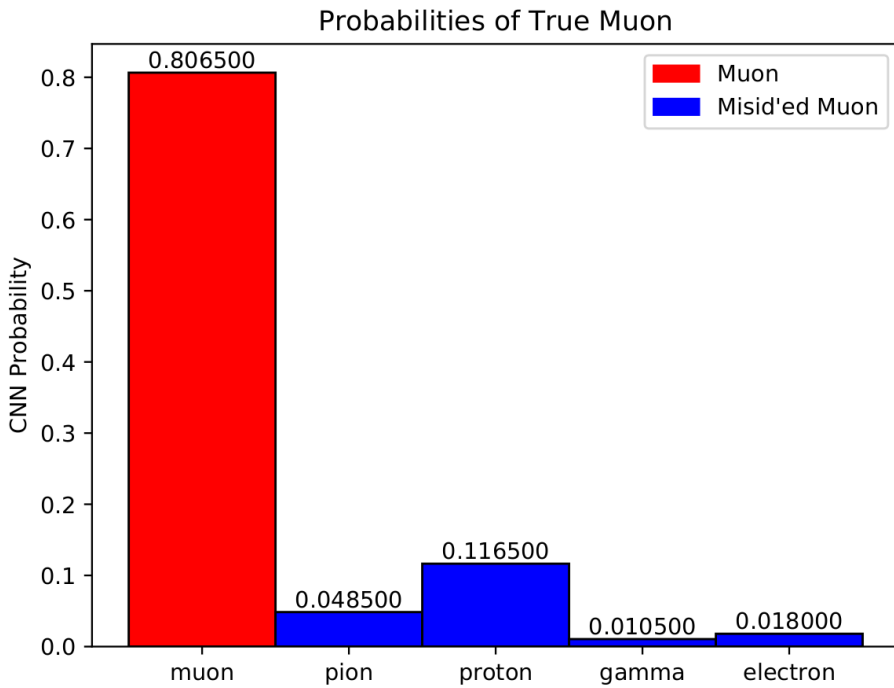


Figure 7.7: Muon Prob

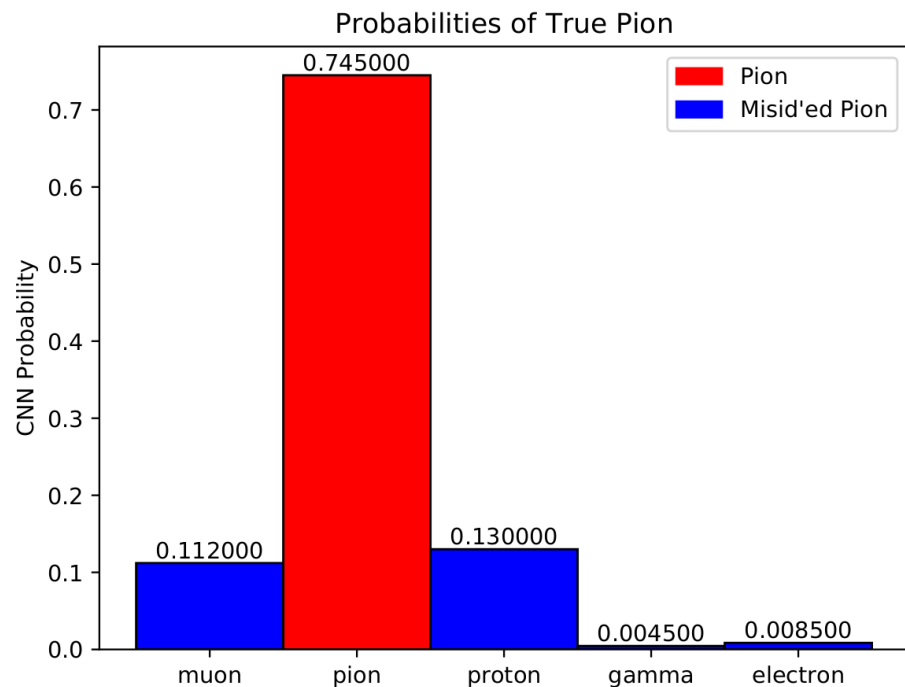


Figure 7.8: Pion Prob

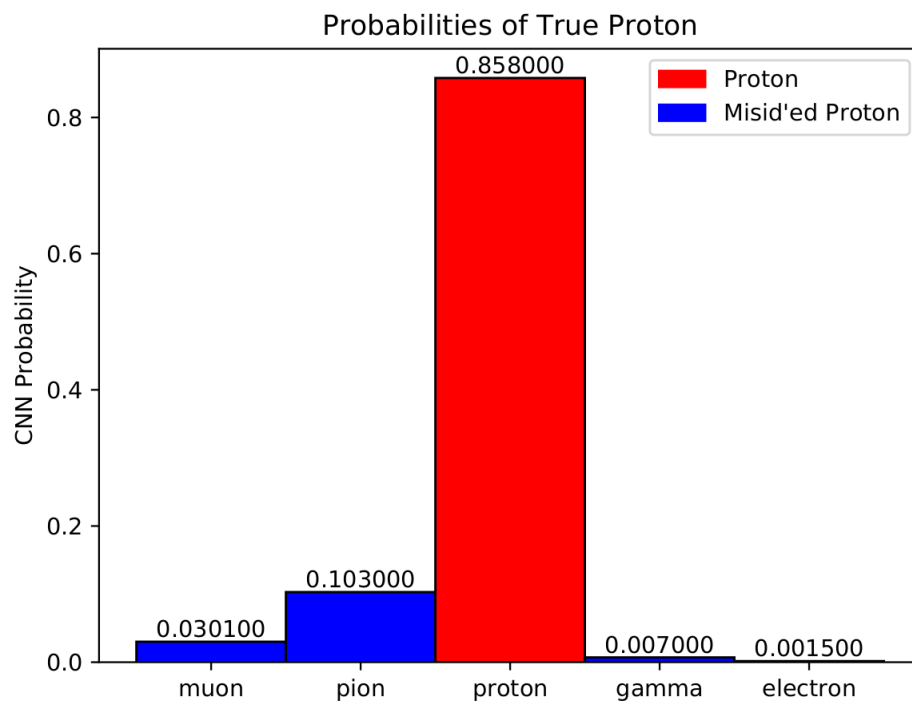


Figure 7.9: Proton Prob

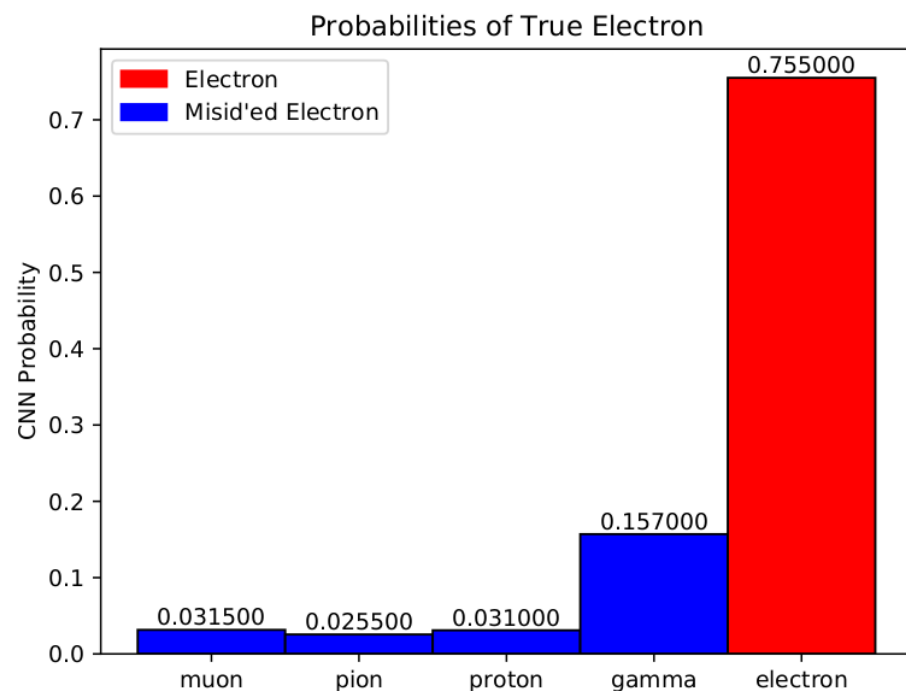


Figure 7.10: Electron Prob

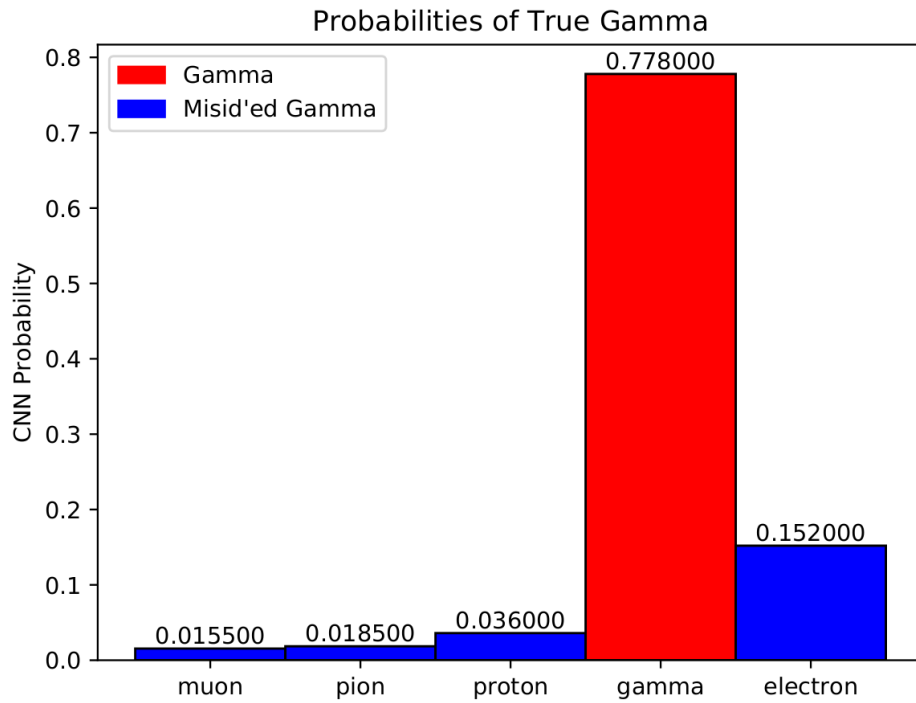


Figure 7.11: Gamma Prob

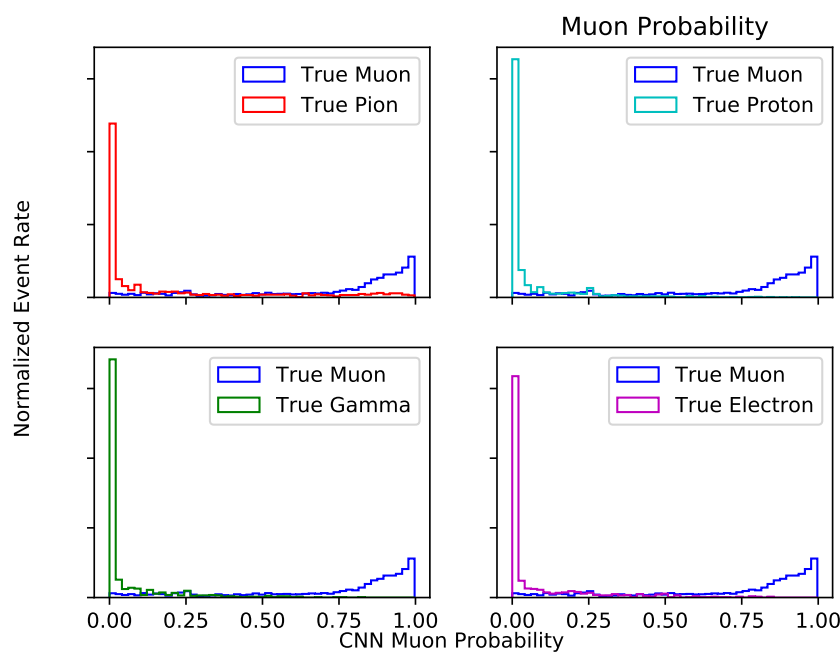


Figure 7.12: Prob

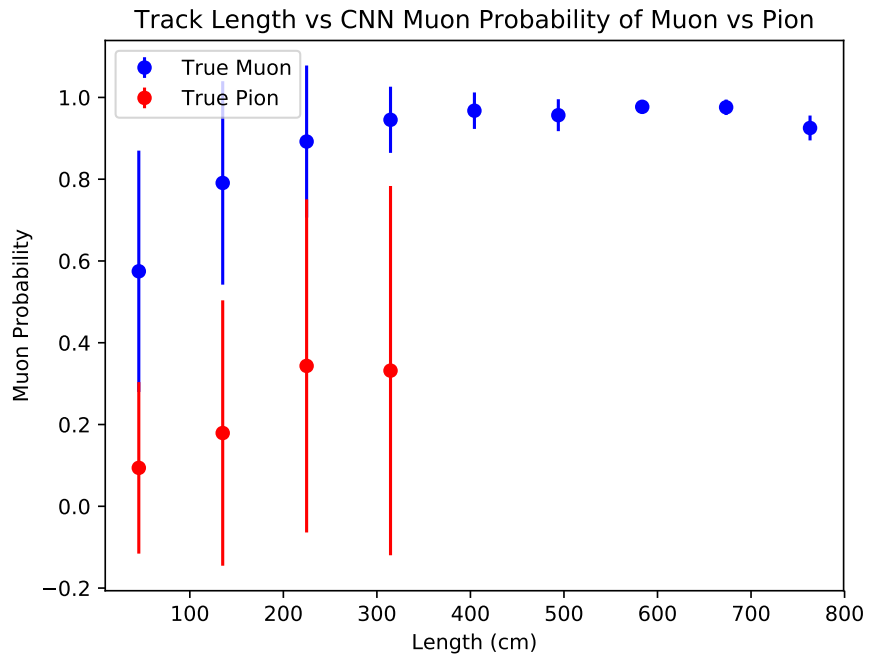


Figure 7.13: mupi

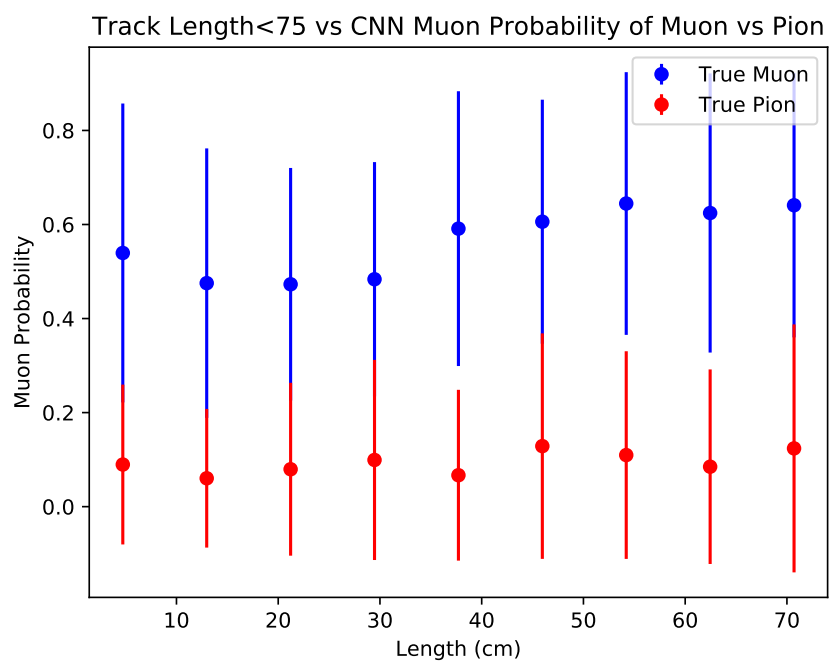
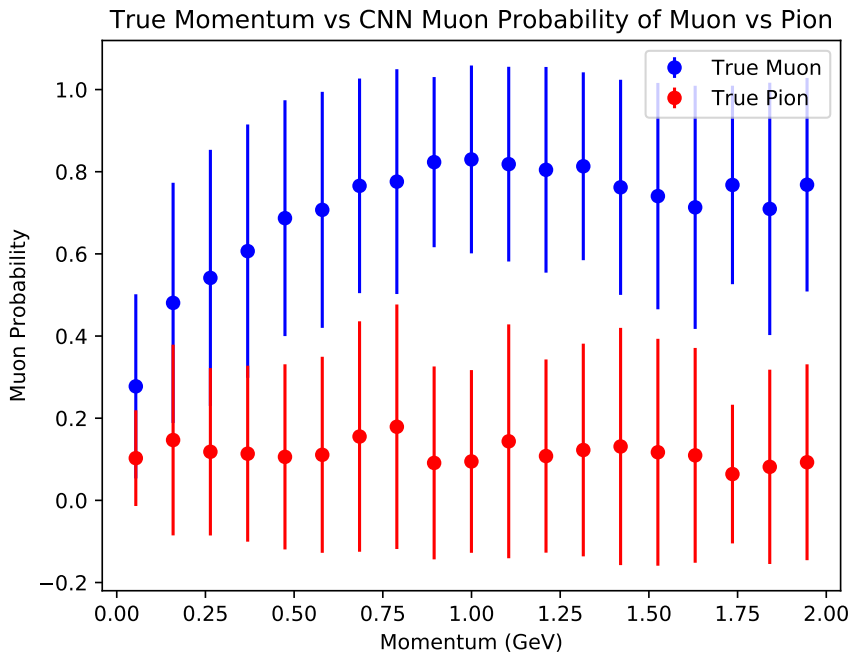
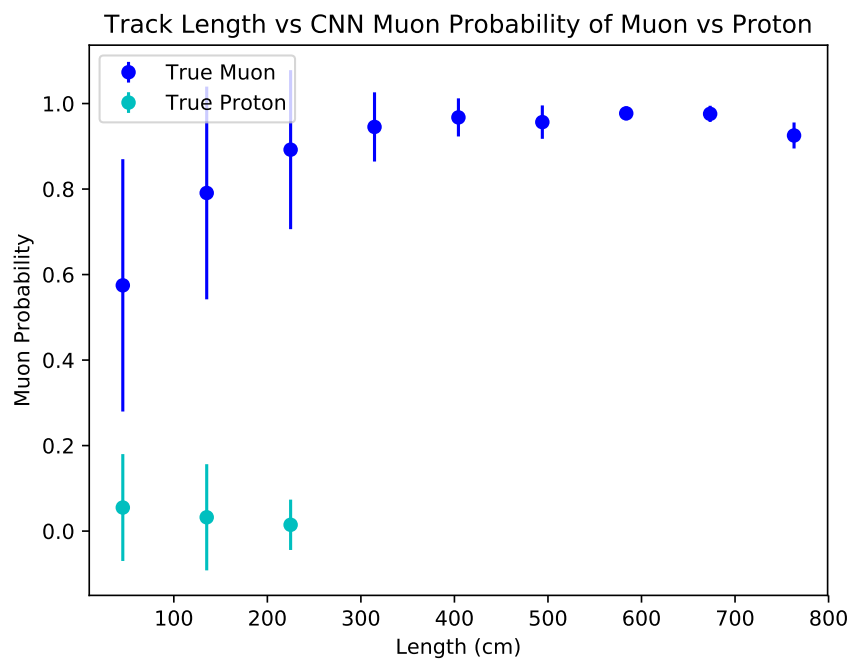
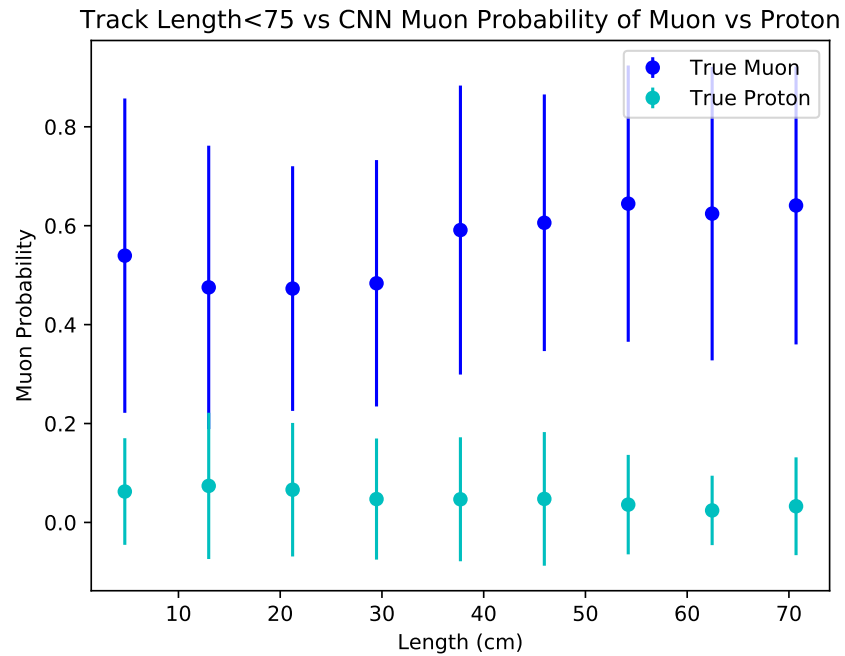
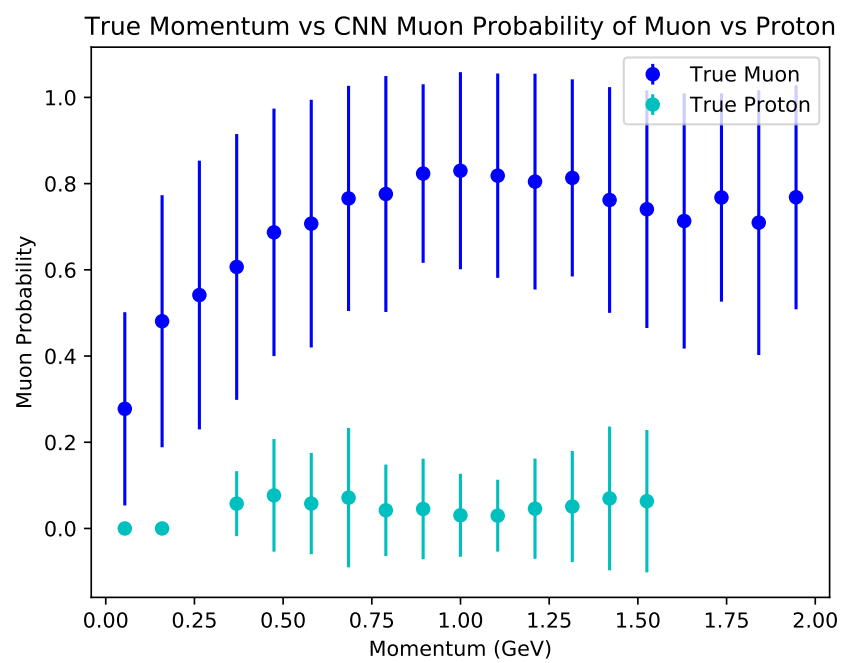


Figure 7.14: mupi

**Figure 7.15:** mupi**Figure 7.16:** mup

**Figure 7.17:** mup**Figure 7.18:** mup

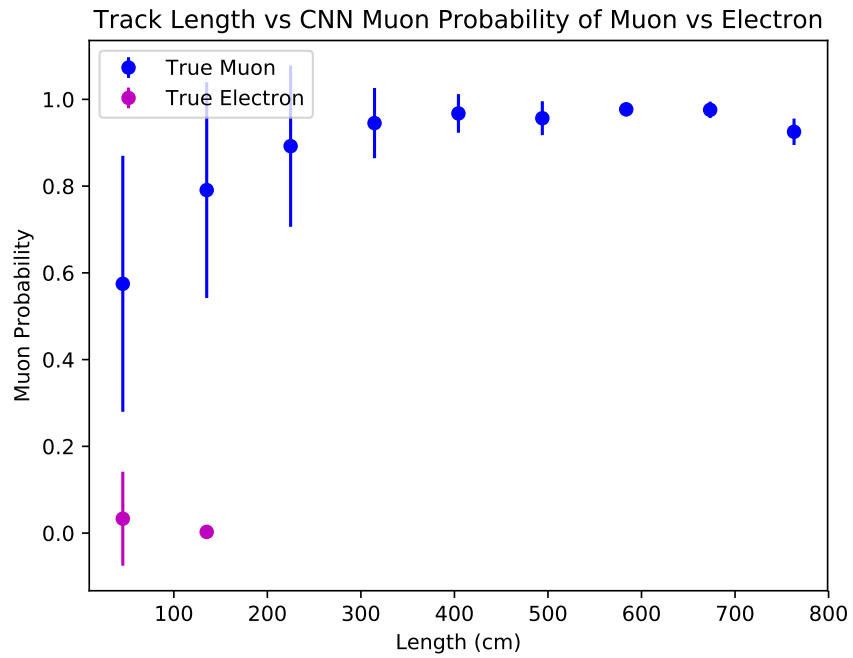


Figure 7.19: mue

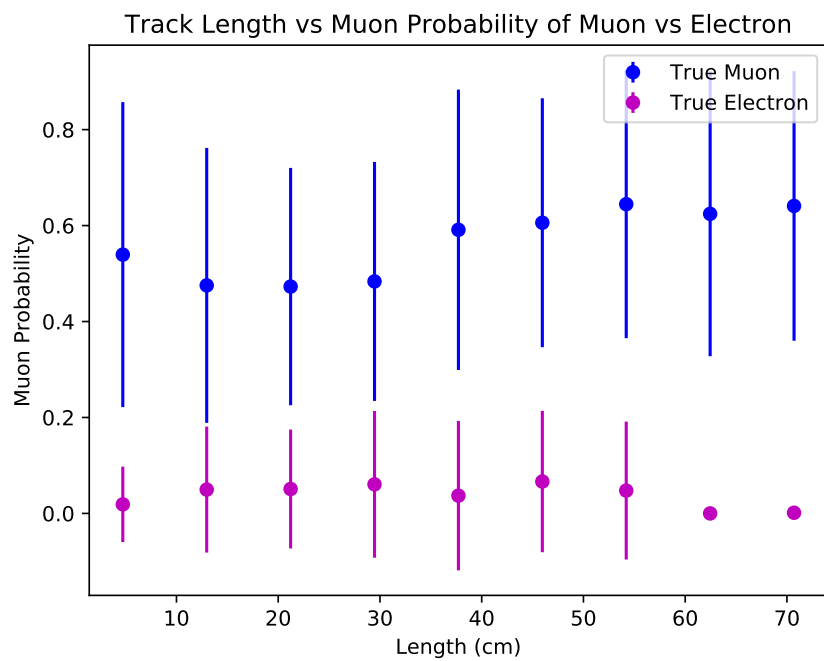


Figure 7.20: mue

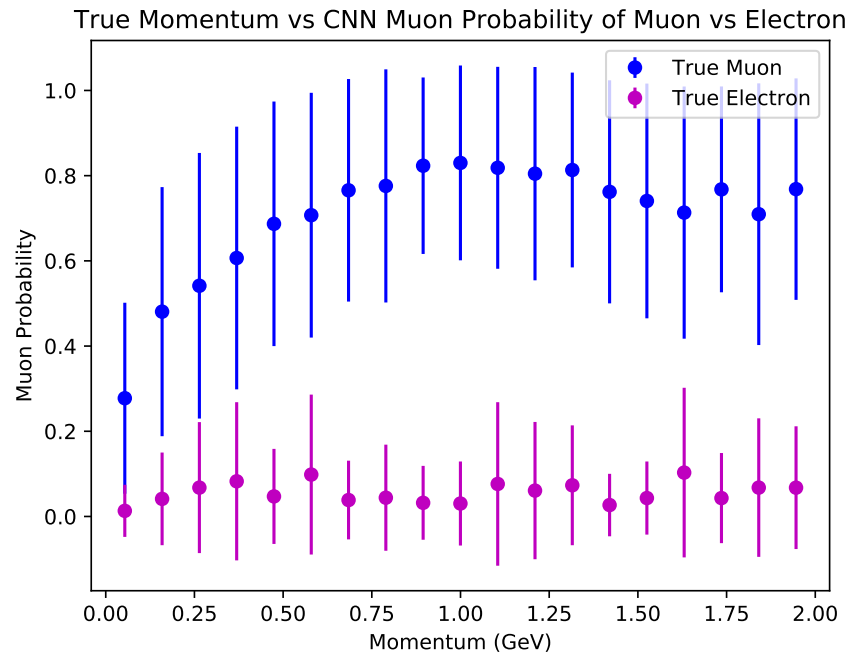


Figure 7.21: mue

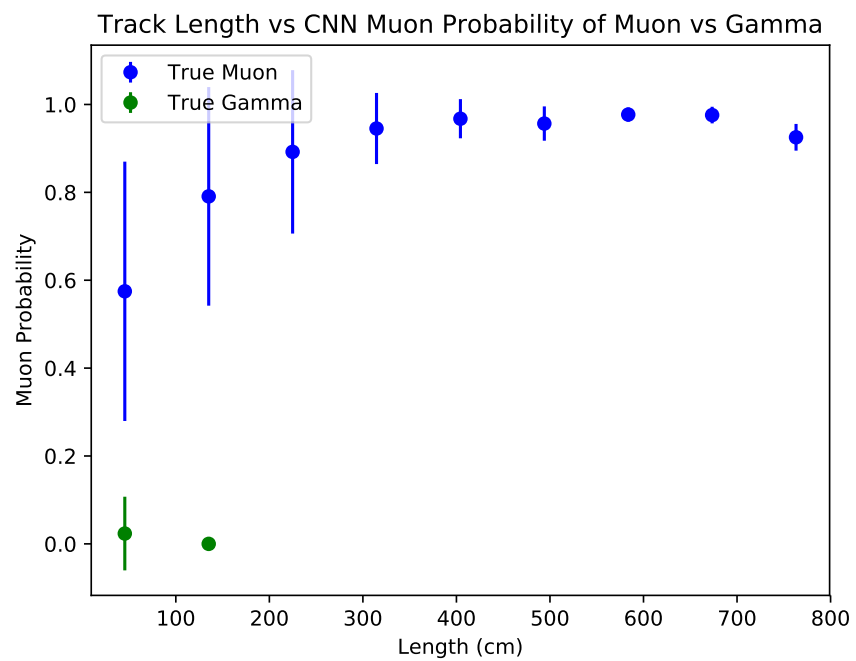


Figure 7.22: mug

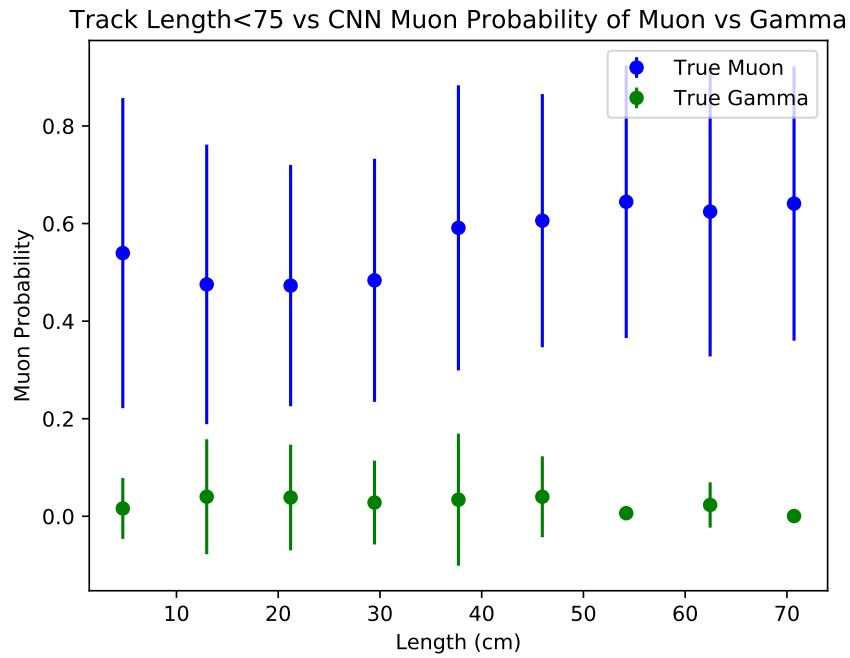


Figure 7.23: mug

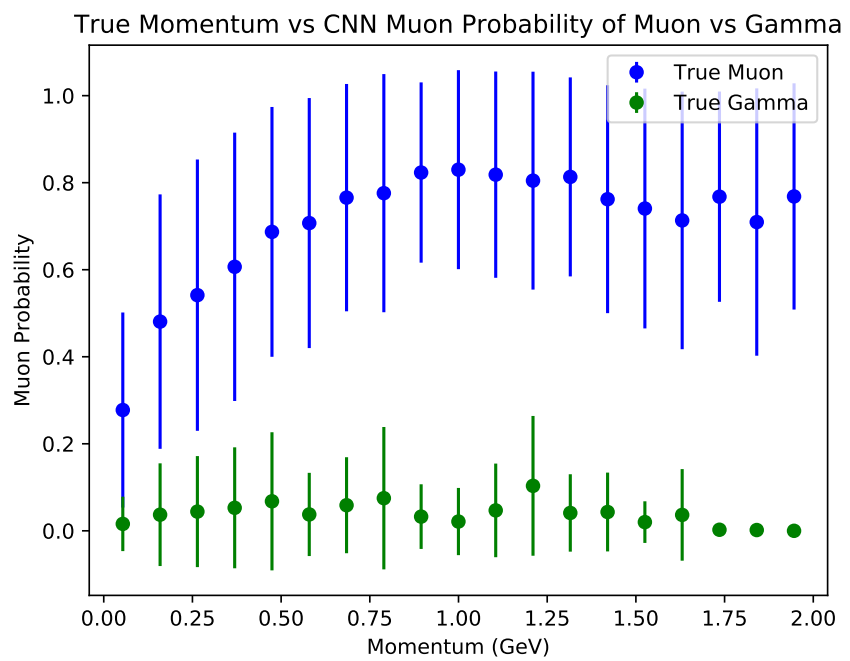


Figure 7.24: mug

1361 Chapter 8

1362 Results of Convolutional Neural 1363 Networks on particles **WORKING** 1364 **TITLE**

1365 8.1 Classification using CNN10000

1366 8.1.1 Classification of MC data using Selection I Original 1367 CC-Inclusive Filter

1368 The next step that was taken was to use CNN10000 to classify track candidate images
1369 that were identified by the selection I original cc-inclusive filter described in [?].
1370 Passing rates for each cut in cc-inclusive filter are show in figure 8.1. For the incorrect
1371 image making normalization dataset, out of 188,880 events, 7438 passed the cut right
1372 before 75 cm track length cut which is 3.9% of total data. Discrepancies in passing rates
1373 are due to grid submission issues, however, this dataset is used to check if changes
1374 in image making normalization affects μ/π separation probability due to CNN10000
1375 being trained with incorrectly image making normalized data. For the second dataset
1376 with correct image making normalization, out of 188,880 events, 9552 events passed the
1377 cut right before the 75 cm track length cut which is 5.1% passing rate and is comparable
1378 to figure 8.1. In time cosmics were also run over for efficiency and purity calculations.
1379 Out of 14395 in time cosmic events, 175 passed the cut right before the 75 cm track
1380 length cut which is a passing rate of 1.2% compared to 1.3% shown in figure 8.1.

Table 3: **Selection I: Original** The table shows passing rates for the above described event selection. Numbers are absolute event counts and Cosmic background is not scaled appropriately. The BNB+Cosmic sample contains all events, not just ν_μ CC inclusive. The selected events are further broken up in the following subsection. The numbers in brackets give the passing rate wrt the step before (first percentage) and wrt the generated events (second percentage). In the BNB+Cosmic MC Truth column shows how many true ν_μ CC inclusive events (in FV) are left in the sample. This number includes possible mis-identifications where a cosmic track is picked by the selection instead of the neutrino interaction in the same event. The cosmic only sample has low statistics, but please note that it is not used in any plots, it is just for illustrating the cut efficiency. The last column Signal:Cosmic only gives an estimate of the ν_μ CC events wrt the cosmic only background at each step. For this number, the cosmic background has been scaled as described in chapter 2. Note that this numbers is not a purity, since other backgrounds can't be determined at this step.

	BNB + Cosmic Selection	MC-Truth	Cosmic only	Signal: Cosmic only
Generated events	191362	45273	4804	1:22
≥ 1 flash with ≥ 50 PE	136219 (71%/71%)	44002 (97%/97%)	2979 (62%/62%)	1:14
≥ 1 vertex in FV	131170 (96%/69%)	43794 (99%/97%)	2805 (94%/58%)	1:13
≥ 1 track within 5 cm of vertex	129784 (99%/68%)	43689 (99%/97%)	2756 (98%/58%)	1:13
flash matching of longest track	44775 (34%/23%)	23647 (54%/52%)	647 (23%/13%)	1:5.7
track containment	10114 (23%/5.3%)	6882 (29%/15%)	61 (9.4%/1.3%)	1:1.9
track ≥ 75 cm	7358 (73%/3.8%)	5801 (84%/13%)	31 (51%/0.6%)	1:1.1

Figure 8.1: Snapshot of passing rates of Selection I from CC-Inclusive Filter

1381 Figures 8.2a, 8.2b, 8.2c and 8.2d show the accuracy and μ/π separation of both the
 1382 correct and incorrect normalized images. The confusion matrices are only composed
 1383 of μ/π data. Other particles passed the cc-inclusive filter before the 75 cm track length
 1384 cut and were all mis-id'ed as muons. Since CNN10000 has not seen any particles
 1385 other than muons and pions, it makes sense that those get mis-id'ed. Figures 8.2b
 1386 and 8.2d don't have μ/π separation comparable to 7.2c, but 8.2b does skew to higher
 1387 probabilities compared to 8.2d. This is to be expected and further work on quantifying
 1388 the performance of CNN10000 should use the incorrect image making normalization. It
 1389 is also expected that the separation isn't as defined as the testing dataset for CNN10000.
 1390 CNN10000 was trained and tested using single particle muons and pions and the track
 1391 candidate dataset come from BNB+Cosmic events, not to mentions all track candidates
 1392 have passed the cc-inclusive filter that tags "muon-like" tracks therefore the pions
 1393 in this sample look much closer in muon topology than the network has seen. Also,
 1394 these images were made from wire and time ticks associated to hits from the track
 1395 candidate that passed the cc-inclusive filter. This is different from the training images
 1396 where a bounding box was drawn over the total μ or π interaction. Spurious energy
 1397 deposition from a $\pi - Ar$ interaction is most likely not included in the BNB+Cosmic
 1398 images due to the tracking algorithm. To remedy this, the neural network needs to
 1399 see more "muon-like" pions and muons and pions from a neutrino interaction passing
 1400 the cc-inclusive filter as well as a larger particle variety including protons, photons

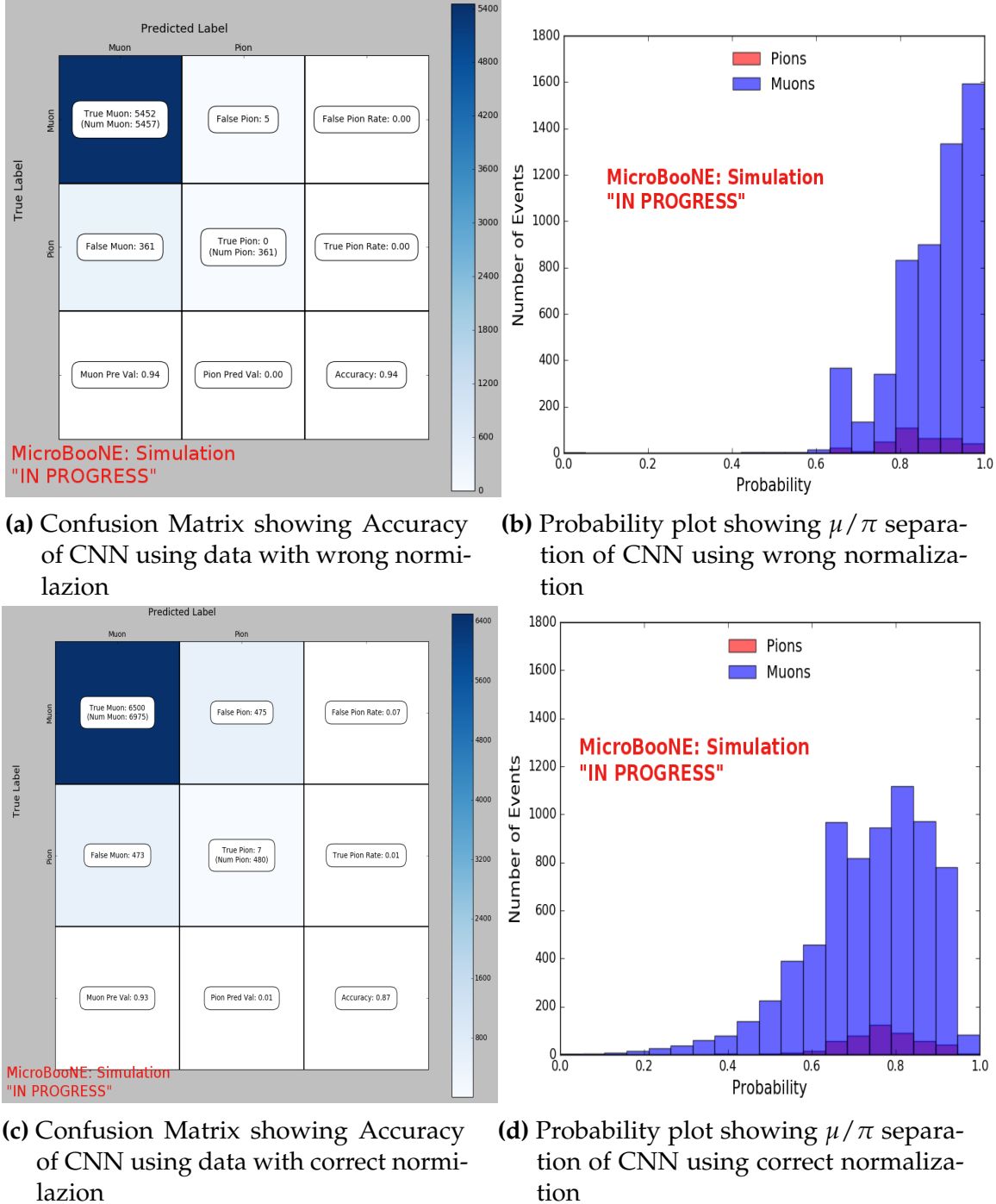


Figure 8.2: Results of CNN10000 classification of track candidate images output from cc-inclusive filter.

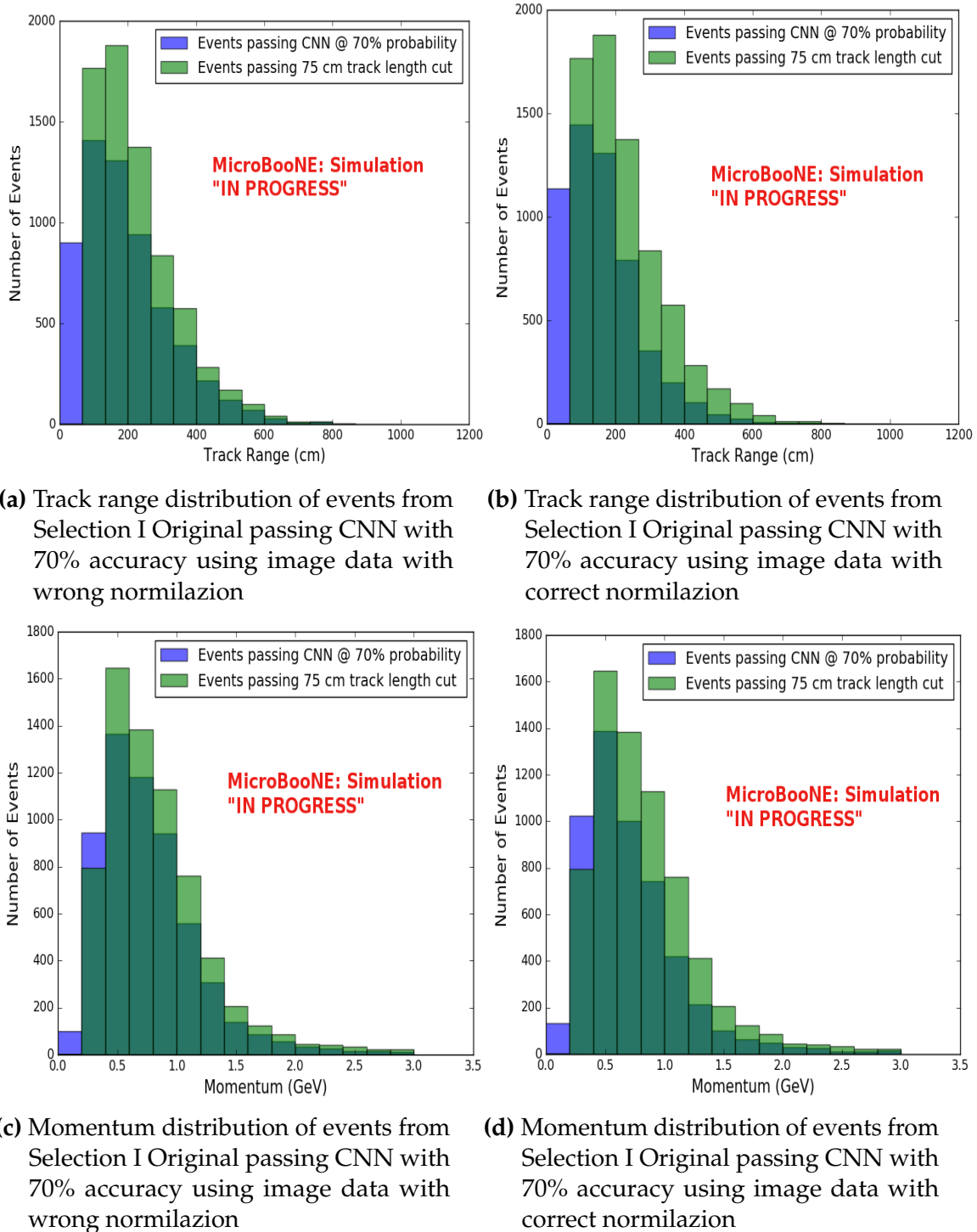


Figure 8.3: CNN10000 distributions of track candidate images output from Selection I Original cc-inclusive filter with different image data normalizations

¹⁴⁰¹ and electrons. Although μ/π separation is lacking, CNN10000 does an excellent job of
¹⁴⁰² classifying muons and using higher CNN probability can increase purity. Figures 8.3a,
¹⁴⁰³ 8.3b, 8.3c and 8.3d show the track and momentum distributions for these two datasets.
¹⁴⁰⁴ In both sets you have an increase in data in the bin below 75 cm and at bins below 0.5
¹⁴⁰⁵ GeV. These distributions were made with events classified with 70% probability of
¹⁴⁰⁶ being a muon regardless of true particle type.

¹⁴⁰⁷ **8.1.2 Classification of MC data using Selection I Modified**
¹⁴⁰⁸ **CC-Inclusive Filter**

Table 5: **Selection I: Modified** The table shows passing rates for the above described event selection. Numbers are absolute event counts and Cosmic background is not scaled appropriately. The BNB+Cosmic sample contains all events, not just ν_μ CC inclusive. The selected events are further broken up in the following subsection. The numbers in brackets give the passing rate wrt the step before (first percentage) and wrt the generated events (second percentage). In the BNB+Cosmic Mc Truth column shows how many true ν_μ CC inclusive events (in FV) are left in the sample. This number includes possible mis-identifications where a cosmic track is picked by the selection instead of the neutrino interaction in the same event. The cosmic only sample has low statistics, but please note that it is not used in any plots, it is just for illustrating the cut efficiency. The last column Signal:Cosmic only gives an estimate of the ν_μ CC events wrt the cosmic only background at each step. For this number, the cosmic background has been scaled as described in chapter 2. Note that this numbers is not a purity, since other backgrounds can't be determined at this step.

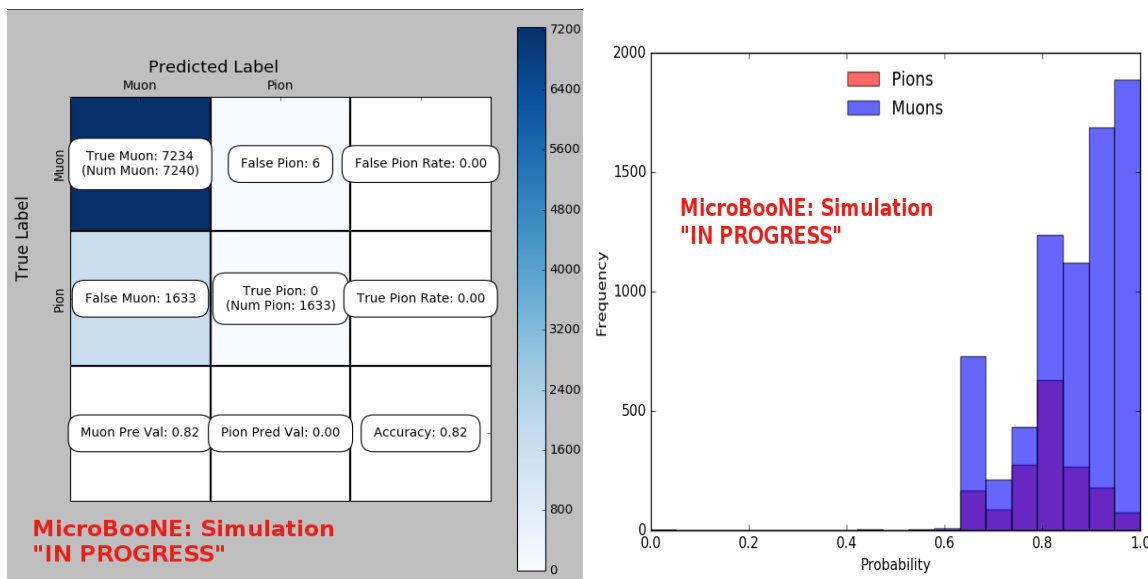
	BNB + Cosmic Selection	MC-Truth	Cosmic only	Signal: Cosmic only
Generated events	191362	45273	4804	1:22
≥ 1 flash with ≥ 50 PE	136219 (71%/71%)	44002 (97%/97%)	2979 (62%/62%)	1:14
≥ 1 track within 5 cm of vertex	135830 (99%/71%)	43974 (99%/97%)	2975 (99%/62%)	1:14
vertex candidate in FV	79112 (58%/41%)	34891 (79%/77%)	1482 (50%/31%)	1:8.9
flash matching of longest track	40267 (51%/21%)	25891 (74%/57%)	340 (23%/7.1%)	1:2.8
track containment	19391 (48%/10%)	11693 (45%/26%)	129 (38%/2.7%)	1:2.3
track ≥ 75 cm	6920 (36%/3.6%)	5780 (49%/13%)	17 (13%/0.4%)	1:0.6

Figure 8.4: Snapshot of passing rates of all cuts from Selection I Modified cc-inclusive filter

¹⁴⁰⁹ CNN10000 was also used to classify track candidate images that were identified by
¹⁴¹⁰ the selection I modified cc-inclusive filter described in [?]. Passing rates for each cut in
¹⁴¹¹ this filter are shown in figure 8.4. As seen in section 8.1.1, wrong image normalization
¹⁴¹² had a higher muon classification probability so all work done using selection I modified
¹⁴¹³ cc-inclusive filter was done using this normalization. Out of 188,880 events, 19,112
¹⁴¹⁴ passed the cut right before the 75 cm track length cut which is a 10.1% passing rate and
¹⁴¹⁵ comparable to the 10% passing rate shown in figure 8.4. In time cosmics were also run
¹⁴¹⁶ over, out of 14,606 in time cosmics events, 302 passed the cut right before the 75 cm
¹⁴¹⁷ track length cut which is a 2.1% passing rate comparable to the 2.7% passing rate in the
¹⁴¹⁸ cc-inclusive tech-note. Figures 8.5a and 8.5b show the accuracy and μ/π separation.
¹⁴¹⁹ Both plots are only composed of muons and pions and like selection I original data,

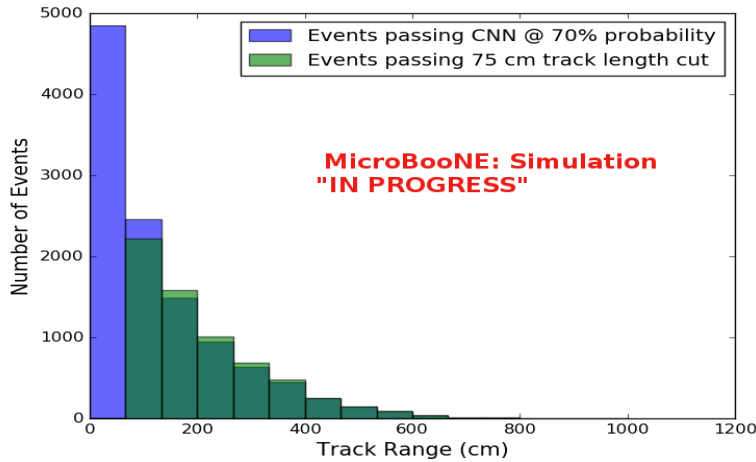
1420 all other particles were id'ed as muons. Also like selection I original data, muons are
 1421 being identified at a very high rate. Figure 8.6a shows the track range distributions
 1422 of all events from selection I modified being classified by the CNN as a muon with a
 1423 probability of 70% regardless of true particle type. We get entries for the CNN curve
 1424 in the lowest bin and none for the 75 cm curve. To see how many true CC events
 1425 were identified by CNN10000 breaking down figure 8.6a by event type was necessary.
 1426 Figures 8.6b and 8.6c show track range distributions separated by signal and various
 1427 backgrounds. Particle type was not taken into consideration in these plots so true CC
 1428 event images can be any track candidate particle passing selection I modified cut right
 1429 before track length cut including pions and protons.

1430 To gain an even deeper understanding on how CNN10000 is performing, plotting
 1431 these distributions with only muons and pions was done due to the fact that CNN10000
 1432 was trained with only those particles for μ/π separation. Figures 8.6d-8.7d show the
 1433 stacked histograms of signal and background of the track range distributions with
 1434 varying CNN probabilities starting from 70% and ending at 90% probability. With
 1435 higher probabilities we get a purer sample in the lower bin but we end up losing
 1436 events as well. Momentum distributions for all signal/background events are shown
 1437 in figure 8.8.

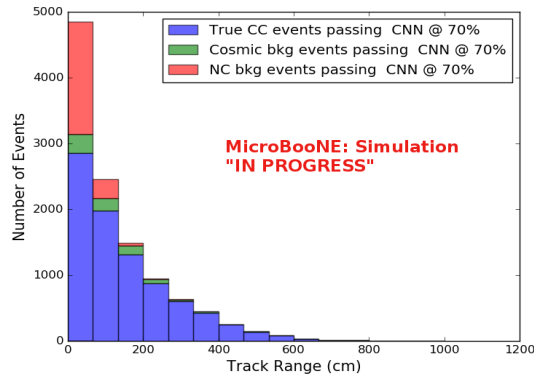


(a) Confusion Matrix for CNN10000 classified events from selection I modified (b) Probability plot for CNN10000 classified events from selection I modified

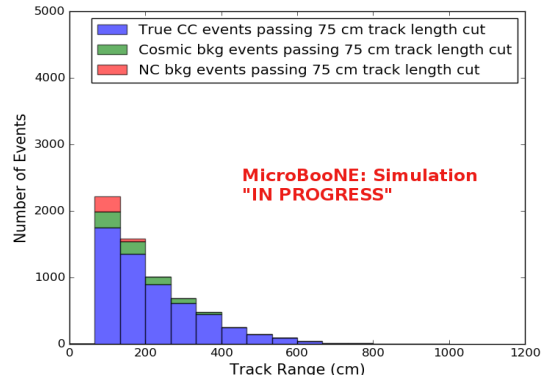
Figure 8.5: Confusion matrix and probability plot of events passing selection I modified cc-inclusive cuts right before 75cm track length cut



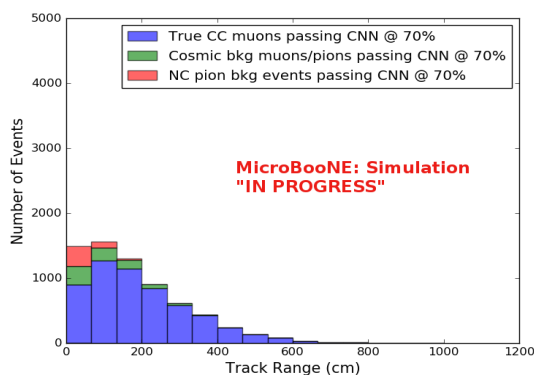
(a) Track range distribution of events from Selection I Modified passing CNN with 70% accuracy



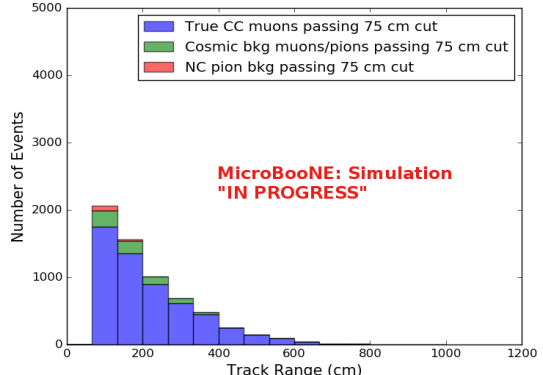
(b) Stacked signal and background track range distributions from Selection I Modified passing CNN with 70% accuracy



(c) Stacked signal and background track range distributions from Selection I Modified passing 75 cm track length cut



(d) Stacked signal muons and background muons/pions of track range distributions from Selection I Modified passing CNN with 70% accuracy



(e) Stacked signal muons and background muons/pions of track range distributions from Selection I Modified passing 75 cm track length cut

Figure 8.6: CNN10000 distributions of track candidate images output from Selection I Modified cc-inclusive filter

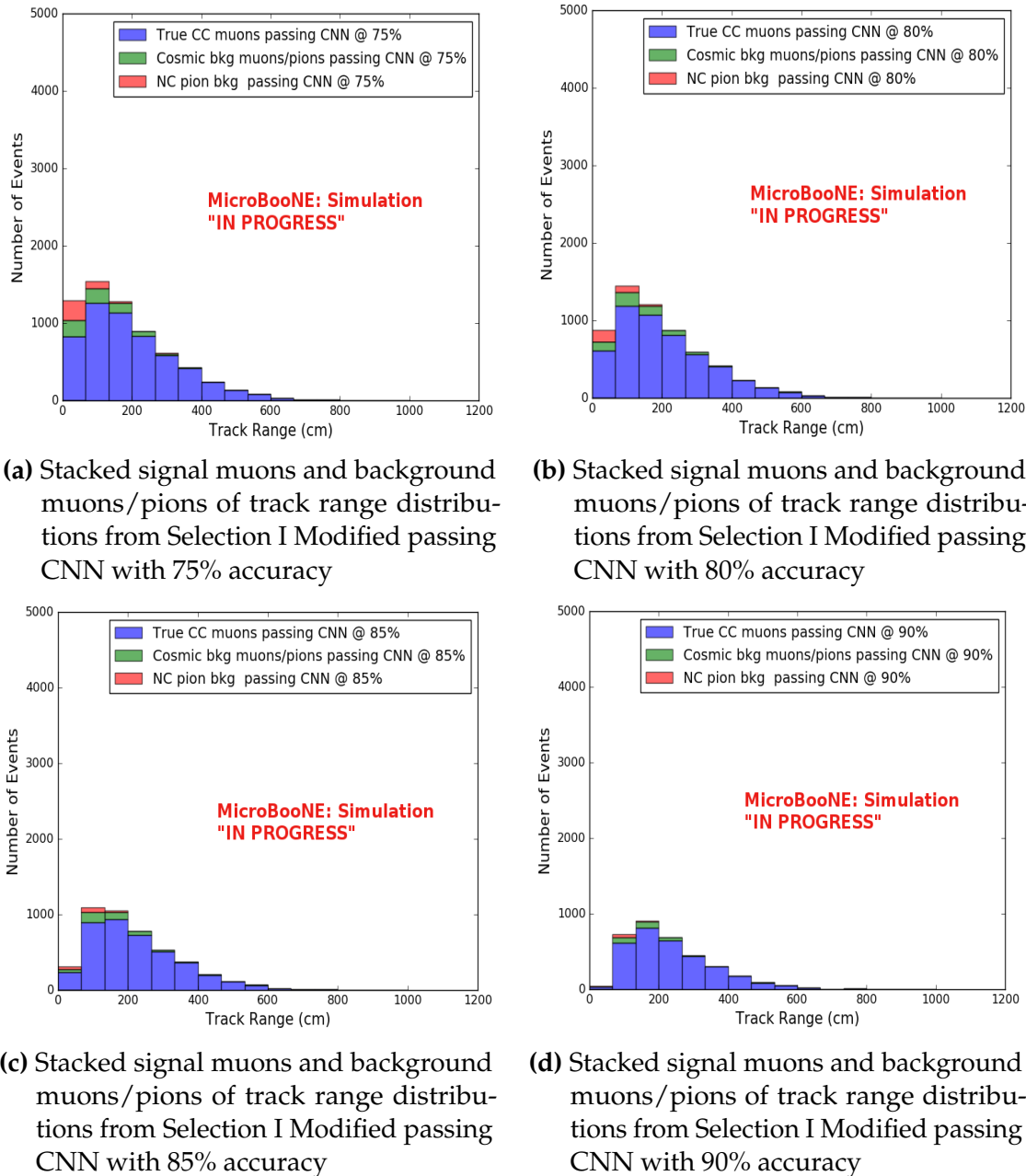
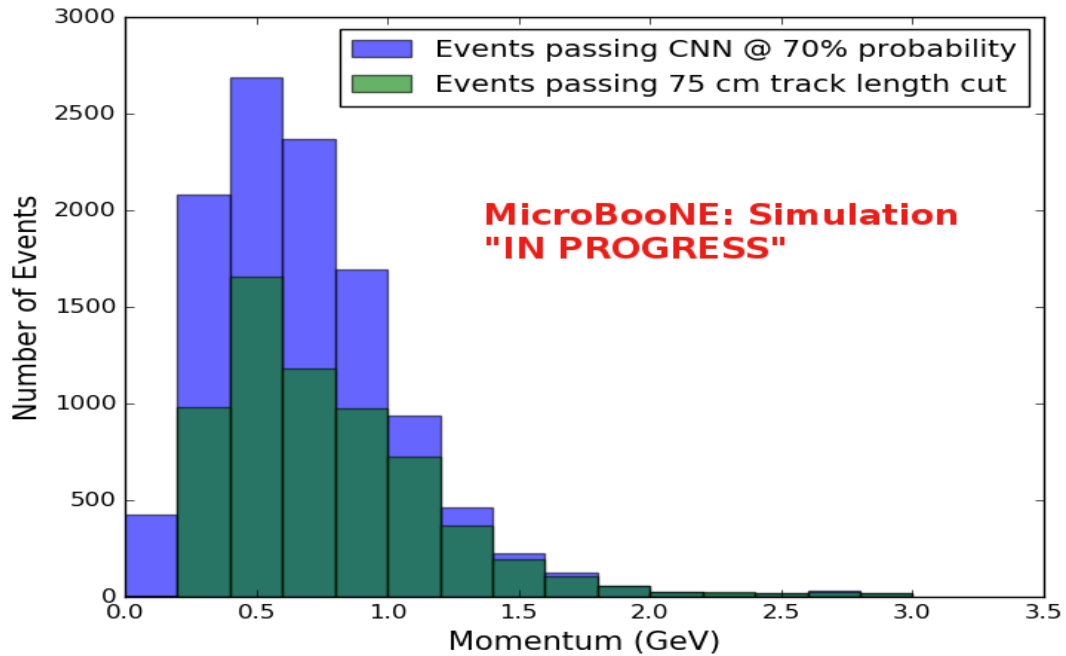
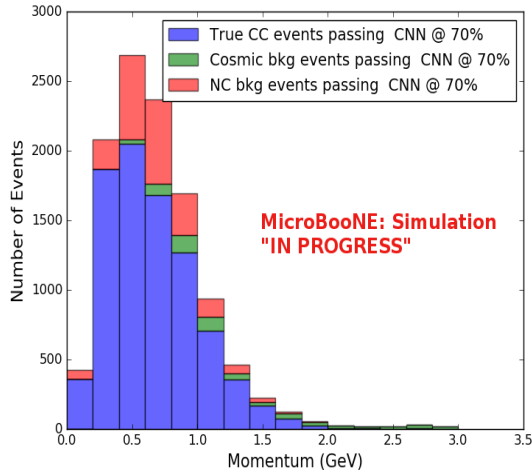


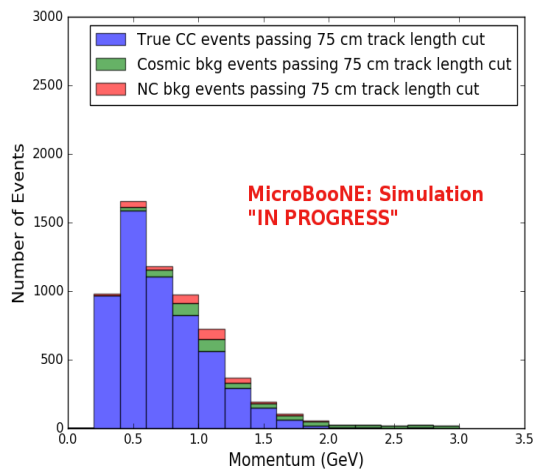
Figure 8.7: CNN10000 stacked signal/background track range distributions of track candidate images output from Selection I Modified cc-inclusive filter



(a) Momentum distribution of events from Selection I Modified passing CNN with 70% accuracy



(b) Stacked signal and background momentum distributions from Selection I Modified passing CNN with 70% accuracy



(c) Stacked signal and background momentum distributions from Selection I Modified passing 75 cm track length cut

Figure 8.8: CNN10000 momentum distributions of track candidate images output from Selection I Modified cc-inclusive filter

Another check was to see if any true CC pions were passing through the cut right before the 75 cm track length cut. Figure 8.9 shows the comparison of the stacked track range distribution with only true CC muon signal versus the stacked distribution with true CC muons and pions signal. As you can see, we gain more events when plotting CC events with a particle type of either muons or pions due to the CNN classifying all pions in this dataset as muons. This is an interesting scenario and a sample of topologies of these images are represented in figure 8.10, at least 3 tracks are coming out of the vertex for these types of events. With the 75 cm track length cut, the selection is cutting event topologies like this where the pion is the tagged track candidate. Figure 8.10a has a defined longer muon track, but because of dead wires through the track, the reconstructed range is 1. less than 75 cm and 2. shorter than the reconstructed pion whose length is also less than 75 cm. This is a very interesting event, but because of issues with the tracking algorithm, the 75 cm cut would get rid of this event. The CNN was able to recover this event only because it has classified all pions as muons. Figure 8.10b shows the second case to think about, the pion, while still less than 75 cm has a reconstructed track length longer than the muon. Again, the CNN recovered this event due to pions being classified as muons. Lastly, figure 8.10c shows a pion with a reconstructed track length greater than 75 cm and the muon. These three cases show that a broader question must be asked when training the network other than is it a muon or pion. There are different routes to recover interesting events like these. One route is to ask the network “Is it a CC event or is it an NC event?” and obtain an image dataset consisting of whole CC/NC events that will train the network to answer this question. The other route is to ask the network “Is this a $\mu/\pi/p/$ from a CC event or NC event and obtain an image dataset consisting of primary particles from a CC/NC event. Both these paths will be explored in future work.

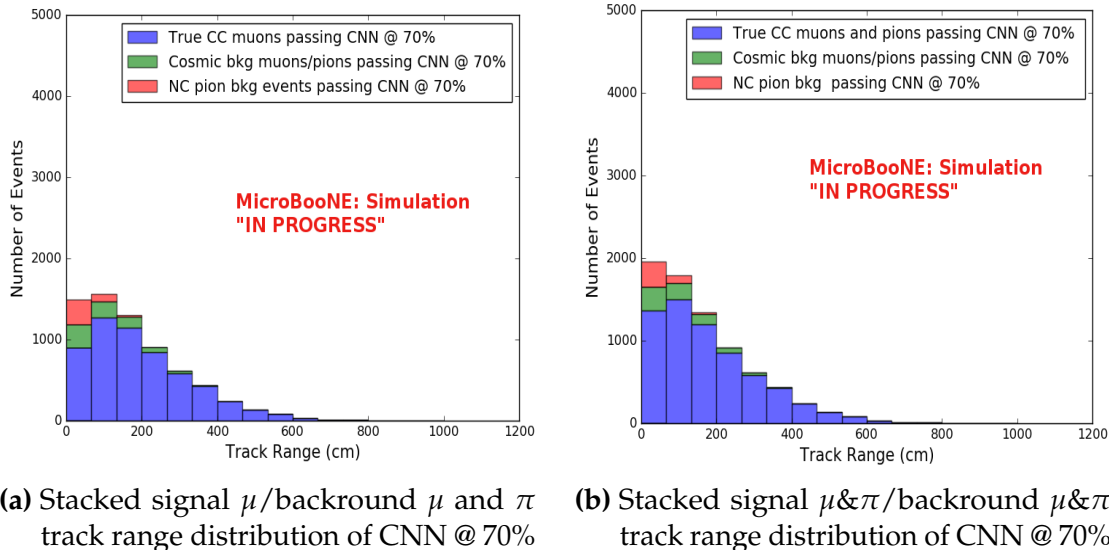


Figure 8.9: Track distribution comparisons of true CC muons plotted vs true CC muons and pions plotted

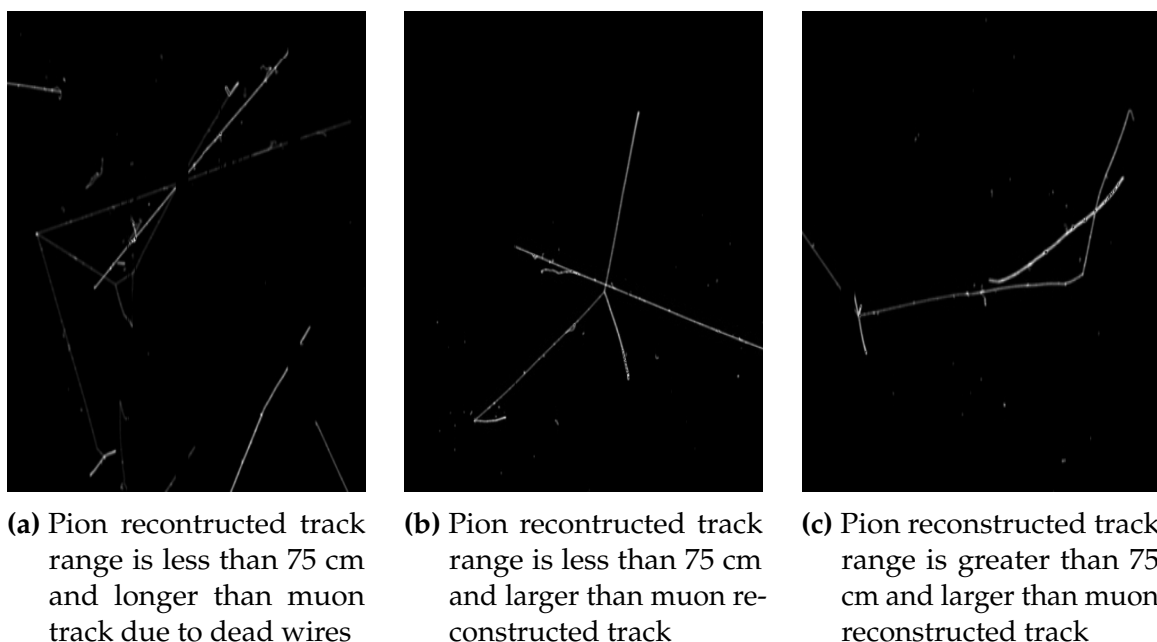


Figure 8.10: Images of true CC events where the pion was the tagged track candidate

		BNB + Cosmics		Cosmic Only	Signal: Cosmic Only
		Selection	MC Truth		
75 cm Cut passing rates	Generated Events	191362	45723	4804	1:22
	Track Containment	19391 (48%/10%)	11693 (45%/26%)	129 (38%/2.7%)	1:2.3
	track \geq 75 cm	6920 (36%/3.6%)	5780 (49%/13%)	17 (13%/0.4%)	1:0.6
CNN passing rates	Generated Events	188880	44689	14606	1:21
	Track Containment	19112 (/10%)	11554 (/26%)	302 (/2.1%)	1:1.73
	CNN cut @ 70% Probability	16502 (86%/8.7%)	10605 (92%/23%)	205 (68%/14%)	1:1.28
	CNN cut @ 83% Probability	7511 (46%/4.0%)	6142 (58%/14%)	32 (16%/0.2%)	1:0.4

Table 8.1: Comparing passing rates of CNN at different probabilities versus 75 cm track length cut: Numbers are absolute event counts and Cosmic background is not scaled appropriately. The BNB+Cosmic sample contains all events. The numbers in brackets give the passing rate wrt the step before (first percentage) and wrt the generated events (second percentage). In the BNB+Cosmic MC Truth column shows how many true ν_μ CC-inclusive events (in FV) are left in the sample. This number includes possible mis-identifications where a cosmic track is picked by the selection instead of the neutrino interaction in the same event. The CNN MC True generated events were scaled wrt the MC True generated events for the 75 cm cut passing rates due to only running over 188,880 generated events versus the 191362 generated events. The last column Signal:Cosmic only gives an estimate of the ν_μ CC events wrt the cosmic only background at each step. For this number, the cosmic background has been scaled as described in [?]. Note that these numbers are not a purity, since other backgrounds can't be determined at this step.

Signal	ν_μ CC events with true vertex in FV	#Events(Fraction)	#Events(Fraction)
		passing CNN @ 70% Probability	
Backgrounds		10605(35%)	#Events(Fraction) passing CNN @ 83% Probability
	Cosmics Only Events	13573(45%)	
	Cosmics in BNB Events	2249(7.4%)	
	NC Events	3412(11%)	
	ν_e and $\bar{\nu}_e$ Events	139(0.5%)	
	$\bar{\nu}_\mu$ Events	97(0.3%)	

Table 8.2: Signal and background event numbers at modified selection level with CNN cut estimated from a BNB+Cosmic sample and Cosmic only sample normalized to $5 * 10^{19}$ PoT. The last column gives the fraction of this signal or background type to the total selected events per CNN probability.

Table 8.1 shows the passing rates for the 75 cm track length cut and the CNN cut at 70% and 83%. The passing rates at the track containment level for the 75 cm track length cut compared to the CNN are comparable with only a 0.6% difference in the in time cosmic bin which may be due in part to the larger in time cosmic statistics used for the CNN dataset. These passing rates need to be comparable to then be able to compare the passing rates after the CNN cut to the 75 cm cut. Again, the same BNB+Cosmic sample was used for both selection I modified with 75 cm cut and selection I modified with CNN cut. As it stands, a CNN cut at 83% probability has

¹⁴⁷¹ a MC true CC event passing rate of 14% compared to the 13% passing rate of the 75
¹⁴⁷² cm track length cut. The Signal:Cosmic Only background is also reduced from 1:0.6
¹⁴⁷³ to 1:0.4 The total passing rate is also higher than the 75 cm cut, 3.6% vs 4.0%. Table
¹⁴⁷⁴ 8.2 shows the breakdown of signal and backgrounds for the CNN at the different
¹⁴⁷⁵ probabilities. We have a 61% signal passing rate with the CNN cut @ 83% versus the
¹⁴⁷⁶ 53.8% signal passing rate of the 75 cm cut.

¹⁴⁷⁷ Based on these numbers, the following performance values of the modified selec-
¹⁴⁷⁸ tion with 75 cm cut versus modified selection with CNN @ 83% probability cut were
¹⁴⁷⁹ calculated:

- ¹⁴⁸⁰ • Efficiency: Number of selected true ν_μ CC events divided by the number of
¹⁴⁸¹ expected true ν_μ CC events with interaction in the FV.
 - ¹⁴⁸² – Selection I modified: 13%
 - ¹⁴⁸³ – Selection I modified with CNN cut @ 83% probability: 14%
- ¹⁴⁸⁴ • Purity: Number of selected true ν_μ CC events divided by sum of itself and the
¹⁴⁸⁵ number of all backgrounds.
 - ¹⁴⁸⁶ – Selection I modified: 53.8%
 - ¹⁴⁸⁷ – Selection I modified with CNN cut @ 83% probability: 61%

¹⁴⁸⁸ Lastly, figure 8.12 shows a more representative performance of the CNN. Due to
¹⁴⁸⁹ the fact that the CNN was trained on muons and pions, showing the performance
¹⁴⁹⁰ of CC muon events versus NC pion events with respect to CNN probability gives a
¹⁴⁹¹ better picture of how the network is performing. Figure 8.12 shows that at 83% we
¹⁴⁹² are below the 75 cm cut NC pion threshold and still above the CC muon threshold.
¹⁴⁹³ Using 83% probability not only reduced the NC pion background, it also dramatically
¹⁴⁹⁴ reduced the in time cosmics and cosmics in the BNB.

¹⁴⁹⁵ 8.1.3 Conclusions and Future Work

¹⁴⁹⁶ It was shown that even though CNN10000 was trained with single particle generated
¹⁴⁹⁷ muons and pions, it performs fairly well at classifying track candidate images from
¹⁴⁹⁸ BNB+Cosmic events. Events have been regained below the 75 cm track length cut and
¹⁴⁹⁹ the momentum and track range distributions have similar shapes to the distributions of
¹⁵⁰⁰ Selection I original and modified. Efficiencies and purities were calculated for selection

Table 8: **Selection I: Modified** Signal and background event numbers at modified selection level estimated from a BNB+Cosmic sample and Cosmic only sample normalized to 5×10^{19} PoT. The last column gives the fraction of this signal or background type to the total 2189 selected events.

Signal	#Events	
ν_μ CC events with true vertex in FV	1168	53.8%
Backgrounds		
Cosmics only events	725	33.4%
Cosmics in BNB events	144	6.6%
NC events	75	3.5%
ν_e and $\bar{\nu}_e$ events	4	0.2%
$\bar{\nu}_\mu$ events	15	0.7%
ν_μ CC events with true vertex outside FV	40	1.8%

Figure 8.11: Snapshot of signal and background event numbers of Selection I modified from cc-inclusive note [?]

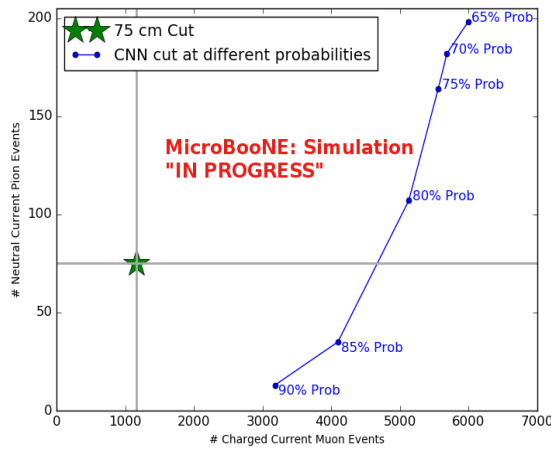


Figure 8.12: CNN performance of classified muons and pions compared to the already implemented 75 cm track length cut

1501 I modified events before 75 cm track length cut with the CNN at 83% probability and
1502 are 14% and 62% respectively. Although the CNN doesn't have separation between
1503 muons and pions and although all particles passing CNN are classified as muon,
1504 increasing CNN probability allows us to increase the purity as well as maintain an
1505 efficiency comparable to the 75 cm track length cut all while recovering events below
1506 that 75 cm cut. Out of the 6142 events that passed the CNN @ 83% 1470 events were
1507 below the 75 cm cut, a recovery of 3.3% of data with a purity of 15%. Although
1508 these numbers are low, it is an improvement from the selection I modified in both total
1509 efficiency and purity and an increase in phase space by recovering these events.

1510 **8.2 Classification using CNN100000**

1511 All future classifications will be done using Selection I Modified CC-Inclusive Filter
1512 because it has a higher efficiency and purity than Selection I Original CC-Inclusive
1513 Filter. To reiterate, CNN100000 was trained using 20,000 images of each $\mu/\pi/p/\gamma/e$.
1514 The results of using CNN100000 to classify BNB+Cosmics will be outlined below.

1515 **8.2.1 Classification of MC data using Selection I Modified
1516 CC-Inclusive Filter**

1517 **8.2.2 Classification of MicroBooNE data using Selection I Modified
1518 CC-Inclusive Filter**

1519 **8.2.3 Comparing two CC-Inclusive Cross Section Selection Filters**

₁₅₂₀ **Chapter 9**

₁₅₂₁ **Conclusion**

₁₅₂₂ Your Conclusions here.

₁₅₂₃

₁₅₂₄ **Bibliography**

- ₁₅₂₅ [1] Wikipedia, Neutrino, <http://wikipedia.org/wiki/Neutrino>, 2013.
- ₁₅₂₆ [2] Wikipedia, Neutrino oscillation, http://en.wikipedia.org/wiki/Neutrino_oscillation, 2013.
- ₁₅₂₇
- ₁₅₂₈ [3] B. N. Laboratory, Neutrinos and nuclear chemistry, <http://www.chemistry.bnl.gov/sciandtech/sn/default.htm>, 2010.
- ₁₅₂₉
- ₁₅₃₀ [4] K. Heeger, Big world of small neutrinos, <http://conferences.fnal.gov/lp2003/forthepublic/neutrinos/>.
- ₁₅₃₁
- ₁₅₃₂ [5] A. Y. Smirnov, p. 23 (2003), hep-ph/0305106.
- ₁₅₃₃ [6] The MicroBooNE Collaboration, R. e. a. Acciari, (2015), arXiv:1512.06148.
- ₁₅₃₄ [7] The MicroBooNE Collaboration, R. e. a. Acciari, (2016), arXiv:1705.07341.
- ₁₅₃₅ [8] The MicroBooNE Collaboration, R. e. a. Acciari, (2017), arXiv:1704.02927.
- ₁₅₃₆ [9] The MicroBooNE Collaboration, R. e. a. Acciari, JINST **12** (2017).